

2012-01-01

# Electrochemical Behavior Of Galvanized Steel Embedded In Soil

Jesus F. Hinojos

*University of Texas at El Paso*, [jfhinojos@miners.utep.edu](mailto:jfhinojos@miners.utep.edu)

Follow this and additional works at: [https://digitalcommons.utep.edu/open\\_etd](https://digitalcommons.utep.edu/open_etd)



Part of the [Engineering Commons](#)

---

## Recommended Citation

Hinojos, Jesus F., "Electrochemical Behavior Of Galvanized Steel Embedded In Soil" (2012). *Open Access Theses & Dissertations*. 2106.  
[https://digitalcommons.utep.edu/open\\_etd/2106](https://digitalcommons.utep.edu/open_etd/2106)

This is brought to you for free and open access by DigitalCommons@UTEP. It has been accepted for inclusion in Open Access Theses & Dissertations by an authorized administrator of DigitalCommons@UTEP. For more information, please contact [lweber@utep.edu](mailto:lweber@utep.edu).

ELECTROCHEMICAL BEHAVIOR OF  
GALVANIZED STEEL EMBEDDED IN SOIL

JESUS F HINOJOS

Department of Mechanical Engineer

APPROVED:

---

Arturo Bronson, Ph.D.

---

Soheil Nazarian, Ph.D.

---

Yirong Lin, Ph.D.

---

Benjamin C. Flores, Ph.D.  
Interim Dean of the Graduate School

Copyright ©

by

Jesus F. Hinojos

2012

ELECTROCHEMICAL BEHAVIOR OF  
GALVANIZED STEEL EMBEDDED IN SOIL

by

JESUS F. HINOJOS

THESIS

Presented to the Faculty of the Graduate School of

The University of Texas at El Paso

in Partial Fulfillment

of the Requirements

for the Degree of

MASTER OF SCIENCE

Department of Mechanical Engineering

THE UNIVERSITY OF TEXAS AT EL PASO

August 2012

## **Acknowledgement**

I would like to extend my sincere gratitude to Dr. Arturo Bronson for guiding me throughout my graduate career and the continuous support of my M.S. study and research, for his patience, motivation, enthusiasm, and immense knowledge. His guidance helped me in all the time of research and writing of this thesis. I could not have imagined having a better advisor and mentor for my M.S. study. Besides my advisor, I would also like to thank the rest of my thesis committee, Dr. Nazarian for all the advice and support that has made the completion of my degree less arduous and Dr. Lin for his support that has made the completion of my degree possible.

Most importantly, none of this would have been possible without the love and patience of my family. My immediate family, to whom this dissertation is dedicated to, has been a constant source of love, concern, support and strength all these years. I would like to express my heart-felt gratitude to my parents Jesus F Hinojos and Virginia Aguilera for their unwavering support during my education. I would especially like to thank my fiancée Reyna Espinoza who supported me above anyone else during the process of finishing my degree.

## Abstract

The investigation focused on the corrosion of galvanized steel embedded in soil. The primary objective of the study was to develop a technique for monitoring the corrosion behavior of samples in the field by measuring the potential and current with respect to time (or electrochemical noise). Electrochemical electrodes were designed to simulate the galvanized steel in contact with a thin-film of electrolytes which are usually generated in soils as they collect and drain rain water depending on soil porosity. The exposure of the galvanized steel to thin-film electrolytes consisted of cycling between two days of wetted soil followed by the removing the water and essentially allowing the soil to dry for five days. The cycled exposure of two-day wet/five-day continued for approximately two years.

To further characterize the corrosion behavior of the galvanized steel, their surfaces were also studied with electrochemical impedance spectroscopy (EIS) to determine the effect of diluted chloride solutions. From the EIS, the corrosion rate was acquired when coupled with a potentiokinetic technique, or polarization scan. The corrosion rate for the galvanized steel reached 81 mils/yr at the high chloride content (i.e., 0.1 M NaCl) and 0.0034 mils/year for the low chloride content (i.e., 0.0001 M NaCl). In comparing the corrosion rates available from field bilogarithmic trends and the acquired laboratory studies, the laboratory corrosion rates of 0.0034 and 81  $\mu\text{m}/\text{yr}$  at 0.0001 and 0.1 M NaCl, respectively, corresponded to the field corrosion rate of 20  $\mu\text{m}/\text{yr}$  at 200 ppm Cl (approximating 0.0002 M Cl).

The current transients acquired from cycled exposure were linked to EIS measurements by using the conductivity of a NaCl solution. Corrosion rates were calculated for galvanized steel embedded in soil from six sites across the state of Texas. The corrosion rates ranged initially from 820 to 14  $\mu\text{m}/\text{year}$  to a plateau rate of 9 to 0.1  $\mu\text{m}/\text{year}$  depending on the site.

## Table of Contents

Chapter 1: Introduction .....	1
1.1 Overview .....	1
1.2 Objective .....	2
Chapter 2: Literature Review .....	3
2.1 Corrosion of Zinc and Carbon Steel.....	3
2.1.1 Mechanisms of corrosion of Zinc .....	3
2.1.2 Carbon steel oxidation .....	9
2.2 Electrochemical methods for studying corrosion.....	13
2.2.1 Polarization resistance of galvanized steel .....	14
2.2.2 Electrochemical Impedance Spectroscopy .....	16
2.2.3 Electrochemical Noise.....	19
2.3 Fe-Zn phase equilibria and kinetics .....	23
Chapter 3: Methodology .....	26
3.1 Galvanized steel electrode preparation .....	26
3.2 Delrin coupon preparation.....	27
3.3 Electrode coupon assembly.....	27
3.4 Electrode positioning structure.....	28
3.5 Polarization scan experiments setup .....	29
3.6 Electrochemical impedance experiments setup.....	30
3.7 Electrochemical noise experiments setup .....	32
Chapter 4: Result and Discussion .....	34

4.1	Electrochemical Impedance Spectroscopy .....	34
4.2	Electrochemical Noise.....	43
4.3	Microstructures and corrosion products.....	46
Chapter 5: Conclusion.....		51
Bibliography .....		52
Appendix.....		56
Curriculum Vitae.....		78



## **List of Table**

Table 1. Corrosion Products Formed on Various Sacrificial Metal Coatings .....	4
Table 2 Chemical compounds found in rust layer .....	10
Table 3. Resistivities with respect to the solution molarity in addition to the resistivity of Quarry F soil solution after 24 months.....	38
Table 4. Values for equivalent circuit 0.0001 M NaCl solution.....	38
Table 5 Corrosion rate results for galvanized steel at different NaCl molarities. ....	40

## List of Figures

Figure 1 Change in (a) reciprocal polarization resistance $R_p^{-1}$ and (b) corrosion potential $E_{\text{corr}}$ of Galvanized Steel GI and Zinc Sheet Zn with cycle number (Yavad, et al., 2007) .....	5
Figure 2 Illustration of corrosion mechanism of galvanized steel (Yavad, et al., 2007) .....	6
Figure 3 Hot-dip galvanized steel phases .....	9
Figure 4 Back extrapolation of a linear section of anodic and cathodic polarization curves (Jones, 1992) .....	15
Figure 5 Experimental bode diagram and fit to the TML model for Type 304 stainless steels covered with a 0.1 NaCl solution layer (Nishikata, et al., 1995). .....	18
Figure 6 Comparison of MEM and FFT on white noise (Bertocci, et al., 1998). .....	22
Figure 7 Fe-Zn equilibrium phase diagram (Kubachewski, et al., 1986). .....	24
Figure 8 Zn Rich part of the Fe-Zn phase diagram (Kubachewski, et al., 1986) .....	24
Figure 9 Hot-dip galvanized steel phases .....	24
Figure 10 Galvanized steel plate after CNC machining. ....	26
Figure 11. Finished electrode coupon, and side view of a finished electrode coupon with cable holes. ....	27
Figure 12. Electrode positioning structure.....	29
Figure 13 Equivalent circuit describing one time constant.....	30
Figure 14 Equivalent circuit describing two time constant .....	31
Figure 15 Potential and frequency response detector connection setup .....	32
Figure 16 Circuits used to acquire current and voltage electrochemical noise simultaneously....	33
Figure 17 Adjusted Bode plot and Phase angle plot for 0.0001 M NaCl solution.....	35
Figure 18 Bode and Nyquist plot of galvanized steel at 0.0001 M NaCl. Acquired with	

PowerSINE .....	36
Figure 19 Nyquist plot of galvanized steel at 0.0001 M NaCl. Acquired with Zview .....	36
Figure 20 Bode and Phase angle plots of galvanized steel at 0.0001 M NaCl. Acquired with Zview .....	37
Figure 21. Solution resistance at different NaCl molarities. Acquired from PowerSINE .....	38
Figure 22. Equivalent circuit describing the two time-constant system of galvanized steel corroding in 0.0001 M NaCl solution. ....	38
Figure 23 . Polarization curve of galvanized steel in 0.0001 M NaCl. Acquired with PowerCV (Castillo, 2011).....	40
Figure 24. Change in current density as the NaCl molarity increases. ....	41
Figure 25 Corrosion rate in $\mu\text{m}/\text{yr}$ as the NaCl molarity increases. ....	41
Figure 26 Conductivity vs. corrosion rate.....	42
Figure 27 Corrosion rate vs time wet/dry .....	42
Figure 28. Elias' diagram showing the corrosion rates for zinc at 0.0001 and 0.001 M NaCl and 200 ppm Cl (0.0002 Cl). ....	43
Figure 29 Current data corresponding to Quarry F.....	44
Figure 30 Current PSD acquired from FFT Quarry F sample .....	45
Figure 31 Current PSD acquired from MEM (order 1000) Quarry F Sample.....	45
Figure 32 Current PSD Overlapping FFT and MEM Quarry F of Sample .....	45
Figure 33 Variance of PSD acquired from FFT analysis for Quarry F W/D full cycles spec 2....	46
Figure 34 Plateau vs. Time Quarry F full cycles W/D. Error bars indicate the std. error.....	46
Figure 35 SEM image of the galvanized steel microstructure. ....	47
Figure 36 SEM image Bridgeport galvanized steel electrode in wet cycle after full process. ....	48

Figure 37 Bridgeport mapping of galvanized steel electrode .....	48
Figure 38 Bridgeport line scan of galvanized steel.....	49
Figure 39 Bridgeport Galvanized steel scan line .....	49
Figure 40. Bode and Nyquist plots for galvanized steel at 0.0001 M NaCl solution. ....	56
Figure 41. Bode and Nyquist plots for galvanized steel at 0.0001 M NaCl solution. ....	57
Figure 42 Bode and Nyquist plots for galvanized steel at 0.0001 M NaCl solution. ....	58
Figure 43 Bode and Nyquist plots for galvanized steel at 0.001 M NaCl solution. ....	59
Figure 44. Bode and Nyquist plots for galvanized steel at 0.001 M NaCl solution. ....	60
Figure 45. Bode and Nyquist plots for galvanized steel at 0.001 M NaCl solution. ....	61
Figure 46. Bode and Nyquist plots for galvanized steel at 0.01 M NaCl solution. ....	62
Figure 47. Bode and Nyquist plots for galvanized steel at 0.01 M NaCl solution. ....	63
Figure 48. Bode and Nyquist plots for galvanized steel at 0.01 M NaCl solution. ....	64
Figure 49. Bode and Nyquist plots for galvanized steel at 0.1 M NaCl solution. ....	65
Figure 50. Bode and Nyquist plots for galvanized steel at 0.1 M NaCl solution. ....	66
Figure 51. Bode and Nyquist plots for galvanized steel at 0.1 M NaCl solution. ....	67
Figure 52 Nyquist plot of galvanized steel at 0.1 M NaCl. Acquired with Zview .....	68
Figure 53 Bode and Phase angle plots of galvanized steel at 0.1 M NaCl. Acquired with Zview	68
Figure 54 Nyquist plot of galvanized steel at 0.01 M NaCl. Acquired with Zview .....	69
Figure 55 Bode and Phase angle plots of galvanized steel at 0.01 M NaCl. Acquired with Zview .....	69
Figure 56 Nyquist plot of galvanized steel at 0.001 M NaCl. Acquired with Zview .....	70
Figure 57 Bode and Phase angle plots of galvanized steel at 0.001 M NaCl. Acquired with Zview .....	70

Figure 58 Electrochemical noise current vs. time.....	71
Figure 59 Electrochemical noise current vs. time.....	72
Figure 60 Electrochemical noise analysis for Quarry F wet/dry cycles Sp2 acquired with DADISP .....	73
Figure 61 Electrochemical noise analysis for Quarry F wet cycles Sp4 acquired with DADISP	74
Figure 62 Mesh 3 at 100x (2% Nital etch) acquired from optical microscope.....	75
Figure 63 SEM picture of Bridgeport full cycles wet (2% Nital etch) .....	76
Figure 64 SEM mapping picture of Bridgeport full cycles wet (2% Nital etch) .....	76
Figure 65 SEM picture of Quarry F Sp 2 full cycles wet dry (2% Nital etch) .....	77
Figure 66 SEM mapping picture of Quarry F Sp 2 full cycles wet dry (2% Nital etch) .....	77

## Chapter 1: Introduction

### 1.1 Overview

Zinc is commonly used as a coating for steel, which tend to form a porous oxide of one of the polymorphs of the ferric hydroxides ( $\text{FeOOH}$ ) and in a situation where the supply of water ( $\text{H}_2\text{O}$ ) is restricted,  $\text{Fe}_3\text{O}_4$  and  $\text{Fe}_2\text{O}_3$  may form in the corrosion process (Shreir, et al., 1994). Atmospheric corrosion is the most common corrosion for galvanized steel, corrosion by wet/dry cycles conditions containing chloride ions differs from fully immersing condition galvanized steel in chloride solution, because the diffusion of the oxygen is significantly greater under a thin electrolyte layer. Experiments have shown that the corrosion increase very fast in the first several cycles, followed by a gradual decrease and finally become constant (Yadav, et al., 2004). In the case where the zinc/steel is submitted to wet/dry cycles, a formation of a thin layer of electrolyte forms. During the dry period, zinc corrodes at different rates (Zhang, et al., 1993). The thin film electrolyte also would not allow the application of regular electrochemical techniques.

When the steel contacts zinc under immersed condition, the zinc acts as anode and the exposed steel base serves as a cathode, protected cathodically from corrosion. The zinc also has the ability to form a protective layer upon exposure to carbonates, oxides, or hydrated sulfates. Zinc corrosion reduces usually when the  $\text{ZnO}$  protective layer forms. A large number of zinc corrosion products have been identified like  $\text{ZnO}$ ,  $\text{Zn}(\text{OH})_2$ ,  $2\text{ZnCO}_3 \cdot 3\text{Zn}(\text{OH})_2$  (Porter, 1994). The dissolution of the zinc obviously depends of the time of wetness on the coating surface and the concentration of ions chloride.

To study the mechanism of the reaction during the corrosion of the zinc, it is necessary to use electrochemical methods to understand this process. In the last two decades, the technique at electrochemical impedance spectroscopy (EIS) has become increasingly understood in corrosion studies (Mansfeld, 1990). The principal process of the EIS is the measurement of potential, current, and resistance simulating mechanisms of corrosion. In the analysis of EIS (Jones, 1992), the impedance

behavior can be expressed in Nyquist plots or Bode plots, with equivalent circuits of resistance and capacitance circuits. Several authors use the same techniques to monitoring the corrosion process, (Mansfeld, et al., 1993) use the bode plots to show the impedance spectra for Fe while (Hamlaoui, et al., 2008) uses the Nyquist plot.

The information of all combined measurements result in polarization curves which describe the electrochemical reaction, electrode reaction are assumed to induce deviation from equilibrium due to the passage of electrical current through an electrochemical cell causing a change in the working electrode potential. This electrochemical phenomenon is referred to as polarization (Perez, 2004). Electrons are attracted from the material, and current runs in the opposite direction from cathodic current above. The anodic oxidation rate,  $i_a$ , is increased, while the cathodic reduction rate,  $i_c$ , is decreased, so the applied current density is  $i_{app,a} = i_a - i_c$  (Jones, 1992). Fontana and Greene (Fontana, et al., 1967) gives in-depth discussion about the polarization scans.

## 1.2 Objective

The main goal of this research is to apply electrochemical noise techniques to monitor passively the corrosion of galvanized steel. The solution developed from soil, rock aggregates and minerals as water permeates mechanically stabilized earth (MSE) wall seem to consist of ions concentration comparable of 0.0001 M NaCl solution (Castillo, 2011). Of course, the solution formed near a MSE wall contains a diluted ion content of  $Cl^-$ ,  $SO_4^{2-}$ , and  $CO_3^{2-}$ , which may concentrate as the solution decreases through water vaporization. Chloride ions are usually the most aggressive ion, but synergistic effects among of ions may contribute to corrosion. Hence, the objective of the present study is to characterize the corrosion of MSE galvanized steel using electrochemical noise coupled with EIS and polarization scan. The electrochemical noise could serve as a low-cost monitoring technique of corrosion.

## Chapter 2: Literature Review

### 2.1 Corrosion of Zinc and Carbon Steel

#### 2.1.1 Mechanisms of corrosion of Zinc

Depending upon the nature of the environment, the zinc has the ability to form a protective layer made up of the basic carbonates, oxides, or hydrated sulfates. In atmospheric corrosion the zinc coating is exposed to wet-dry cycles, forming a thin electrolyte film composed primary of zinc oxide products. The zinc coating corrodes at an accelerated rate on the first cycles, but after long-term corrosion, rate approximates a linear trend even in the most aggressive atmospheres (Porter, 1994). The conditions that lend to the formation of soluble films may dissolve zinc rapidly. Studies demonstrate that after the reciprocal of the polarization resistance reaches its maximum point, directions change to negative slope and the average corrosion rate decreases, and the corrosion potential ( $E_{\text{corr}}$ ) changes to the noble direction (Yadav, et al., 2004). The reed dust ( $\text{FeOOH}$ ) appears on the coating surface, because the zinc coating does not act as a sacrificial anode due to the excess of zinc corrosion products on the coating surface (El-Mahdy, et al., 2000). In a previous study, they showed that the underlying steel corrosion appears after the polarization resistance ( $R_p^{-1}$ ) reaches a maximum, and red rust appears as an indication that the zinc does not protect the steel with the galvanic protection (Yadav, et al., 2004). Yadav et al. also demonstrated that the corrosion rate was uniform during the first cycle of the experiments and then a more localized as the wet-dry cycles continues with a longer exposure time. The study revealed that the zinc layer with the shorter drying period showed the grater thickness loss, but without formation of  $\text{FeOOH}$  during the experiment. The samples with the longer drying period showed the  $\text{FeOOH}$  to the naked eye.

Many corrosion cells are formed in the surface accelerating the corrosion rate, as a sacrificial metal when the zinc is exposed to the natural atmosphere. During this time, corrosion products are gradually formed and converted to a stable layer, as shown in the *Table 1*. Through, experiments Yadav



identified corrosion products during wet-dry cycles in a 0.05 M NaCl solution with a fixed layer of 500  $\mu\text{m}$  thickness during the drying period to ensure a constancy of the electrolyte thickness. The products in order of chloride concentration were:  $\text{Zn}(\text{OH})_2 < \text{ZnCl}_2 \cdot 6\text{Zn}(\text{OH})_2 < \text{ZnCl}_2 \cdot 4\text{Zn}(\text{OH})_2$ , as the concentration of chloride and hydrogen ions increased. During the drying process, the molarity of NaCl increases near 5 M creating a large concentration of chloride ions (Yadav, et al., 2004).

*Table 1. Corrosion Products Formed on Various Sacrificial Metal Coatings*

<b>Metal</b>	<b>Corrosion Product</b>
<b>Al</b>	$\text{Al}_2\text{O}_3$ , $\beta\text{Al}_2\text{O}_3 \cdot \text{H}_2\text{O}$ , $\alpha\text{AlOOH}$ , $\text{Al}(\text{OH})_3$ , amorphous $\text{Al}_2\text{O}_3$
<b>Zn</b>	$\text{ZnO}$ , $\text{Zn}(\text{OH})_2$ , $2\text{ZnCO}_3 \cdot 3\text{Zn}(\text{OH})_2$ , $\text{ZnSO}_4 \cdot 4\text{Zn}(\text{OH})_2$ , $\text{ZnCl}_2 \cdot 4\text{Zn}(\text{OH})_2$ , $\text{ZnCl}_2 \cdot 6\text{Zn}(\text{OH})_2$
<b>Mn</b>	$\gamma\text{-Mn}_2\text{O}_3$ , $\text{MnCO}_3$ , $\gamma\text{-MnOOH}$
<b>Cd</b>	$\text{CdO}$ , $\text{CdOH}_2$ , $2\text{CdCO}_3 \cdot 3\text{Cd}(\text{OH})_2$

(Schweitzer, 2010)

Yadav et al. identified three stages during the corrosion process. In the first stage of corrosion,  $R_p^{-1}$  increases and shifts the  $E_{\text{corr}}$  in negative direction, as shown in the initial stage *Fig. 1*. The anodic dissolution of the zinc coating is more accelerated than the cathodic process of oxygen reduction on the coating surface. The surface dissolves into  $\text{Zn}^{2+}$  leaving a thicker layer of  $\text{ZnCl}_2 \cdot 4\text{Zn}(\text{OH})_2$ , but this product does not act as barrier layer against mass transfer of  $\text{O}_2$  and dissolved  $\text{Zn}^{2+}$  in this stage. The oxygen decreases almost uniformly at the same rate across the surface of the zinc coating. The process of Zn products slightly decreases the pH of the solution stabilizing corrosion products like:  $\text{Zn}(\text{OH})_2$ ,  $\text{ZnCl}_2 \cdot 6\text{Zn}(\text{OH})_2$  and  $\text{ZnCl}_2 \cdot 4\text{Zn}(\text{OH})_2$  this happened in solutions where the chloride ions were increases and the pH were controlled with  $\text{CO}_2$  dissolved in the solution from the air (Yadav, et al., 2007).

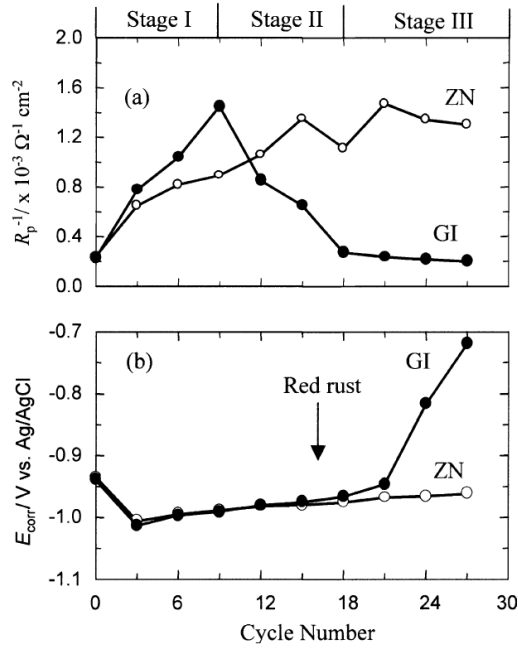


Figure 1 Change in (a) reciprocal polarization resistance  $R_p^{-1}$  and (b) corrosion potential  $E_{\text{corr}}$  of Galvanized Steel GI and Zinc Sheet Zn with cycle number (Yavad, et al., 2007)

In the second stage,  $R_p^{-1}$  decreases after reaching a maximum value and  $E_{\text{corr}}$  change to a positive slope (*Fig. 1*). Accordingly to the study, the reduction of  $R_p^{-1}$  was not caused by the formation of the corrosion products of the galvanized steel. The corrosion proceeds with the dissolution of the zinc layer until reach the Zn-Fe alloy layer is exposed as shown *Fig. 2(b)*. The appearance of yellowish red rust was observed, even in these conditions the zinc coating can act as sacrificial anode under wet surface. If the surface has a thin electrolyte layer during the dry period, the zinc coating loses the ability to act as sacrificial anode, as shown in *Fig. 2(b')*

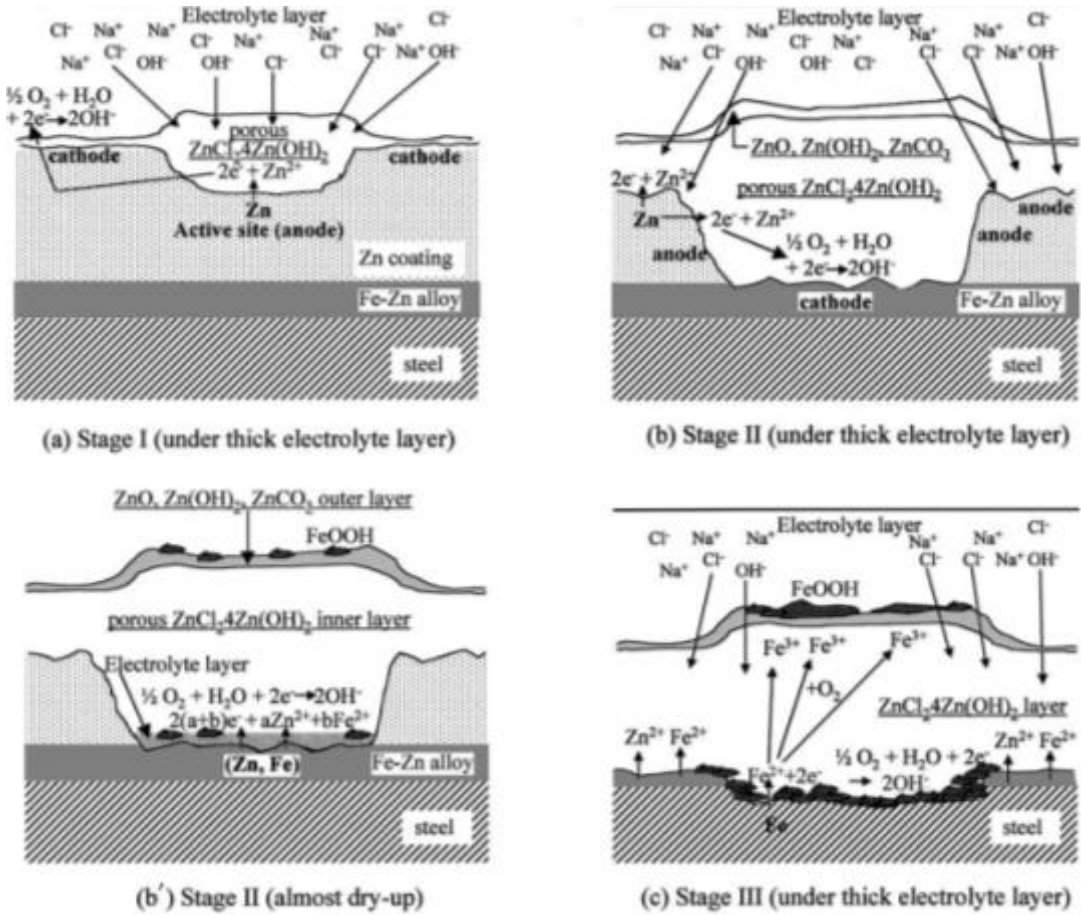


Figure 2 Illustration of corrosion mechanism of galvanized steel (Yavad, et al., 2007)

In the last stage of the corrosion process, underlying steel corrosion begins, but this process may be at a very slow rate. The  $R_p^{-1}$  is almost constant, and the values of  $E_{corr}$  increases dramatically. At this point it is not possible to say that zinc coating or Zn-Fe alloy layer are still present on the steel surface in this stage (Yavad, et al., 2007).

In a different study, a rotating ring disc electrode was used to study oxygen reduction on carbon steel and zinc in a weakly alkaline electrolyte according *Eq. (1)*:  $O_2 + 2H_2O + 4e^- \rightarrow 4OH^-$ . When the zinc coating is covered with the zinc oxide layer,  $O_2$  is reduced to  $HO_2^-$  via reaction on *Eq. (2)*  $O_2 + 2H_2O + 2e^- \rightarrow HO_2^- + OH^-$ . However  $HO_2^-$  may itself and oxidize via *Eq. (3)*  $HO_2^- + H_2O + 2e^- \rightarrow 3OH^-$ . This is possible because 2 electron transfer reaction into hydrogen peroxide or it may be reduced into hydroxide in a 4 electron transfer reaction, which indicates a fast charge (Dafydd, et al., 2005).

### 2.1.1.1 Effect of Anions on Zn

Certain anions promote corrosion for example the  $\text{Cl}^-$ , while other acts as an inhibitor such as  $\text{PO}_2^{3-}$ . At a certain salt concentration, the potential change to noble values and inhibition of corrosion take place. Aal et al. (1999) in a study of zinc produced experiments with  $\text{Na}_2\text{B}_4\text{O}_7$  solution in the absence and presence of  $\text{Cl}^-$  anions with galvanostatic polarization technique. In absence of  $\text{Cl}^-$  anions, the polarization curves are characterized by arresting the zinc oxide products. The low concentration of anions  $\text{Cl}^-$ , has no influence on the passive film formed on the coating surface. The anodic and cathodic process of the zinc corrosion in an alkaline solution  $\text{Zn} \rightarrow \text{Zn}^{2+} + 2e^-$  (4) dissolves zinc and reduces the oxygen molecule as in Eq. (4) and Eq. (1), the zinc hydroxide formed the reaction of  $\text{Zn}^{2+}$  with  $\text{OH}^-$  precipitated on the surface of the coating resulting in a zinc oxide Eq. (5)  $\text{Zn}^{2+} + 2\text{OH}^- \rightarrow \text{Zn}(\text{OH})_2 \rightarrow \text{ZnO} + \text{H}_2\text{O}$  (Aramaki, 2001) [2]. The concentration of  $\text{Cl}^-$  anions is directly associated with the breakdown of the Zn passivity, when chlorite ions react with the passive film to form  $\text{Zn}^{2+} - \text{Cl}^- - \text{OH}^-$  complexes. Once the passivity film breaks, the initiation of the pitting corrosion starts. Addition of tungstate, phosphate or molybdate anions change the breakdown in a noble direction. In contrast, additions of sulphate anions increase the pitting attack (Aal, 2000). The  $\text{Cl}^-$  and  $\text{SO}_4^{2-}$  anions promote the corrosion and the extent of corrosion-promotion is related to their catalytic effect on the reduction of oxygen in the solution (Gouda, et al., 1967). Passivity provides the initiation sites for pitting tough corrosion products ( $\text{ZnO}$ ,  $\text{Zn}(\text{OH})_2$  and  $\text{ZnCO}_3$ ) increase with the progress of the corrosion (Yadav, et al., 2004).

Cachet et al. analyzed the impedance diagrams and concluded that dissolution of the zinc takes place essentially at the base of pores in conductive layer of the oxidation product, which is progressively degraded by anodic current. At more positive potential, a less soluble zinc hydroxide layer contributes to passivity. The passivation is attributed to presence of zinc oxide and other non-stoichiometric compound of the metal (Aal, 2000).

(El-Mahdy, et al., 2000) in a study of the zinc coating conducted experiments to measure the corrosion mass loss in a solution of 0.05 M NaCl and 0.05 M Na<sub>2</sub>SO<sub>4</sub> with different cycles of 1 hour of immersion and 7 hours for drying. The corrosion mass loss with respect to each cycle was described by Eq. 6  $\Delta M = (M_{Zn}/2F) \int_0^{t_N} i_{corr} dt$ .

The calculations of the experiments of zinc in 0.05 M NaCl resulted in two different regions. The first region agrees with Yadav et al. (2004) in the accelerated rate of mass loss until the appearance of red rust, indicating the dissolution of zinc layer and the reduction of oxygen. The corrosion of the underlying steel, after the appearance of red rust, the mass loss rate immediately decreased. The result for the other experiment of Zn in 0.05 M Na<sub>2</sub>SO<sub>4</sub> differs from the corrosion by a chloride solution. During the exposure to the sulfate solution, the mass loss rate remained constant throughout the whole cycles. The X-ray diffraction (XRD) analysis of the corrosion products of the samples exposed to both solutions show that the corrosion products were composed of ZnO, ZnCl<sub>2</sub>·4Zn(OH)<sub>2</sub>, Zn<sub>5</sub>(CO<sub>3</sub>)<sub>2</sub>(OH)<sub>6</sub>, α-FeOOH, β-FeOOH and δ-FeOOH in the 0.05 M NaCl solution and only hydrated ZnSO<sub>4</sub> in the 0.05 M Na<sub>2</sub>SO<sub>4</sub> solution. El-Mahdy et al. attributed the difference in the corrosion behavior between solutions with Cl<sup>-</sup> and SO<sub>4</sub><sup>2-</sup> anions to the difference in Zn precipitates formed on the surface (El-Mahdy, et al., 2000).

### 2.1.1.2 Corrosion of Zn-Fe alloy layer

Phase formed between the Fe and Zn are: gamma (Γ) phase, Fe<sub>3</sub>Zn<sub>10</sub>, delta (δ) phase, FeZn<sub>10</sub> and FeZn<sub>7</sub>, zeta (ζ) phase, FeZn<sub>13</sub>, and the outer phase (η) being a zinc rich solid solution as Fig. 3. The thickness of individual layers of zinc coating plays important role in improves corrosion protection. The corrosion rate decreased with number of layers only up to certain (optimal) number of layers, and then the corrosion increased. Authors have shown that the polarization resistance values increases with increasing Fe content in the zinc phases. The corrosion rate of the Zn-Fe alloy layer is much lower than the zinc coating on iron. It has been reported that the corrosion product of the zinc provides almost 50%

of the corrosion protection of the galvanic coating in atmospheric environment. However, the zinc corrosion products combined with the dissolution of the Zn-Fe layer contributes to a better performance of the galvanic coating (Yadav, et al., 2007).

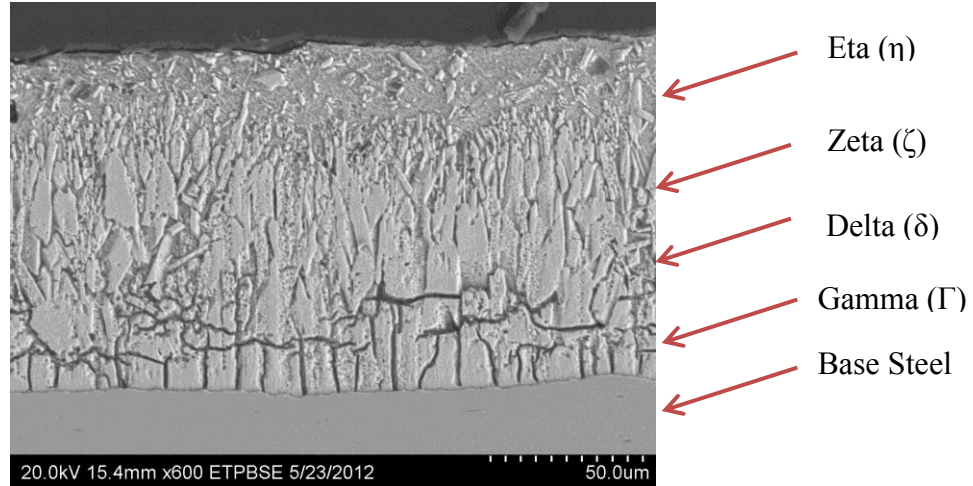


**Figure 3 Hot-dip galvanized steel phases**

In the early stage of the corrosion, alloy side and steel side formed a cathode. The anodic reaction zinc gives  $Zn^{2+}$  and the cathodic reaction up to -700 mV is diffusion controlled by the oxygen reduction  $OH^-$  (Yadav, et al., 2007). The protection efficacy of the zinc coating is related to the defects and failures occurring in a single layer in the deposition process may be neutralized or masked, by the successively deposited layers.

### **2.1.2 Carbon steel oxidation**

Corrosion products of steel and iron consist of hydroxides and oxides *Table 2*. Ferrous ions are the primary corrosion products formed by anodic dissolution. Ferrous ions are converted by precipitation and oxidation reaction into soluble ferric oxy-hydroxide, where Fe-OOH constitutes the most stable product in atmospheric corrosion. The properties of these oxides and hydroxides products depend directly on the surface electrolyte and thus different types of atmosphere. In places where a high concentration of  $Cl^-$  exist like seaside, more  $Fe_3O_4$  and less  $\gamma$ -FeOOH. The rust formed in the presence of  $Cl^-$  is well known to involve  $\beta$ -FeOOH, because the formation of this hydroxide require the presence

of  $Cl^-$  ; study reported that  $\beta$ -FeOOH was mainly at thick parts of rust layer, and was scarce at thin parts and may work as a reservoir of  $Cl^-$  ions (Tanaka, et al., 2010). The rust layer itself would then become porous and introduce chloride ions from outside easily, which promote corrosion. However, chloride ions only played an important role at the initial stage of atmospheric corrosion; as the rust layer grew in thickness, the supply of fresh chloride ions may gradually reduce and as result, the formation of chloride would be slower (Ma, et al., 2009). Thus, the existence of  $\beta$ -FeOOH can be presumed to a high concentration of  $Fe_3O_4$  (Ishikawa, et al., 1998). Magnetite,  $Fe_3O_4$ , may form the oxidation of  $Fe(OH)_2$  or form intermediate ferrous-ferric species such as green rust. Magnetite may also formed by the reduction of FeOOH in the presence of a limited oxygen supply Eq. (6)  $8FeOOH + Fe \rightarrow 3Fe_3O_4 + 4H_2O$ .

Table 2 Chemical compounds found in rust layer

Name	Composition
<b>Oxides</b>	
Hematite	$\alpha$ - $Fe_2O_3$
Maghemite	$\gamma$ - $Fe_2O_3$
Magnetite	$Fe_3O_4$
Ferrihydrite	$Fe_5HO_8 \cdot 4H_2O$
<b>Hydroxides</b>	
Ferrous hydroxide	$Fe(OH)_2$
Ferric hydroxide	$Fe(OH)_3$
Goethite	$\alpha$ -FeOOH
Akaganeite	$\beta$ -FeOOH
Lepidocrocite	$\gamma$ -FeOOH
Feroxyhyte	$\delta$ -FeOOH
<b>Others</b>	
Ferrous chloride	$FeCl_2$
Ferric chloride	$FeCl_3$
Ferrous sulphate	$FeSO_4$
Ferric sulphate	$Fe_2(SO_4)_3$

(Morcillo, et al., 2011)

In a neutral solution basic solution the formation of  $Fe(OH)_2$  may form. In and atmospheres polluted by  $SO_2$  where the surface form a electrolyte of weakly acid the  $Fe(OH)_2$  does not precipitate.

For this reason many authors consider  $\gamma$ -FeOOH and  $\alpha$ -FeOOH are the primary crystalline corrosion product, these corrosion products are formed via electrochemical that takes place in cells of microscopic dimensions with very distic anodic and cathodic areas. In a dry, clean atmosphere the steel surface becomes converted by a 20-50 Å thick oxide film which practically prevents further oxidation. This oxide film consists of an inner layer of  $\text{Fe}_3\text{O}_4$  and outer layer of polycrystalline  $\text{Fe}_2\text{O}_3$ . In different occasions where is present a weakly acid solution the  $\gamma$ -FeOOH transforms to  $\alpha$ -FeOOH depending on the sulfate concentration and temperature.  $\alpha$ -FeOOH seem to be the most stable modification of the ferric oxy-hydroxides. The steel that has been subjected to a long-term oxidation the magnetite usually appears in the inner part of the rust adhering to the steel surface, where reduction of the oxygen may occur. The steel usually corrodes in two regions: the first region that is located next to the steel-rust interface, consist of a dense amorphous FeOOH with some crystalline  $\text{Fe}_3\text{O}_4$  and the second region consist of loose crystalline  $\alpha$ -FeOOH and  $\gamma$ -FeOOH (Mansfeld, 1987).

The yield of  $\text{Fe}_3\text{O}_4$  is dependent on the solubilities of FeOOH, the hydrolysis species of  $\text{Fe}^{3+}$ , such as  $\text{Fe}(\text{OH})_2^+$ , and  $\text{Fe}(\text{OH})_4^+$ , used for the  $\text{Fe}_3\text{O}_4$  formation are given by dissolution of FeOOH. This fact verifies that  $\text{Fe}_3\text{O}_4$  is produced by the reaction of ferric species dissolved from FeOOH with ferrous species in the solution (Ishikawa, et al., 1998). When the steel is exposed, the surface is covered with a 2 to 5 nm thick oxide film consisting in an oxide layer of  $\text{Fe}_2\text{O}_3$ . This film protects the steel from further corrosion. If a small amount of water vapor is present, FeOOH may form. The steel is protected from the corrosion environment by a thin oxide passive film 1 to 4 mm thickness with a composition of  $\text{Fe}_2\text{O}_3/\text{Fe}_3\text{O}_4$ . This is the same kind of film formed when the steel contact dry air or oxygen. The  $\text{Fe}_2\text{O}_3$  layer is responsible for the passivity, while  $\text{Fe}_3\text{O}_4$  provides the basis for a higher oxidation state. The  $\text{Fe}_2\text{O}_3$  layer will not form until the  $\text{Fe}_3\text{O}_4$  existed on the surface for a reasonable period of time. During this period, the  $\text{Fe}_3\text{O}_4$  layer continues to form (Schweitzer, 2010).

The corrosion of galvanized steel in environment with a high concentration of  $\text{Cl}^-$  leads the



formation of zinc corrosion such as ZnO and zinc hydroxychloride  $Zn_5(OH)_8Cl_2 \cdot H_2O$  (ZHC), after the formation of Zn(II) caused by the  $Cl^-$  ions, the formation of  $\beta$ -FeOOH will appear in the rust. Tanaka et al. (2010) explains the influence of zinc corrosion products on the formation of  $\beta$ -FeOOH by synthesizing particles of  $\beta$ -FeOOH in the presence of  $ZnCl_2$ , ZnO, and ZHC ( $Zn_5(OH)_8Cl_2 \cdot H_2O$ ). Analyses with XRD demonstrate that ZnO and ZHC were dissolved during the formation of  $\beta$ -FeOOH. Therefore, the crystallization of  $\beta$ -FeOOH can be inhibited by the inclusion of Zn(II), ZnO and  $Zn_5(OH)_8Cl_2 \cdot H_2O$ , with an inhibition order of  $ZHC \approx ZnO > Zn(II)$  (Tanaka, et al., 2010).

In another study, Tanaka have reported that Fe(III) is hydrolyzed at  $pH \geq 2$  to form steel hydroxides of the form  $Fe(OH)_x^{(3-x)}$ . The pH of the chloride solution with Zn(II) decreases gradually as the solution ages but when ZnO and  $Zn_5(OH)_8Cl_2 \cdot H_2O$  are added to the solution it has a sudden increase to a pH of 2.3 in about 15 minutes of aging and then it decreases rapidly for an hour. The sudden increase in the pH is attributed to the dissolution of the ZnO and  $Zn_5(OH)_8Cl_2 \cdot H_2O$  compounds, which then causes an acceleration in the formation of  $Fe(OH)_x^{(3-x)}$  resulting in the rapid reduction of the pH for an hour. The  $Fe(OH)_x^{(3-x)}$  hydroxides are condensed to form amorphous iron oxides and hydroxides that originate with the formation of  $\beta$ -FeOOH particle. After the decrease in pH, the hydrolysis of Fe(III) is inhibited and the crystallization and particle growth of  $\beta$ -FeOOH is suppressed. Also, the ZnO and ZHC in the solution interfere in the crystallization and particle growth of  $\beta$ -FeOOH as it was mentioned above (Tanaka, et al., 2010).

### **2.1.2.1 Effects of anions in the formation of $\beta$ -FeOOH**

As discussed before the phase and crystallization of various iron oxide formed in corroding solution depended on the atmospheric environment forming an electrolyte layer, such as different anions, concentration of pH and temperatures. It is well know that the  $\beta$ -FeOOH requires the presence of halide ions like  $Cl^-$  to achieve its formation, but the formation of its structure can be influenced by the existence of different anions such as:  $SO_4^{2-}$ ,  $NO_3^-$ ,  $HPO_4^{2-}$  and  $SiO_3^{2-}$  (Ishikawa, et al., 2005).

The location of  $\beta$ -FeOOH in the rust layer is still open in discussion. According to many works, akaganeite forms in the inner part of the corrosion layer, near to metal-oxide interface of corroded artefacts. But akaganeite was also identified on the external part of thick rust layers formed in the carbon steel exposed to air in a coastal region. This is caused for the excess concentration of  $\text{Cl}^-$  ions in the marine atmosphere. However in presence of sulfate anions,  $\alpha$ -FeOOH is the most stable phase of ferric oxyhydroxide. According to Remazeilles et al. (2007) the formation of  $\beta$ -FeOOH occurs in the presence of concentrated chloride ions in thin electrolyte film created during the drying of the solution on the surface of the steel during the atmospheric corrosion (Remazellines, et al., 2007).

Ishikawa et al. (2005) showed some analysis performed on the XRD of  $\beta$ -FeOOH obtained through the oxidation of Fe(II). During this analysis the peaks of  $\beta$ -FeOOH lower the intensity after the addition of  $\text{SO}_4^{2-}$  and  $\text{HPO}_4^{2-}$  reduce the crystallinity of the particles. The addition of  $\text{NO}_3^-$  and  $\text{SO}_4^{2-}$  do not affect the cristallinity of the particles. A small amount of  $\text{SiO}_3^{2-}$  curiously promotes the particle growth by the generation of nuclei from the hydrolysis species of  $\text{SiO}_3^{2-}$ . The XRD results of a similar  $\beta$ -FeOOH sample obtained through the hydrolysis for Fe(III) demonstrated similar results to the Fe(II)-oxidation, except for the products in the presence of  $\text{SO}_4^{2-}$ , which showed an improved crystallinity at low  $\text{SO}_4^{2-}/\text{Fe(III)}$  ratios (Ishikawa, et al., 2005).

## 2.2 Electrochemical methods for studying corrosion

Electrochemical processes consist of anodic and cathodic partial reactions are coupled with an electronic current in the metal and ionic current in the electrolyte (Marcus, et al., 2006). The use of electrochemical impedance spectroscopy (EIS) techniques acquired very useful data that explain mechanism, which could not be obtained through traditional direct current (DC) techniques. For example, the measurement of corrosion rates in a low conductivity solution (Mansfeld, 1990). However, some electrochemical for long term corrosion evaluation on monitoring, electrochemical noise requires a coupling of EIS and DC techniques to ensure a proper mechanism study.

### 2.2.1 Polarization resistance of galvanized steel

Electrochemical reaction kinetics transferring electrons and determines the rate of corrosion of a metal exposed to a corrosive electrolyte layer. On the other hand, thermodynamics predict the possibility of corrosion, but it does not provide information on how slow or fast corrosion occurs. If the electrochemical system (electrode and electrolyte) is at equilibrium, then the net rate of reaction is zero. In comparison, reaction rates are governed by chemical kinetics, while corrosion rates are primarily governed by electrochemical kinetics. Electrochemical kinetics of a corroding metal can be characterized by determining the three polarization parameters, such as corrosion current density ( $I_{\text{corr}}$ ), corrosion potential ( $E_{\text{corr}}$ ), and Tafel slopes ( $\beta_a$  and /or  $\beta_c$ ). The polarization resistance method, based on the electrochemical concepts, enables determination of instantaneous interfacial reaction rates such as corrosion rates and exchange of current densities from a single experiment. The polarization resistance  $R_p$  is defined as the slope of the current density-potential curve near the corrosion potential  $E_{\text{corr}}$ , the Tafel equation  $i = i_0 \frac{nF}{RT} \Delta E$  is applicable to the region where the values of polarization are high. At low values of polarization, the dependence of current on polarization is usually linear. This linear region is called polarization resistance due to its formal similarity to Ohm's law (Kelly, et al., 2003).

At an intermediate resistance circuit, some current begins to flow and the potential of both half-cells reaction move slightly toward each other. The resistance of the circuit depends on a number of factors, including the resistivity of the media, passive film, and the metal itself. Once the corrosion current is determined, the current density can be calculated by determining the surface area. By using Faraday's laws, corrosion rate in terms of metals loss per unit time (mm/y) can be determined. However, the polarization resistance is more useful than just calculating the corrosion rates. An extended polarization analysis can be used to predict the type and severity of corrosion. As the polarization increases, the corrosion decreases. Understanding the changes of the atmospheric changes on polarization can offer insight into controlling corrosion (Schweitzer, 2007).

The polarization resistance of a metal-electrolyte system and the pitting can be determined using at least two electrode systems. Subsequently, the corrosion rate of a metal can be calculated by using a function of the form  $I_{corr} = f(\beta, R_p) > I_0$ . The techniques are: linear polarization, which covers both anodic and cathodic portion of the potential  $E$  versus current density  $I$  curve for determining  $R_p$ . Tafel extrapolation technique, takes into account the linear parts of the anodic and cathodic curves for determining  $R_p$ . For electrochemical impedance spectroscopy (EIS), the output of a Nyquist plot considers the charge transfer or diffusion control process, which can be used to determine the  $R_p$ , which result in the reciprocal of corrosion current  $I_{corr}$  (Perez, 2004).

Walter et al. (1975) studied the corrosion rate ( $I_k$ ) determined by curing in a near neutral solution by Tafel slopes as shown in *Fig. 4*. Under this condition the rate determining step is controlled by the charge transfer of metal ions crossing the electrical double layer. However, this technique cannot be easily applied to near neutral unmixed solution, because the mass transferred  $H^+$  ions,  $O_2$  or  $M^{Z+}$  control the reaction at electrode surface (Walter, 1975).

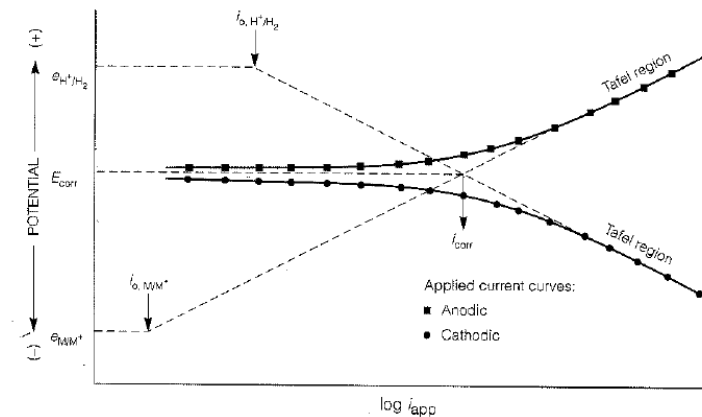


**Figure 4 Back extrapolation of a linear section of anodic and cathodic polarization curves (Jones, 1992)**

If the mass transfer effect the anodic and cathodic partial reactions, the corrosion potential and the corrosion density are complicated by the mass-transfer over potential of anodic and cathodic partial reactions, as Walter explained for a zinc coating corroding in a near neutral solution. The partial anodic reaction diluted by the concentration of metal ions in the vicinity of the electrode surface, increased the corrosion potential and decreased in the current density. The effect of mass transfer can lead to

erroneous results (Walter, 1975).

Walter (1976) identifies several possible sources of error in calculating corrosion rates from data acquired in low polarization data experiments. These errors are: the incorrect inclusion of the diffusion portion of the potential response, the neglect of the curvature in the polarization curve in the vicinity of the corrosion potential, the neglect of the metal ion deposition when the corrosion potential nears the equilibrium potential, and the values for the anodic Tafel slope for a zinc coating containing impurities may vary during the experiment and may also differ from the literature values of pure zinc. The polarization curves for zinc and zinc coatings showed a curvature in polarization curves near the corrosion potential, was acquired to build the polarization resistance curve. The range of the linearity, based on a 5% deviation of the polarization curve from linear behavior at the corrosion potential approximated 1.5 mV for zinc and zinc coatings. In the case of such a small linear range, results obtained outside of this range may result in an inaccurate corrosion rates. The increase of metal ions in the solution may increase the metal equilibrium potential, defined as the difference between the corrosion and equilibrium potentials resulting from accumulation of metal ions in the solution from soluble corrosion products. The values of anodic Tafel slopes for zinc have been shown to change over the period of sample immersion suggesting that the calculation of the corrosion rate may become more accurate with long-term exposure (Walter, 1976).

### **2.2.2 Electrochemical Impedance Spectroscopy**

Electrochemical impedance spectroscopy (EIS) has become a mature technique proven to be extremely effective in mechanistic studies of a wide variety of corrosion process. The technique measures response of an electrode to a small-amplitude alternating potential signals of extensively frequency applied at a fixed potential. Evaluation of the experimental spectra as a function of the frequency ( $f$ ) of the signal in Bode plots, which are the preferred display of EIS data, reveal one or more time constant. In the Bode plots the phase angle  $\Phi$  and the logarithm of the impedance modulus  $|Z|$  are

plotted versus  $\log$  of  $f$ . The sensitive indicator of the system properties is the maxima and minima of  $\Phi$  and the position at specific frequency (Marcus, et al., 2006). Nishikata et al. 1995 used the EIS technique to study the corrosion metals covered with a thin electrolyte layer. They found from EIS data obtained from a metal in contact with a thin electrolyte layer interface can be described by a transition line model (TLM). From the TLM model, EIS information can be analyzed to detect the nonhomogeneous current distribution over a working electrode which leads to erroneous monitoring of the corrosion rate (Nishikata, et al., 1995). During the atmospheric corrosion the dissolved salts and gases form a thin electrolyte layer deposited on the surface of the metallic coating. The thickness of this thin electrolyte layer plays an important role in the atmospheric corrosion rate of the metal. As noted previously, the thickness of the solution affects the oxygen diffusion through the electrolyte controlling the rate of the cathodic reaction of the corroding metal and the solubility of the corrosion products, affecting the concentration of anions. Also, the thin electrolyte layer dries, the concentration of the anions increases with usually a change in the solution pH. Therefore, a thin electrolyte solution complicates the corrosion mechanism of metals differing from that in bulk solutions.

Nishikata et al. 1995 reported that some previous investigations using polarization curves and impedances of metals in thin electrolyte layer have neglected the contribution of the current distribution over the surface of the working electrode. To take into account for the current distribution, Nishikata et al. (1995) used TLM, in which the current distribution over the working electrode is considered. With a transmission line, the EIS analysis model provides the effects of current distribution over the surface of the electrode. On a plot of the phase shift angle ( $\theta$ ), the phase angle must pass further than  $-45^\circ$  so the current distribution becomes uniform especially at low frequencies, as shown in *Fig. 5*. Accordingly, the polarization resistance obtained can be used to acquire an accurate corrosion rate (Nishikata, et al., 1995), as exemplified in the EIS data obtained for stainless steel with two different electrolyte thicknesses (10 and 1100  $\mu\text{m}$ ) of 0.1 M NaCl, the slope indicates the time constants differs specially the

effective capacitance. The impedance for 0.1 M NaCl with a thickness of 10  $\mu\text{m}$  shows the effect TML type frequency dependency in the frequency range of 1Hz-10kHz.

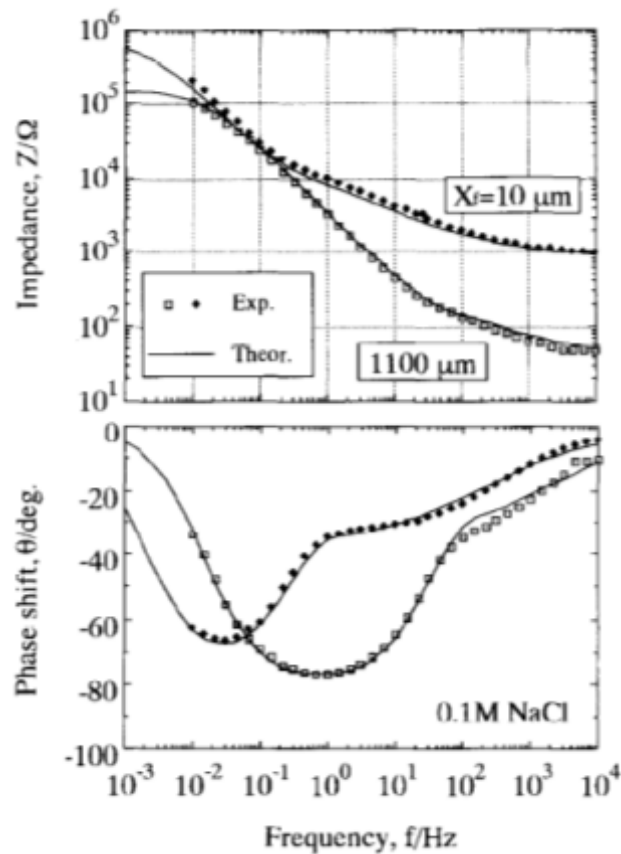


Figure 5 Experimental bode diagram and fit to the TML model for Type 304 stainless steels covered with a 0.1 NaCl solution layer (Nishikata, et al., 1995).

Li et al. (2010) used EIS technique to investigate atmospheric corrosion in a laboratory simulated environments with variable relative humidity (RH) and fixed chloride content. During this study the impedance response at 5-30% RH, NaCl particles remain unaltered and no corrosion products formed on the electrode with the adsorbed water having less than one monolayer on the surface suggesting the existence of dry conditions. With the rate of 60% RH, two monolayers of water were absorbed causing a variation on the impedance measurements. Indicating the resistance increases between the metal and the electrodes and the capacity is due to the absorption ability of electrolyte layer. The surface conductance increases with increasing RH as a result of the surface accumulation of absorbed water molecules. When the RH is up to 70-100%, the water is absorbed, the particles of NaCl dissolved on the surface of

the metal, and the electrolyte causes atmospheric corrosion leaving corrosion products on the surface. One problem associated with EIS for the study of atmospheric corrosion is the uneven distribution of the thin electrolyte layer (Li, et al., 2010).

### **2.2.3 Electrochemical Noise**

The analysis of the spontaneous fluctuation of current and potential known as electrochemical noise (EN) is an applicable method for monitoring corrosion. EN monitors the current between two identical electrodes, as well as acquiring the corrosion potential of a single electrode. (Kelly, et al., 2003).

During the late 1970s, the instrumentation was improved and the design of low-noise amplifiers and regulation devices was possible. The very low amplitude of the EN generated by most corrosion processes in the high-frequency range investigated at that time, was about 1 Hz and 10 kHz (Marcus, et al., 2006). The characterization of statistical properties of EN was extended; while the mean and standard deviation of random signals were currently measured by using analog instrumentation, such as a root mean square (RMS) voltmeter, the correlation function in the time domain and the power spectral density (PSD), or its squared root, named amplitude spectral density. By taking the Fourier transform (FT) of the current-time series for example, the PSD was derived. (Marcus, et al., 2006).

In some investigations the EN in corrosion was studied under potentiostatic or galvanostatic control. During the galvanostatic mode the potential of the electrode under the test was fixed versus a reference electrode (RE), and the fluctuation of the current flowing through the electrode were recorded, this is called electrochemical current noise (ECN). A different approach of ECN measurements has been developed for investigation at the corrosion potential, by coupling two freely corroding electrodes through a zero-resistance ammeter (ZRA). This allows the fluctuation of the coupling current to be measured without any RE, which is a great benefit during the field experiments. The other improvement is that the mean current flowing between identical electrodes remains close to zero, while for a single



electrode potentiostatically controlled versus RE, any change in open circuit potential of the electrode tends to polarize it out of the corrosion potential (Marcus, et al., 2006).

Al-Mazeedi and Cottis et al. 2004 used the EN parameters as indicator of corrosion type, using a three electrodes technique, where two of the electrodes were working electrodes measuring the electrochemical current noise using a zero-resistance ammeter (ZRA) (Al-Mazeedi, et al., 2004). At the same time the potential is measured between the two working electrode pair relative to a reference electrode. The area of the working electrodes plays an important role in the monitoring of the potential noise since the potential noise of the third working electrode may be larger, if it is used as a reference electrode (Cottis, 2001). The study assumed that during the analysis, there are a large number of events occurred in each calculation intervals, so the calculation sample with a long time period interval should be at the low frequency. For this reason, the best method of estimations of the shot noise parameters is using the low frequency power spectral density (PSD) of the potential and the current (Al-Mazeedi, et al., 2004). In other investigation, Mansfeld and Lee et al. (1997) mention that the determination of spectral noise plots in which  $\log R_{sn}$  (spectral noise resistance defined as the standard deviation of the potential divided by the standard deviation of the current) is plotted vs.  $\log f$  similar to bode plots, can only be done if the potential-current noise data are obtained simultaneously. The spectral noise resistance is defined as the dc-limit of the spectral noise plot. The authors also noted that the main problem in the analysis of electrochemical noise data is the frequency dependence of  $R_n$ . In order for  $R_n$  to be equal to  $R_p$  as it was assumed by Skerry et al. (1991),  $R_n$  cannot depend on the frequency, since  $R_p$  is defined in Eq. 7 as for  $R_n$  and  $R_p$  to be equal, the potential and current PSD plots must have equal slopes  $R_p = \lim_{f \rightarrow 0} (|Z(f)|) - R_s$ . If the slopes are different,  $R_n$  can provide information on the degradation of the coating, but cannot be related as a specific coating property (Mansfeld, et al., 1997).

The effect of the electrode area on electrochemical noise measurements is yet to be fully established. However, it is considered that the current noise amplitude is proportional to the electrode's

surface area, assuming that the potential noise is produced by the effect of current noise on  $R_p$ . Therefore the potential noise also depends on the area of the electrode with the assumption that the current noise is caused by a large number of uncorrelated sources. Therefore, the most common approach to report the electrochemical noise measurements is by specifying the area of the electrode used for the measurements (Cottis, 2001).

### **2.2.3.1 PSD Acquisition Methods**

Two methods are commonly used to estimate the power spectral density in electrochemical noise studies: the Fourier transform in the form of FFT and the maximum entropy method (MEM). The FFT produces noisy spectra, while the MEM produces smoother spectra. However, FFT can be smoothed and the MEM will produce noisier spectra if a higher order is used. The MEM has been applied to corrosion studies mainly to study pitting in aluminum, mild steel, and iron. The MEM has some advantages over the FFT: MEM is faster than the FFT, because MEM does not require ensemble averaging, so acquisition in a single time is sufficient; MEM gives smoother spectra; allowing computation of the spectrum at frequencies lower than the inverse of the acquisition time, which is the lowest frequency calculated by the FFT (Bertocci, et al., 1998). A disadvantage of the MEM is the uncertainty introduced by the arbitrary choice of the order  $M$ , which is the number of coefficients used in the computation. The computation times of the MEM and FFT algorithms may be neglected in the corrosion application compared to extended acquisition times required for corrosion monitoring, so that measuring an FFT spectrum is  $K$  times longer than measuring an MEM spectrum. For featureless spectra, such as those usually measured below 1 Hz in corrosion studies, the choice of  $M$  may be not critical. In *Fig. 6* compare the PSDs measured on white noise FFT and MEM are shown in the *Fig. 6*. The FFT technique does show a long PSD fluctuation compared to the MEM technique especially with increasing order. However, the MEM techniques shift the PSD ( $v^2/Hz$ ) to higher values (Marcus, et al., 2006).

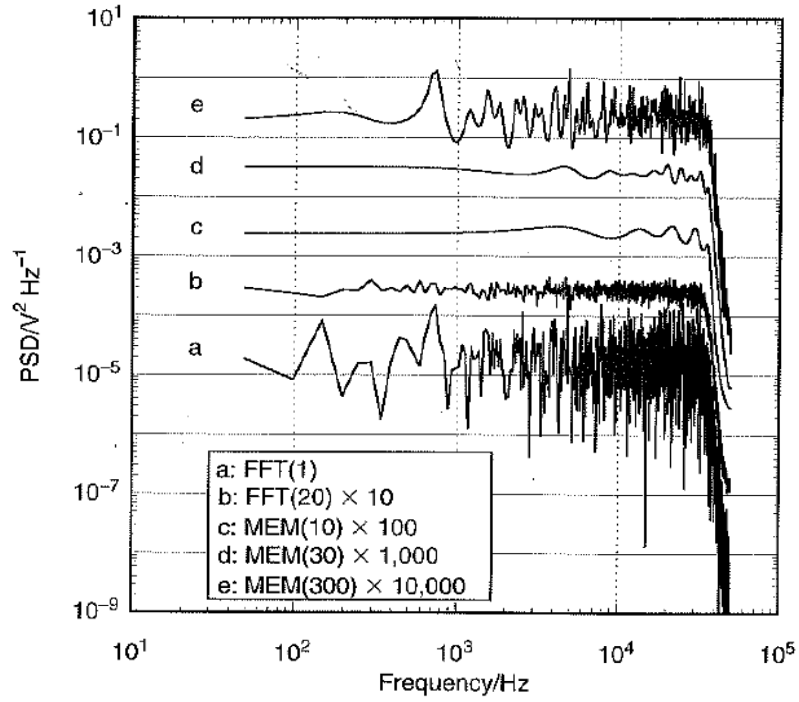


Figure 6 Comparison of MEM and FFT on white noise (Bertocci, et al., 1998).

The PSD is defined most of the time as the Fourier transform of the autocorrelation function. However, is based on the periodogram method by the mean of Cooley-Tukey FFT algorithm Eq 8.

$$\psi(f) = \frac{2}{T} \frac{1}{K} \sum_{j=1}^K |I_j(f)|^2 \quad (8)$$

Where  $f$  is the frequency,  $I_j(f)$  the Fourier transform of the elementary time recording  $I_j(t)$ ,  $T$  the acquisition time, and  $K$  is the number of time recording. This method has the advantage of being simple, easily implementable on a computer, and, above all, applicable to a large class of random signals. However, even with these advantages, the FFT needs, to obtain accurate spectra, to average over  $K$  squares of the modulus of the Fourier transform of  $I_j(t)$ . Therefore, the periodogram method will be designated as FFT( $K$ ), but with this leads to the following drawbacks: 1. The time to acquire the data is multiplied by  $K$  compared to a method that would need only one acquisition. 2. It is appropriate only if the time signals are reproducible, that is, if several acquisitions can be recorded during the same

experiment (Bertocci, et al., 1998).

Similar to the FFT analysis, MEM technique estimates by the direct method, in which the spectral estimation is made on the signal samples, or an indirect method, in which the PSD is estimated through the autocorrelation function. The MEM is an estimation of the PSD suggested by information theory. It is assumed that the sample data  $x(n)$ , can be described by autoregressive model Eq 9.  $y(n) = xn - a_1y(n - 1) - a_2y(n - 2) - \dots - a_My(n - M)$  Where  $y(n)$  is the estimated value of  $x(n)$  and  $M$  the order of the model (Bertocci, et al., 1998).

Huet et al. (1998) mentioned that both the FFT and MEM methods are inaccurate in calculating the PSD for non-stationary systems. Analyses of the electrochemical noise data of these systems, show that the erroneous spectra can be identified easier in the FFT than with the MEM method. During analyses of non-stationary systems, windowing becomes very necessary since other methods such as moving average, polynomial fitting and linear regression cancel part of the fluctuations and therefore alter the PSD. Windowing implies the multiplication of the time record by a function that shrinks to zero at the beginning and end of the time window and is equal to one in the middle. This reduces the confusion of low frequencies as high frequencies and eliminates the drifting without the altering the PSD (Bertocci, et al., 1998).

## 2.3 Fe-Zn phase equilibria and kinetics

When the substrate steel is immersed in the liquid zinc bath, a number of reactions occur depending upon the bath composition and the solutes found in the steel. The Fe-Zn system has been the subject of a number of review papers and the phase diagram has been modified several times, especially the zinc-rich section, since it was presented in 1938. The most widely accepted iron-zinc equilibrium phase diagram as assessed by Kubachewski and Massalski (1986) is presented in *Fig. 7*. The iron is submerged in a zinc bath that is normally at 450-490 °C, according to the phase diagram. Horstmann (1978) proposed that the following phases should be formed, zinc saturated  $\alpha$ -iron, gamma ( $\Gamma$ ) phase

layer, gamma<sub>1</sub> ( $\Gamma_1$ ) phase layer, delta ( $\delta$ ) phase layer and an eta ( $\eta$ ) phase layer (Horstmann, 1978). Fig. 8 shows the Zinc rich part of the Fe-Zn equilibrium phase diagram by Kubachewski.

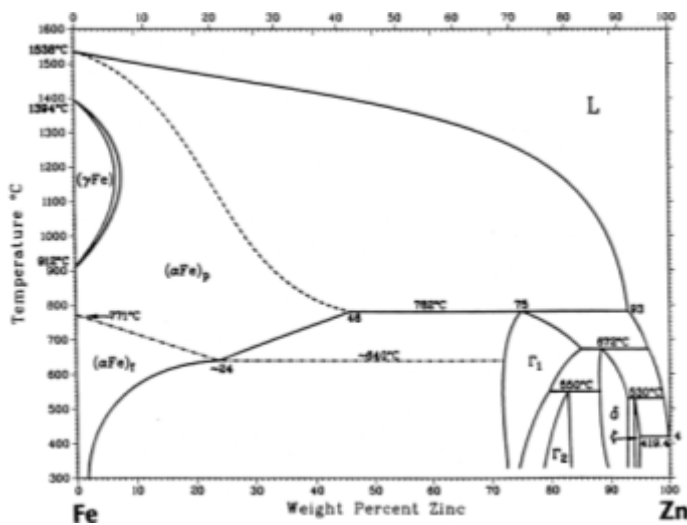


Figure 7 Fe-Zn equilibrium phase diagram (Kubachewski, et al., 1986).

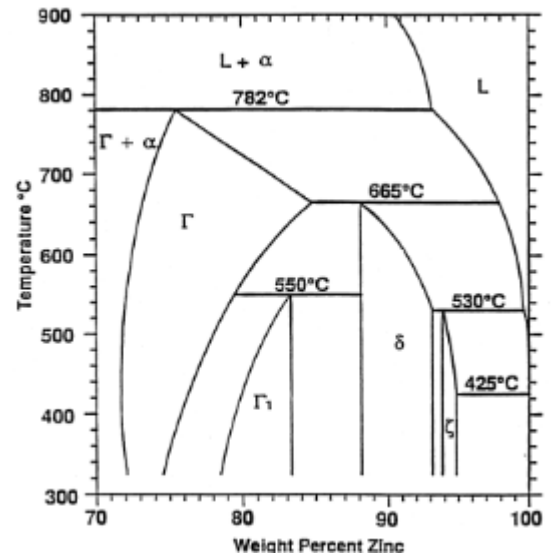


Figure 8 Zn Rich part of the Fe-Zn phase diagram (Kubachewski, et al., 1986)

The sequential formation of the Fe-Zn phases originate at the zinc-steel interface beginning with the zeta ( $\zeta$ ) phase layer, followed by the delta ( $\delta$ ) phase layer and after some incubation the formation of the gamma ( $\Gamma$ ) phase layer. Fig 9 shows in an optical micrograph but the gamma layer is so small that the layer is assumed to contain both  $\Gamma$  and  $\Gamma_1$  phase layers.

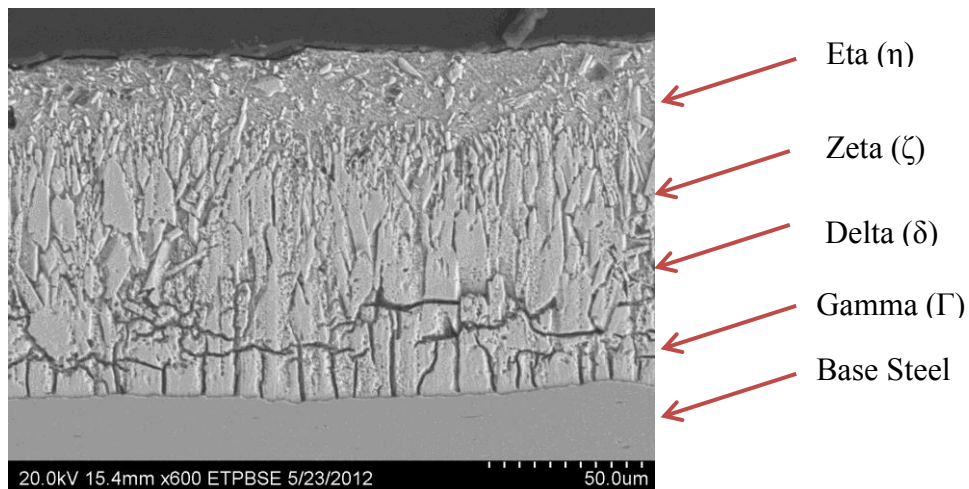


Figure 9 Hot-dip galvanized steel phases

The phase layer development of the Fe-Zn system starts with the zeta ( $\zeta$ ) phase formation, immediately followed by the formation of the delta ( $\delta$ ) phase at the  $\alpha$ -iron/ zeta ( $\zeta$ ) phase interface. The zeta ( $\zeta$ ) and delta ( $\delta$ ) phases form a continuous layer after five seconds immersion, however the gamma ( $\Gamma$ ) phase was found to form after 30 seconds incubation. The zeta ( $\zeta$ ) phase layer has two layers ( $\zeta_1$  and  $\zeta_2$ ) depending on the saturation of Fe in the alloy melt. The zeta phase grows in a columnar morphology that is saturated with Fe, the continued growth of these crystal form a new kind of zeta phase ( $\zeta_2$ ). If the zinc melt is supersaturated with iron, the sufficient formation of these zeta phase crystals saturated with iron can lead to the formation of these crystals in the melt, the  $\zeta_2$  will be separated by the solid zinc  $\eta$  phase, as it can be seen in *Fig. 9* (Marder, 2000).

## Chapter 3: Methodology

### 3.1 Galvanized steel electrode preparation

The galvanized steel strands were cut in symmetrical sections avoiding any ribs or scratches and sections that are straight enough to machine into electrodes. Sections of galvanized steel segments were selected, and then the sections were machined in a Hass super mini-mill computer numerical control (CNC), programmed to create an area of  $1 \times \frac{1}{2}$  cm, as shown in *Fig 10*. The CNC used a  $\frac{1}{4}$  in. four flute end-mill made of tungsten carbide in a cobalt matrix. Coolant was used during the whole machining process with the CNC to avoid material heating, which would change the microstructure of the metal such as grain size and consequently the corrosion characteristics. The spin and feed rates of the CNC were also fixed to ensure the zinc coating was not damaged during the machining process.

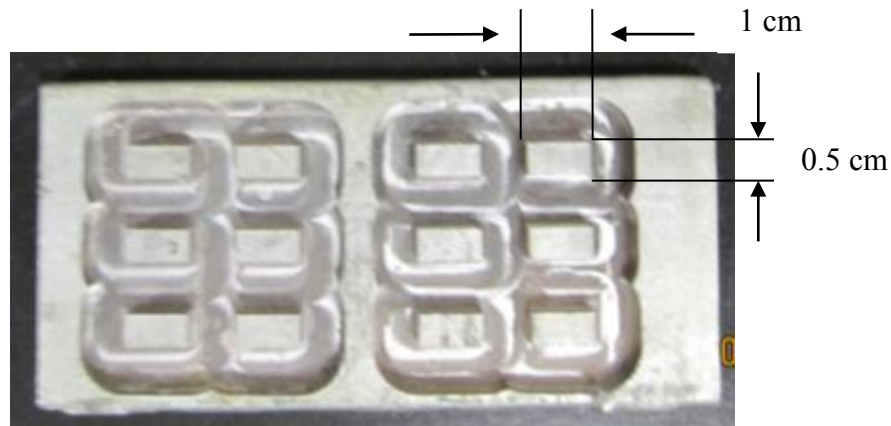


Figure 10 Galvanized steel plate after CNC machining.

After CNC machining of the galvanized steel plates, the electrodes were cut with an abrasive wheel. Water was used to keep the plate cool during the cutting of the electrodes. In this step of the process, the electrodes were cut as close as possible to the electrodes. The edges of the electrodes were then detailed with a grinder.

The final step in the processing of the galvanized steel electrodes consisted in machining the height of the electrode to a height of 0.170 in. This step is used to ensure the electrode will be flushed after the press fitting into the Delrin pocket with a depth of 0.20 in. along with the copper cable used for

data acquisition. The machining of the height of the electrode also allows the copper wire to contact the steel instead of zinc, which improves the conductivity between the electrode and wire.

### 3.2 Delrin coupon preparation

A 1 1/4 in. diameter Delrin rod was cut into segments of 2 in. of length and the sections are then machined with a CNC programmed to create a ridge of 0.02 in. and 3 pockets of 1 x 1/2 cm. and 0.2 in. in depth. The Delrin rod was phased with a 1 in. two flute end-mill, and the pockets were machined with 1/4 in. 4 flute end-mill, then detailed with a 1/8 in. 4 flute end-mill. During the machining of the Delrin coupon, coolant was used to prevent the Delrin from burning. The 2 in Delrin sections are machined on both sides.

After the segments have been machined on both sides, they were cut in half with a vertical saw to create two separate Delrin coupons. The final height of the Delrin coupons was machined with a milling machine. The reason for reducing the height in the laid machine before using the milling machine is due to the elasticity of the material. If the feeding of the material is too much in the milling machine, would rip the coupon out of the vice. Finally, the holes to insert the copper cables into the Delrin coupon were machined with a milling machine and a 1/16 in. bit, as shown in *Fig 11*.

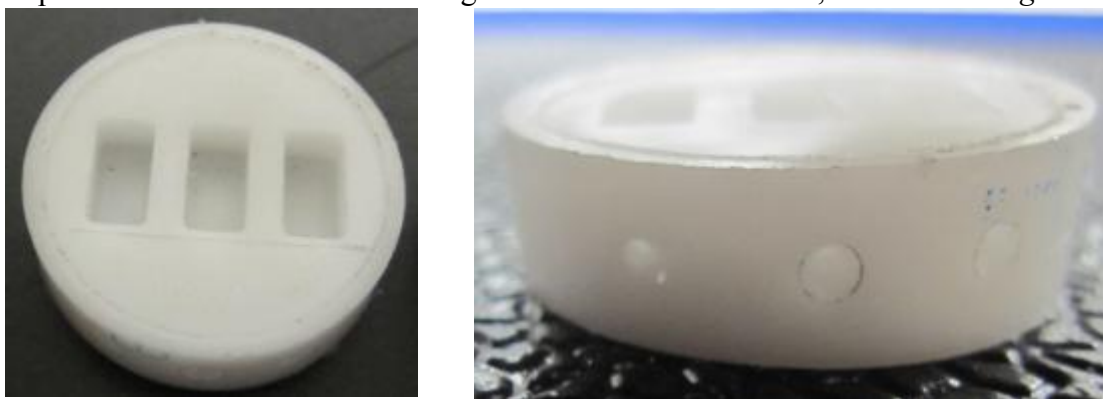


Figure 11. Finished electrode coupon, and side view of a finished electrode coupon with cable holes.

### 3.3 Electrode coupon assembly

Before the working electrode was press fitted into the Delrin coupon, the edges of the working electrode were slightly ground to enhance the guiding of the electrode through the Delrin during the



press fitting process. The electrodes were cleaned in an ultrasonic cleaner with acetone for 30 minutes to remove any residual contaminants from the machining process. The Delrin coupons were also cleaned with acetone. The copper wire was inserted into the coupon and spread inside the pocket to ensure good contact with the electrode. Prior to press fitting of the electrode, two drops of epoxy were poured into the coupon's pocket to seal the electrode sides and prevent crevice corrosion. The electrode was press fitted carefully so the galvanized steel was not damaged in the process. After the electrodes were press fitted, pressure was applied with a hydraulic press to ensure the electrodes are driven to the bottom of the Delrin pocket. Finally the electrodes were cleaned with a cotton cloth saturated with acetone to remove any epoxy that may have made it to the electrode's surface. After some time has been allowed for the epoxy to dry (2 to 3 hours), the cables were sealed so that they do not corrode during the experiments.

### **3.4 Electrode positioning structure**

A plexiglass structure was built to allow for the accommodation of the electrodes inside a 1 liter beaker glass, as shown in *Fig. 12*. This structure ensured that the electrodes were always in the same position during the electrochemical experiments. The plexiglass structure also aids to position the counter electrode in a mesh position with the reference electrode in the middle of the counter electrode.

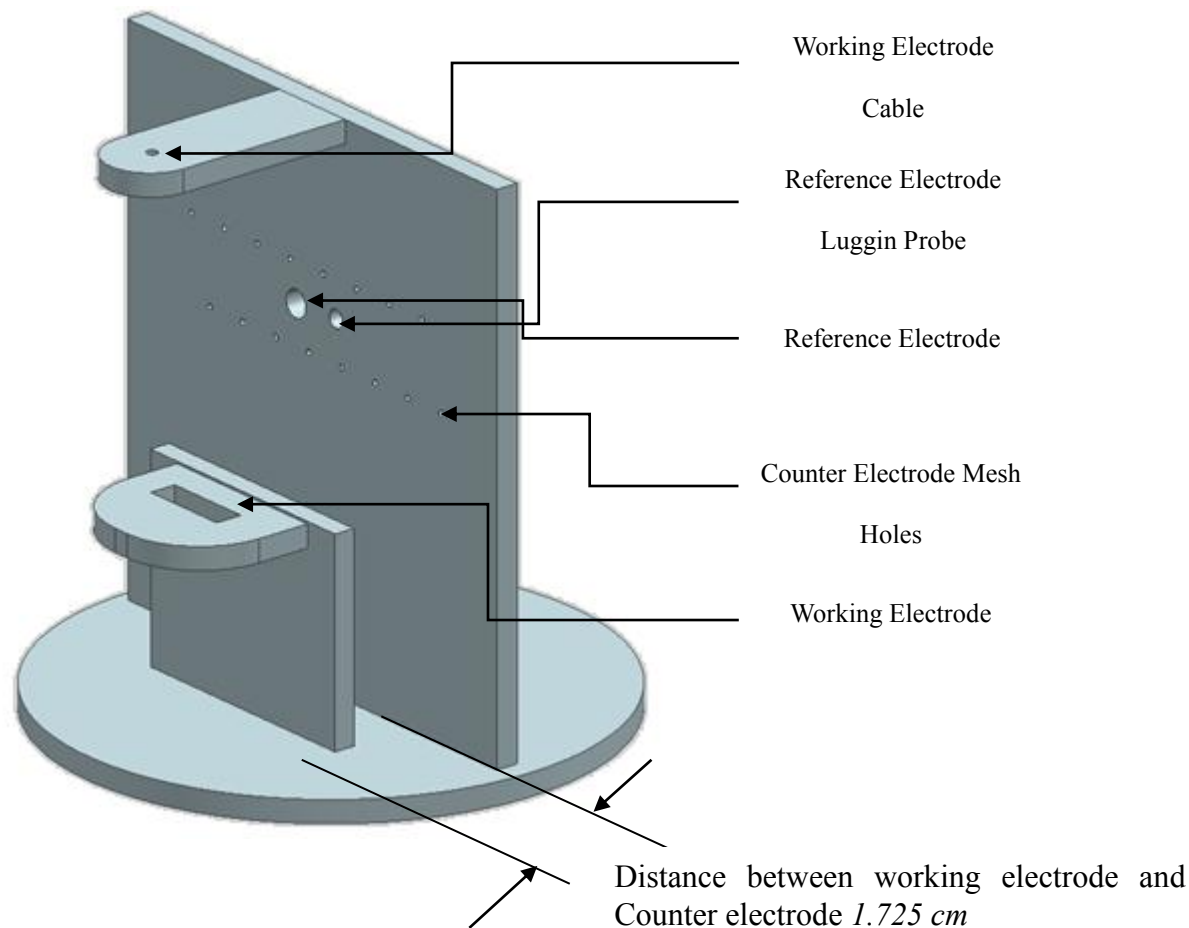


Figure 12. Electrode positioning structure

### 3.5 Polarization scan experiments setup

Polarization scan were acquired at different NaCl molarities concentrations to obtain electrochemical data for the calculation of corrosion rates and mass loss. The electro potential was acquired from the measurements between the working electrode and the reference electrode, and the polarizing current was measured between working electrode and counterelectrode. The polarization scans provided Tafel behavior of the system consisting of the anodic and cathodic polarization curves which ideally are symmetrical about  $E_{\text{corr}}$  when  $|\beta_a| = |\beta_c|$ , as shown in *Fig. 4*. However for corrosion in metals, the Tafel slopes are almost never equal because of the different anodic and cathodic half-cell reactions, which compose the mixed potential  $E_{\text{corr}}$ . The polarization scans were performed with

galvanized steel as the working electrode, Ag/AgCl saturated with KCl as the reference electrode and a Pt wire as the counterelectrode.

### 3.6 Electrochemical impedance experiments setup

The electrochemical impedance measurements were attained to find the solution resistance at different molar concentration of NaCl in deionized water, as well as the polarization resistance. The electrochemical impedance experiments illustrate the electrochemical behavior of the electrode to create an electric equivalent circuit representing the metal-solution interface and interphase.  $R_s$  is the ohmic or uncompensated resistance of the solution between the working and reference electrodes.  $R_p$  is the polarization resistance or charge-transfer resistance at the electrode/solution interface. The effective capacitance at this interface is shown in *Fig. 13*.

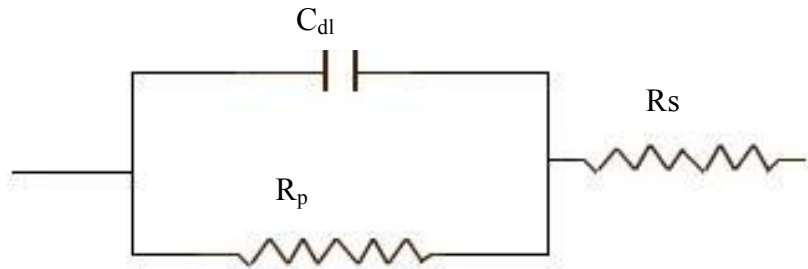


Figure 13 Equivalent circuit describing one time constant.

With increased exposure time to aggressive environment, ionic conditions pathways through the coating shorts the coating capacitance, and resistive impedance develops. Once electrolyte contacts bare metal, faradaic reaction occurs and corrosion is underway. Several equivalent circuit models are commonly used to analyze EIS data from degraded coatings. The most common circuit is shown in *Fig. 14*. In this model, the impedance response of intact areas of the coating is represented by a capacitor,  $C_{ox}$ . There is a coating resistance, but it is usually too large to measure. The impedance response at defects varies from sample to sample but falls into general categories.  $R_{ox}$  represents the pores oxide resistance,

which is the ionic resistance to current flow between the bulk electrolyte and the metal- film interface. This pathway exists through microscopic pore defects, and through the pore space containing water and ions in the polymer film. This circuit depends in the impedance behavior at low frequencies. In the case where the spectrum achieves a DC limit  $R_s + R_{ox} + R_p$ , corrosion occurs under charge transfer control (Marcus, et al., 2006).

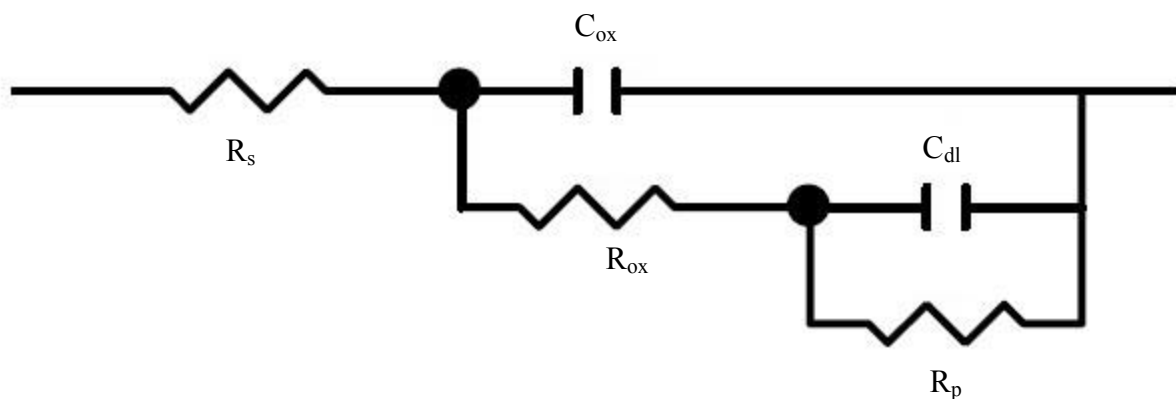


Figure 14 Equivalent circuit describing two time constant

For the reference electrode, a Pt electrode contained in a Luggin-probe was connected in parallel to an Ag/AgCl reference with a 100  $\mu$ F capacitor. The coupled Pt-Ag/AgCl reference electrode allows the stabilization of the electrochemical impedance measurements at high frequencies. The necessity for this modification was brought upon by problems such as the phase shift introduced by the potentiostat and problems at high frequencies due to the resistance and capacitance of the fiber tip of the reference electrodes (Mansfeld, et al., 1988). The connection setup of the potentiostat and frequency response detector for the electrochemical impedance experiments as shown in *Fig. 15*.

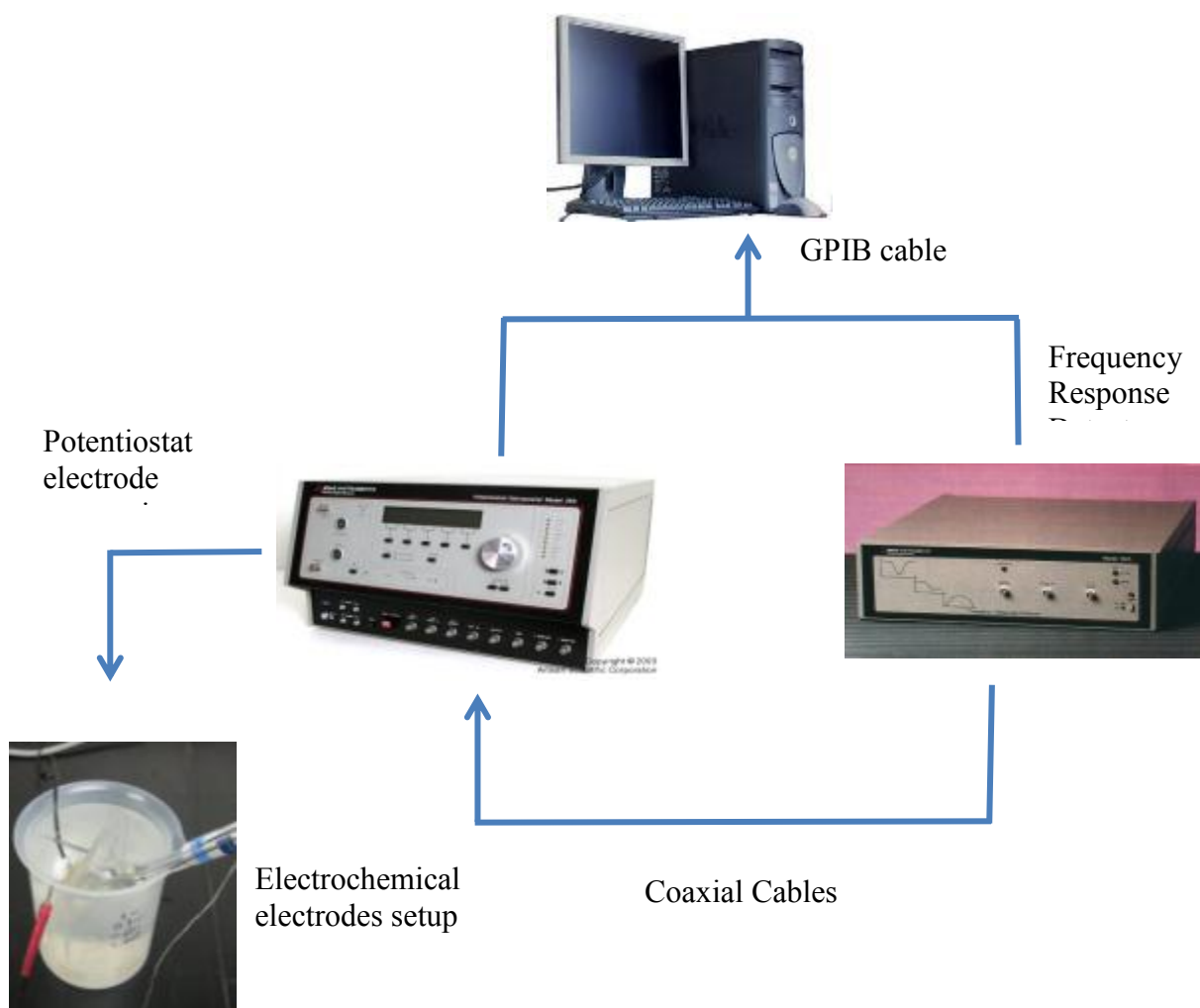


Figure 15 Potential and frequency response detector connection setup

### 3.7 Electrochemical noise experiments setup

The setup for the electrochemical noise experiments consisted of measuring current and voltage during different cycles of wet and dry in soil. The electrode coupon was composed of three galvanized steel electrodes working as the reference electrode, the counter electrode and the working electrode. Current was measured between the working electrode and the counter electrode; the potential was measured between the working electrode and the reference electrode, the third electrode.

The electrochemical noise setup is composed of two separate circuits, as shown in *Fig 16*. The circuit to acquire the voltage noise signals included a 10 M $\Omega$  connected to the working electrode to

dissipate probable parasitic capacitance. The voltage signal obtained between the working and reference electrodes is then connected to a buffer amplifier to simplify data acquisition. The circuit to acquire the current noise signals used the counter-electrode being grounded. The current signal then passed through an operational amplifier with a  $10\text{ k}\Omega$  resistance. The resultant signal finally passed through a buffer amplifier to improve the data acquisition.

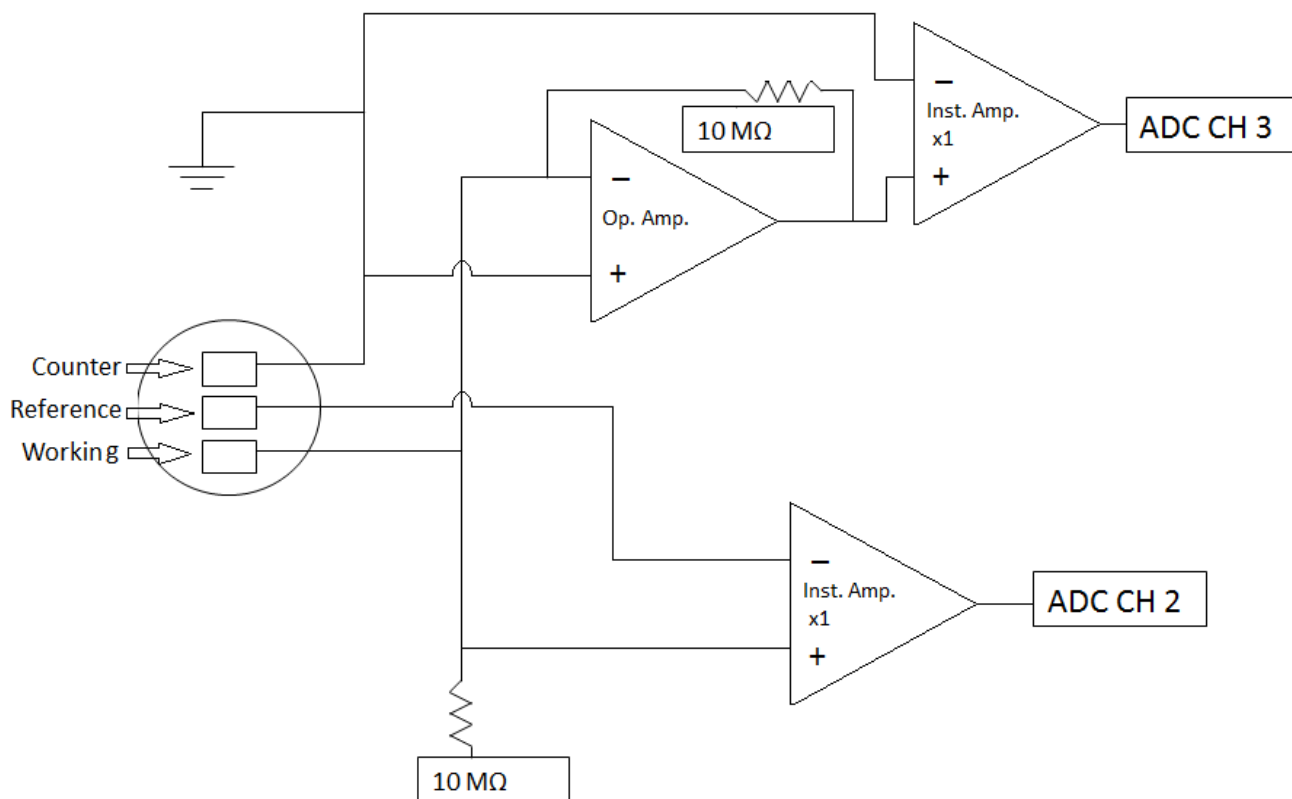


**Figure 16** Circuits used to acquire current and voltage electrochemical noise simultaneously.

## Chapter 4: Result and Discussion

### 4.1 Electrochemical Impedance Spectroscopy

Electrochemical impedance spectroscopy was performed for galvanized steel electrodes immersed in aqueous solutions containing 0.0001, 0.001, 0.01 and 0.1 M NaCl. To mimic the real time corrosion behavior of the galvanized steel in the soil, special attention was given to the results at the lowest molarity possible (0.0001 M NaCl), since it is the closest to the chloride content of the soil.

The low conductive solution effects the measured impedance, because the high frequency limit of the electrode impedance may no longer allow one to determine the electrolyte resistance (Chechirlian, et al., 1993). Therefore, the potential distribution inside the electrolyzing cell was measured using an external conductivity sensor (EC500). Since an accurate estimate for electrolyte resistance  $R_{s,est}$  is available, a modified Bode representation is possible as

$$|Z|_{adj} = \sqrt{(Z_r - R_{s,est})^2 + (Z_j)^2} \quad \phi_{adj} = \tan^{-1} \left( \frac{Z_j}{Z_r - R_{s,est}} \right)$$

for the reactive configuration, where  $Z_r$  is the real frequency of the Nyquist plot,  $Z_j$  is the imaginary frequency of the Nyquist plot and  $R_{s, est}$  is the solution resistance from the external sensor. The results are presented in *Fig. 17* for magnitude and phase angle, respectively. The slope of the corrected modulus yields valuable information concerning the existence of constant phase element behavior that is obscured in the traditional Bode presentation. At high frequencies, the corrected modulus is dominated by the contribution of the imaginary part of the impedance (Orazem, et al., 2008). Since the change is minimum is possible to continue using the polarization resistance from the actual Bode plot and Nyquist plots.

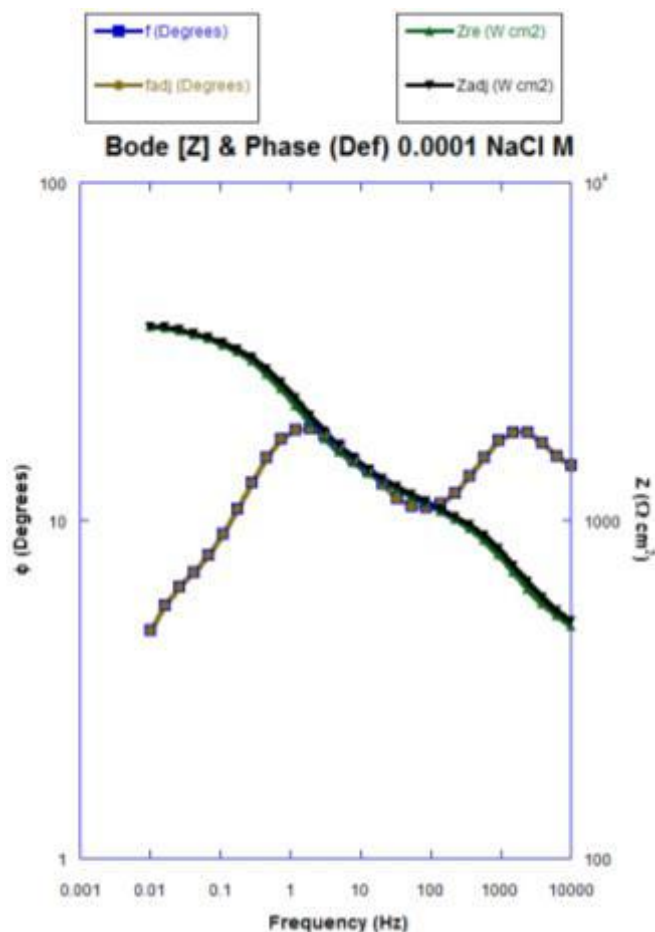


Figure 17 Adjusted Bode plot and Phase angle plot for 0.0001 M NaCl solution.

Bode and Nyquist plots were obtained for the NaCl contents ranging from 0.1 to 0.0001 M NaCl with a typical plot shown in *Fig. 18*. The Bode plots were obtained several times to verify the reproducibility of the results and averaged at each molarity to provide a more accurate result. The polarization resistance and solution resistance obtained from the Bode plots using Z-view, shows the difference in solution conductivity as well as the changes in corrosion rates as the chloride content increases as shown in *Fig. 19* and *Fig. 20*. The solution resistance varies linearly with molarity on a logarithmic plot, as shown in *Fig. 21*.

The resistivity with respect to the solution molarity was calculated by dividing the solution resistance acquired from EIS measurements by the spacing between the working electrode and the reference electrode. The resistivity obtained from the solution extracted from the real time corrosion



experiments in soil from Quarry F after running the wet/dry cycles for 24 months are shown in *Table 3*. The value of the resistivity from the solution obtained from the real-time corrosion experiments fall between the resistivity for 0.0001 and 0.001 M NaCl. But the resistivity is significantly closer to the resistivity at 0.0001 M NaCl.

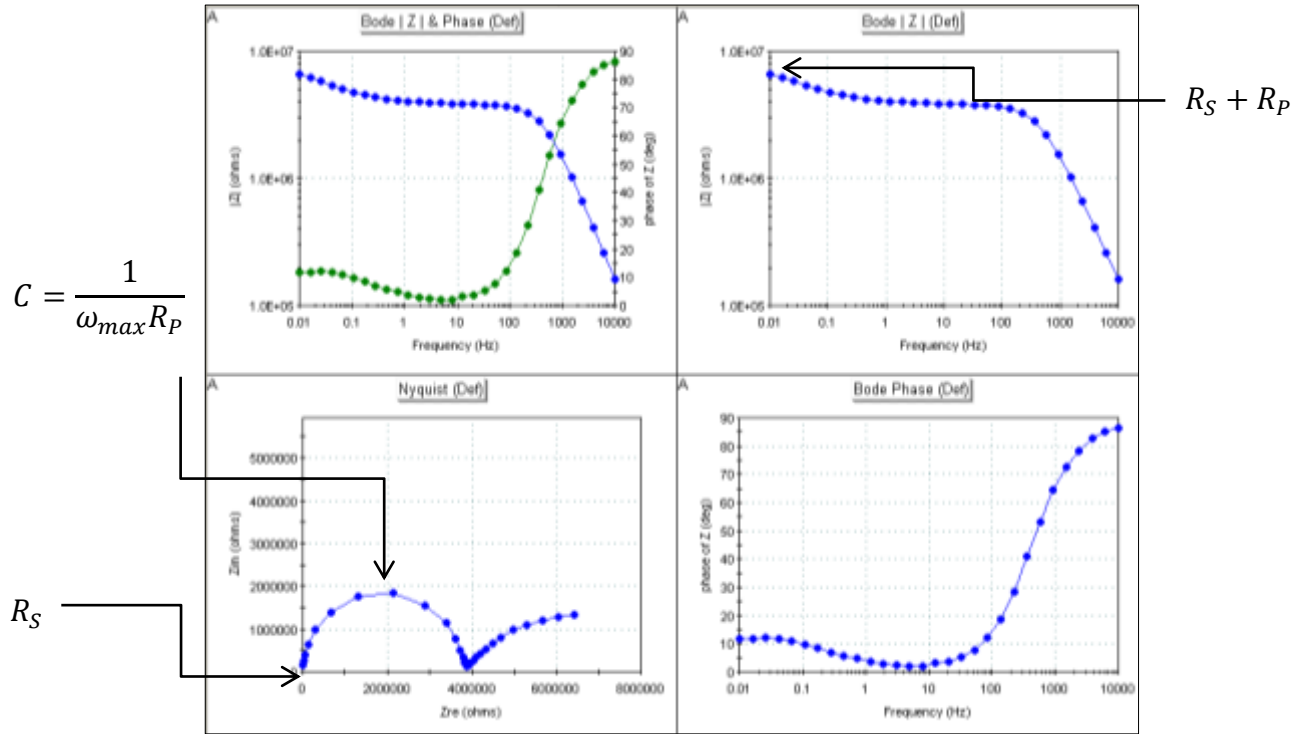


Figure 18 Bode and Nyquist plot of galvanized steel at 0.0001 M NaCl. Acquired with PowerSINE

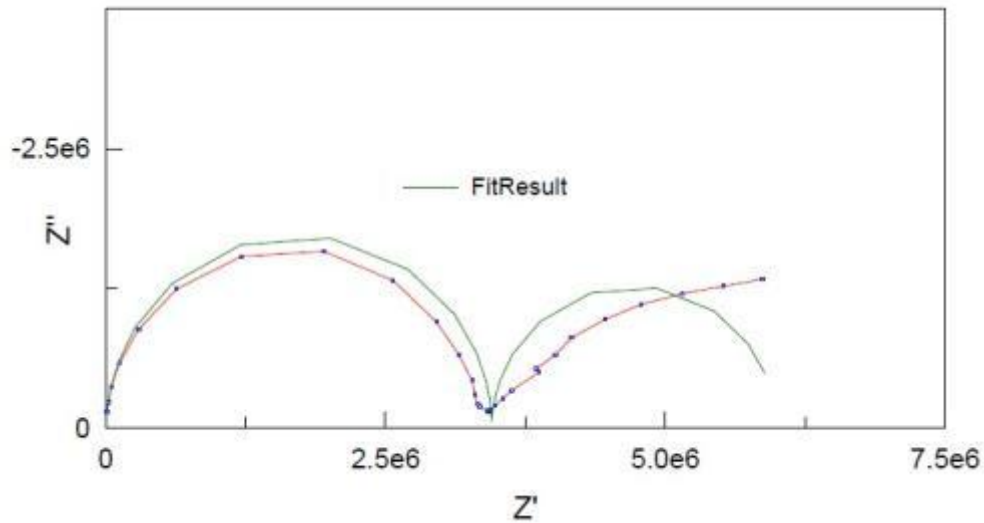


Figure 19 Nyquist plot of galvanized steel at 0.0001 M NaCl. Acquired with Zview

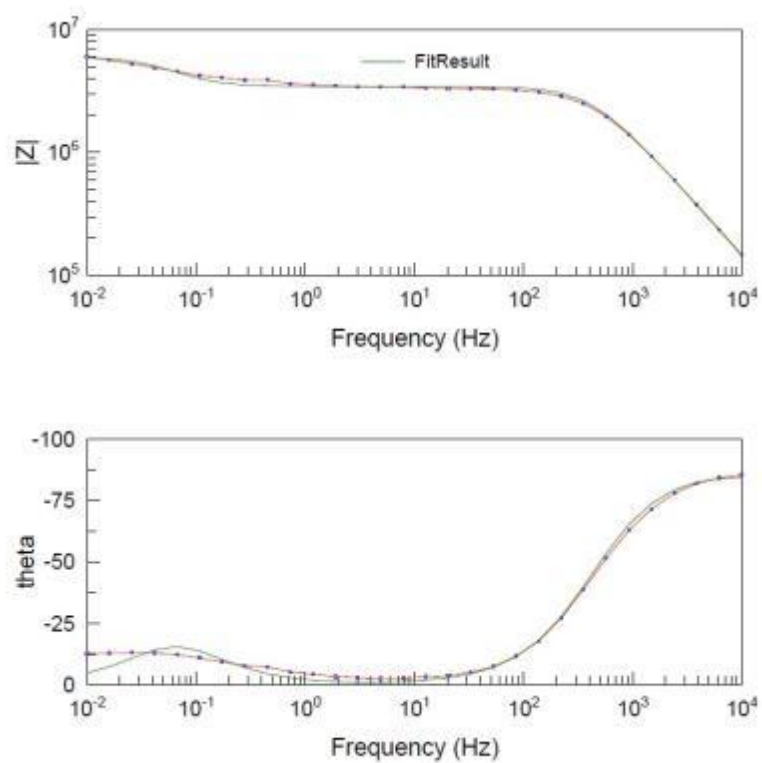


Figure 20 Bode and Phase angle plots of galvanized steel at 0.0001 M NaCl. Acquired with Zview

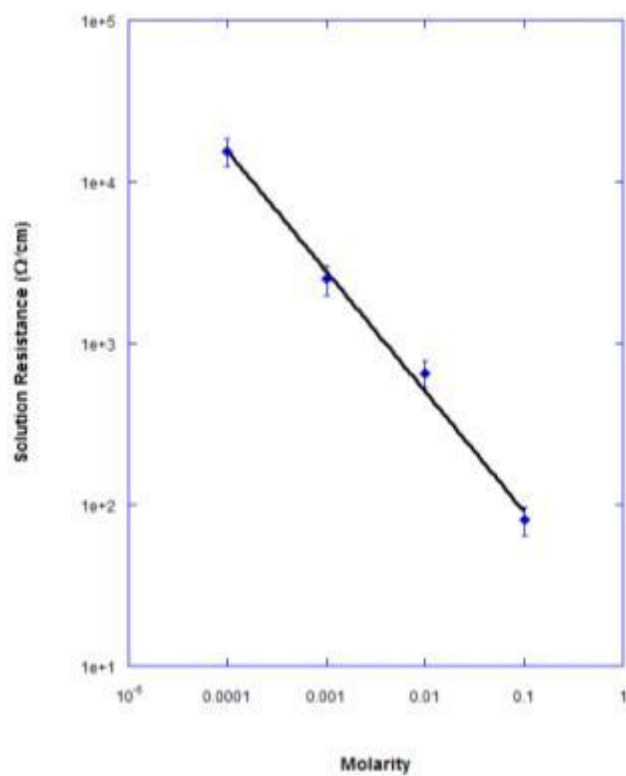


Figure 21. Solution resistance at different NaCl molarities. Acquired from PowerSINE

Table 3. Resistivities with respect to the solution molarity in addition to the resistivity of Quarry F soil solution after 24 months.

Molarity	Resistivity ( $\Omega/\text{cm}$ )
Quarry F Soil	2.10E+04
0.0001	1.43E+04
0.001	9.82E+03
0.01	2.21E+02
0.1	1.7E+02

A two time-constant, equivalent circuit was needed to simulate the electrochemical impedance data acquired for a 0.0001 M NaCl solution. The time constant was obtained through the Bode and Nyquist plots in *Fig. 22*. The equivalent circuit is composed of a solution resistance ( $R_s$ ), a polarization resistance ( $R_p$ ) and the double layer capacitance ( $C_{dl}$ ) with the corrosion values. Shown in table 4.

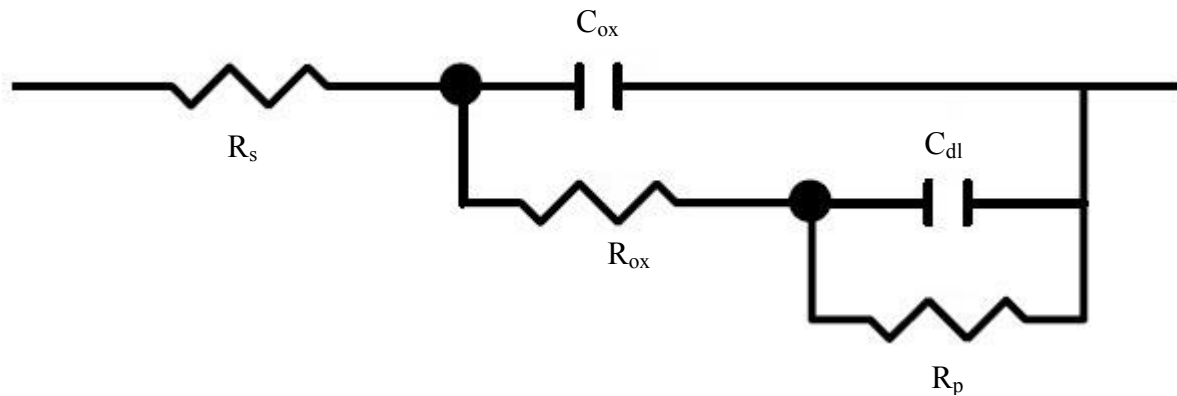


Figure 22. Equivalent circuit describing the two time-constant system of galvanized steel corroding in 0.0001 M NaCl solution.

Table 4. Values for equivalent circuit 0.0001 M NaCl solution

Element	Abbreviation	Value	Error	Error %
Solution resistance	$R_s$	8272	5224	63
Oxide capacitance	$C_{ox}$	1.10E-10	1.90E-12	1.72
Oxide resistance	$R_{ox}$	3.44E+06	38510	1.18
Double layer capacitance	$C_{dl}$	1.27E-06	1.13E-07	8.85
Polarization resistance	$R_p$	2.53E+06	1.48E+05	5.86

The polarization curve was obtained at four molarities to calculate the corrosion rate of galvanized steel, as well as the micrometers ( $\mu\text{m}$ ) and the mass loss during the corrosion of the material. Special attention was provided at the results at 0.0001 M NaCl because the concentration is closer to the actual chloride concentration of the soil in wet environment. The water used for the solution for the acquisition of the polarization curve is the same (deionized) water used for the real-time corrosion of the galvanized steel embedded in soil. The Tafel slopes were calculated at a low scan rate (0.1 mV/sec) to allow the half reactions to achieve steady-state the surface of the galvanized steel in the low molarity solution. The Tafel slopes were calculated as well as the corrosion potential. From the polarization curve, the Tafel slopes allowed for the calculation of the “k” constant.

$$k = \frac{b_a b_c}{2.303(b_a + b_c)}$$

The “k” constant along with the inverse of the polarization resistance allows for the calculation of the current density. With the current density of the system, the mass loss of the galvanized steel can be obtained. *Fig. 23* shows a typical polarization curve (e.g., 0.0001 M NaCl) with the Tafel slopes and the corrosion potential. The corrosion rate in terms of micrometers lost per year (MPY) was also calculated for the galvanized steel at the different NaCl molarities.

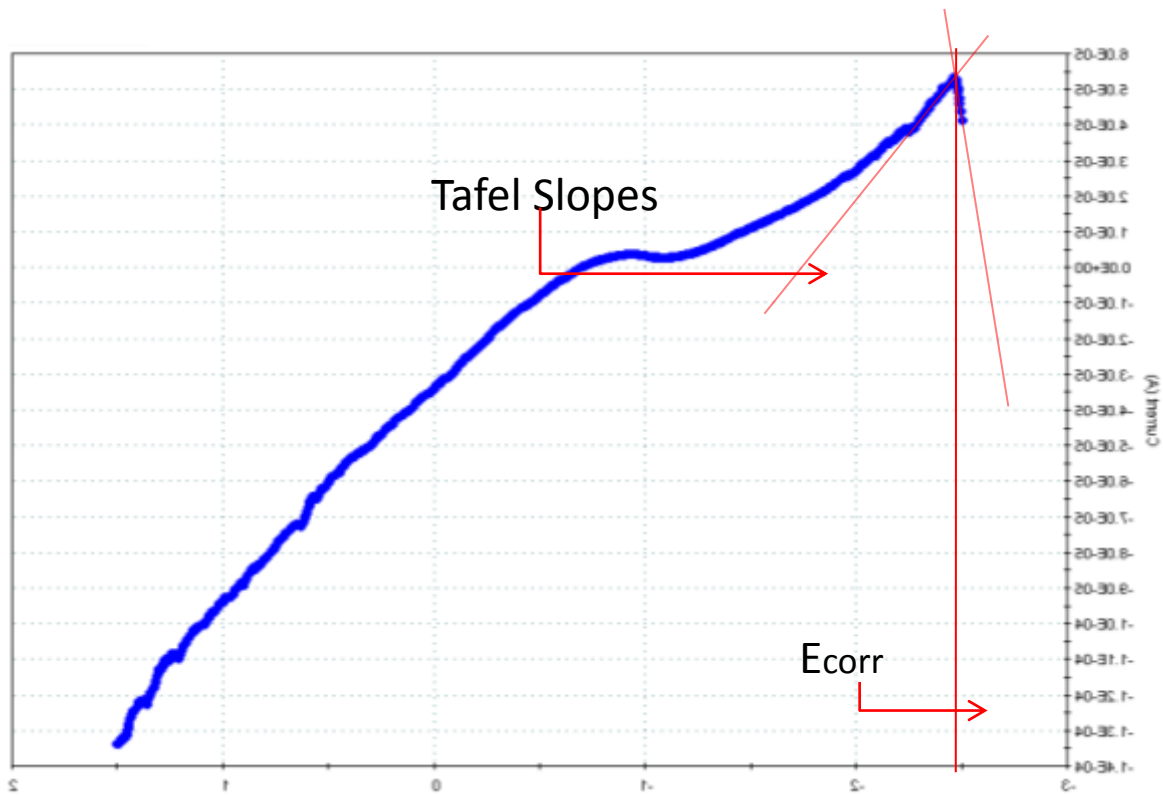


Figure 23 . Polarization curve of galvanized steel in 0.0001 M NaCl. Acquired with PowerCV (Castillo, 2011).

Table 5 shows the Tafel constants determined from the polarization curve for galvanized steel, as well as the calculated corrosion parameters at 0.0001 M NaCl solution and other NaCl molarities.

Table 5 Corrosion rate results for galvanized steel at different NaCl molarities.

Molarity	ba (V/decade)	bc (V/decade)	Rp (Ω)	k	icorr (amps/cm <sup>2</sup> )	ΔM (gr/cm <sup>2</sup> )	MPY	
							(mils/year)	(μm/yr)
0.1	0.555	1.3	1761	0.169	1.92E-04	1.87E-03	81.3105	2.07E+03
0.01	0.67	0.61	2516	0.139	1.10E-04	1.08E-03	46.7195	1.19E+03
0.001	0.065	0.395	8326	0.024	5.82E-06	5.68E-05	2.4679	6.27E+01
0.0001	1.44	0.024	2.54E+06	0.010	8.08E-09	7.89E-08	0.0034	8.70E-02

Fig. 24 shows the change in the current density as the NaCl molarity of the solution increases. Similarly Fig. 25 shows the change in μm lost per year in the coating. The changes from 0.0001 to 0.001 M NaCl are significantly small compared to the changes from 0.001 to 0.01 M NaCl or the changes from 0.01 to 0.1 M NaCl. These changes were expected since the increment in chloride concentration from 0.0001 to 0.001 M NaCl is very small (~0.0525 gr/L).

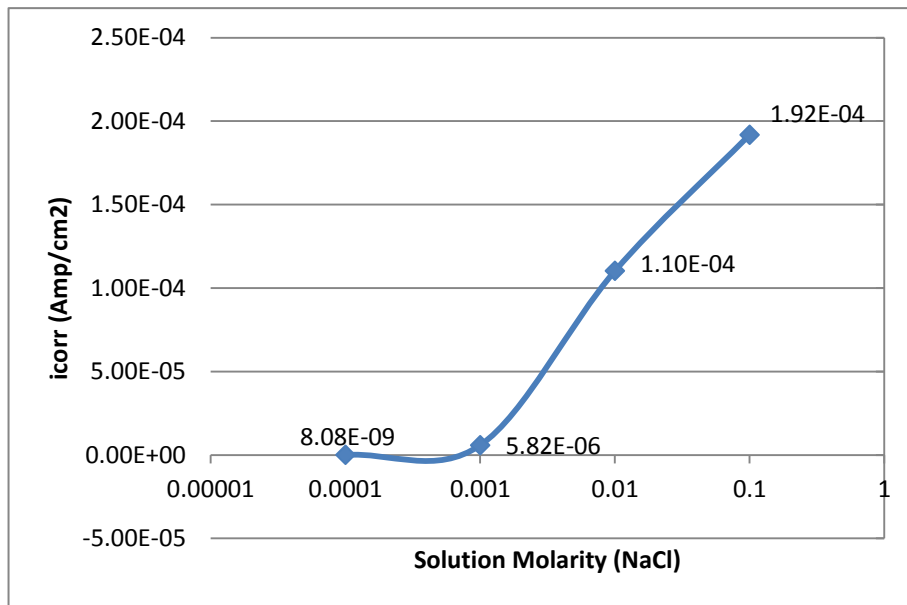


Figure 24. Change in current density as the NaCl molarity increases.

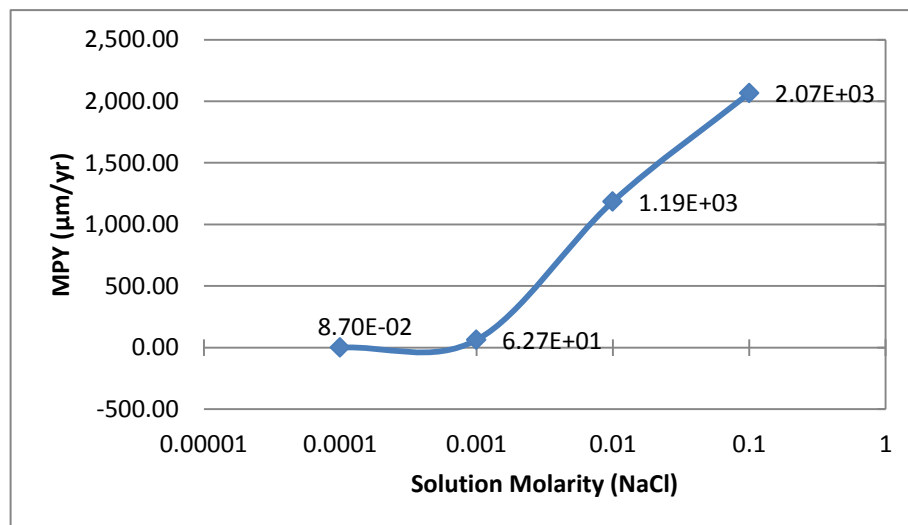


Figure 25 Corrosion rate in µm/yr as the NaCl molarity increases.

In Fig. 26 shows the corrosion rate with respect to conductivity calculated from previous data. As is expected the corrosion rate increased with increasing conductivity, which was correlated in a parallel study measuring the current from samples embedded in soil. The calculated corrosion rate from embedded samples decreased and stabilized after the first year, leaving a minimum corrosion rate on the surface of the galvanized steel.

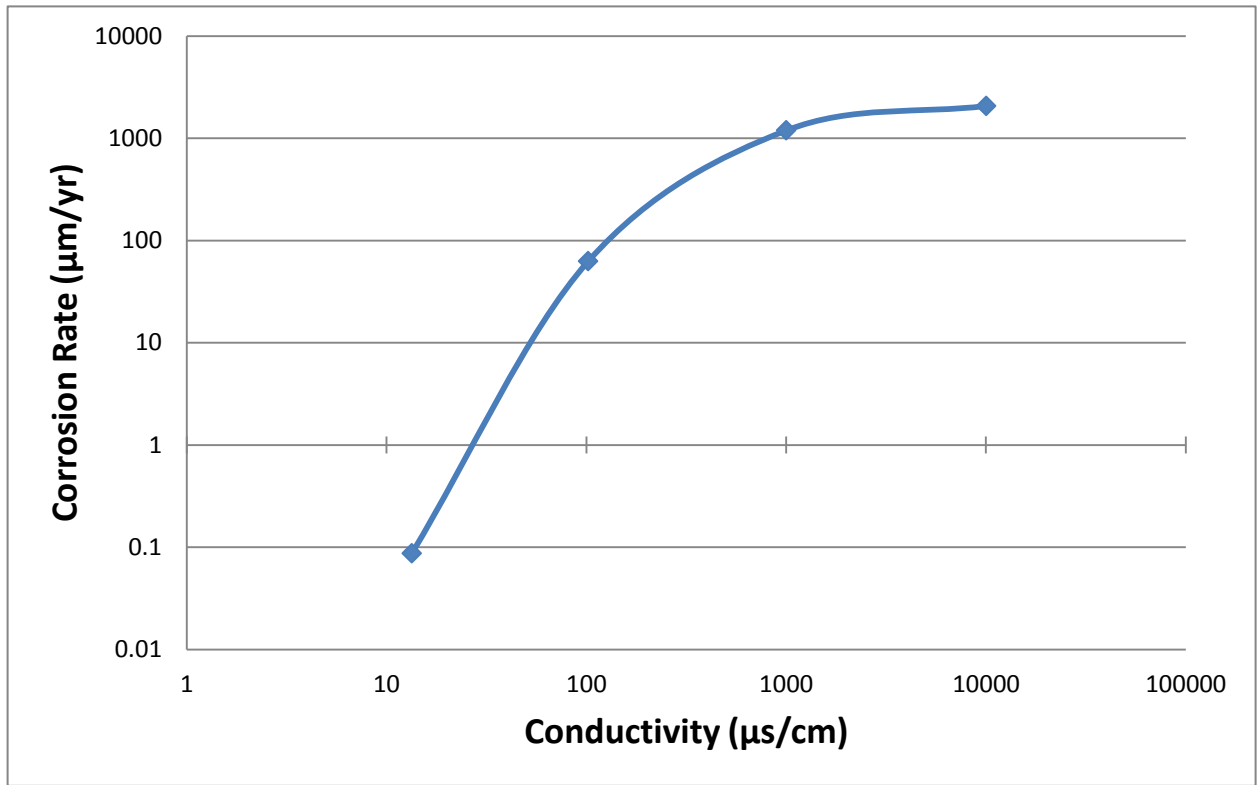


Figure 26 Conductivity vs. corrosion rate

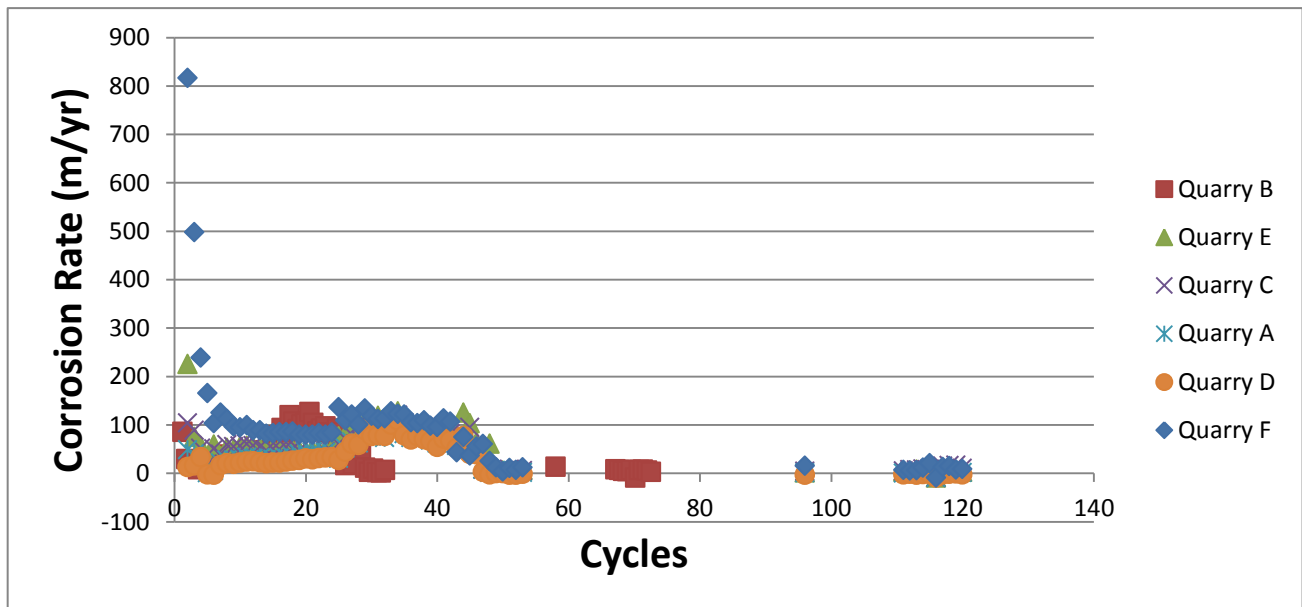


Figure 27 Corrosion rate vs time wet/dry

The calculated corrosion rate of zinc at 0.0001 and 0.001 M NaCl. 200 ppm Cl (0.0002 M Cl) 0.0001 NaCl ( $8.70\text{E-}02 \mu\text{m}$ ).





Specimens 1 and 3 were underground during the wet/dry cycle experiment for about 1 year and specimens 2 and 4 were exposed to soil with the similar wet/dry cycle for two years. The rate of acquisition of the current for electrochemical data was 40 minutes (2400 s) amounting to  $4(10)^{-4}$  Hz.

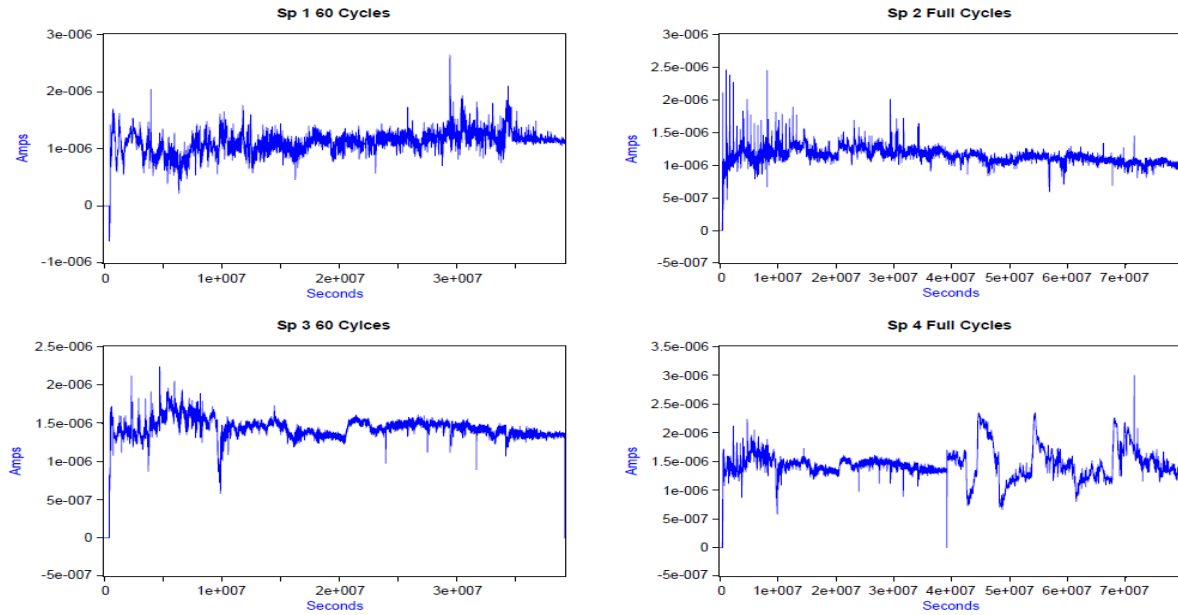


Figure 29 Current data corresponding to Quarry F

*Fig. 30* shows the PSD acquired from the fast Fourier transform (FFT) for a sample data of 1024 samples from the potential electrochemical data from Quarry F. *Fig. 31* shows the PSD acquired from the maximum entropy method (MEM) for the same data series. The PSD acquired from the MEM estimates the spectrum by calculating poles (order). An increasing order of the MEM smoothed the data the PSD from the FFT for the same data. The extrapolation of data to improve the frequency resolution is an advantage provided by the MEM method of the PSD-FFT calculation. *Fig. 32* shows the PSD acquired from both FFT and MEM, the graph shows that the MEM acquired PSD has a level high enough to simulate the FFT acquired PSD. The measured PSDs on white noise FFT and MEM are shown in the *Fig. 32*. The FFT technique does show a long PSD fluctuation compared to the MEM technique especially with increasing order. However, the MEM techniques shift the PSD ( $A^2/Hz$ ) to lower values

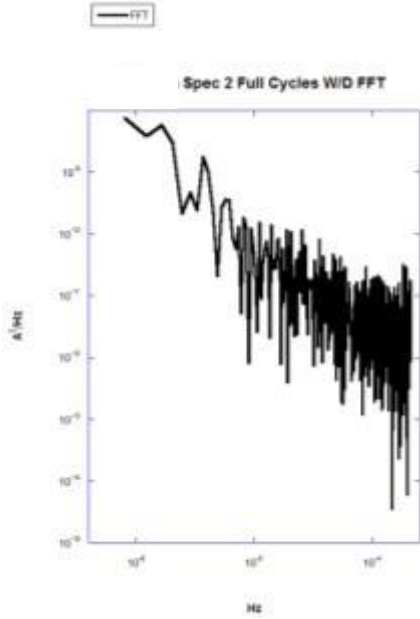


Figure 30 Current PSD acquired from FFT Quarry F sample

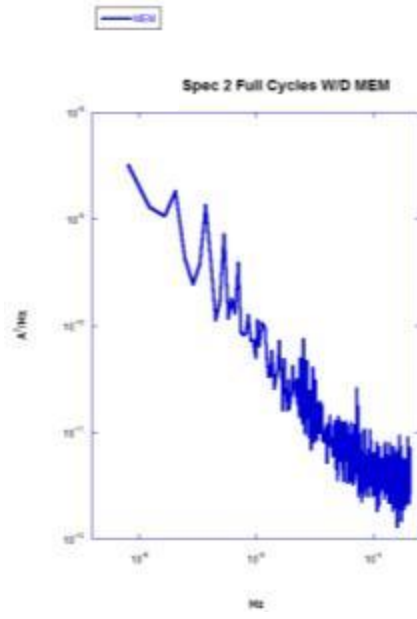


Figure 31 Current PSD acquired from MEM (order 1000) Quarry F Sample

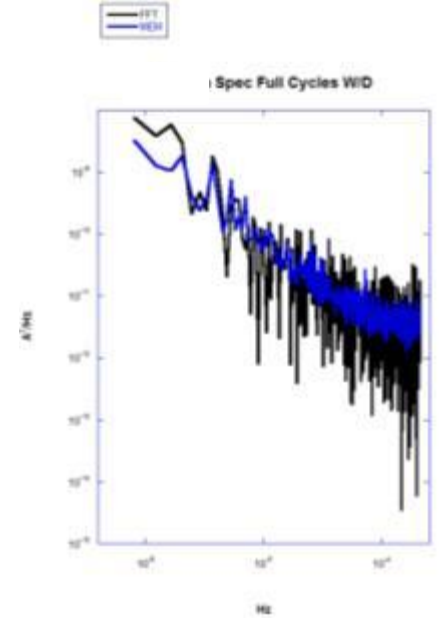


Figure 32 Current PSD Overlapping FFT and MEM Quarry F of Sample

The Nyquist sampling theorem provides a prescription for the nominal sampling interval required to avoid aliasing. It may be stated simply as follows: the sample frequency should be at least twice frequency contained in the signal Eq. 11

$$f_s \geq 2f_c \quad (11)$$

where  $f_s$  is the sample frequency and  $f_c$  is the highest frequency contained on the signal. After doing the calculation of  $f_s/f_c$ , the result was two, which indicate that the graphs are inside the parameter of Nyquist sampling theorem.

The samples were removed in two stages during the analysis of the experiment. The first set of samples were removed about the first year (60 cycles), this set of samples concluded with about sixteen thousand points of analysis data. The second stage of the experiment completed after two years (120 cycles), this part ended close to thirty-three thousand points of data. Every set of data point were divided on five parts to run PSD analysis and see the change of the plateau versus time as shown in *Fig. 33* and *Fig. 34*.

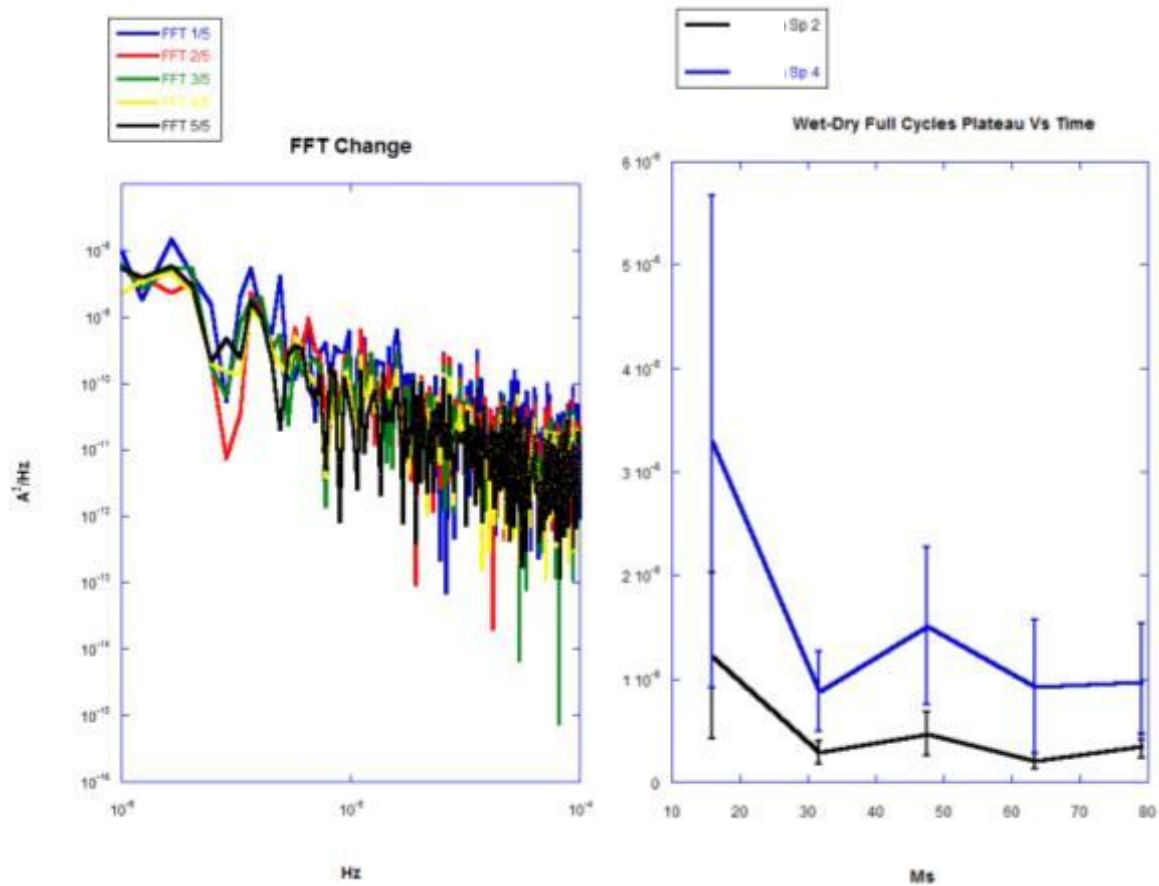


Figure 33 Variance of PSD acquired from FFT analysis for Quarry F W/D full cycles spec 2

Figure 34 Plateau vs. Time Quarry F full cycles W/D. Error bars indicate the std. error

### 4.3 Microstructures and corrosion products

The SEM image in *Fig. 35* shows the microstructure of the galvanized steel along with the thickness of the zinc coating and the thickness of the Fe-Zn intermetallic. The thickness of zinc layer approximated  $\sim 110 \mu\text{m}$  with. The Fe-Zn intermetallic having an average thickness of  $\sim 25 \mu\text{m}$ . A thin

layer of what was identified by Marder et al. as the gamma phase. And composed of both  $\Gamma$  phase ( $\text{Fe}_3\text{Zn}_{10}$ ) with an iron composition range of 23.5 –28.0 wt% and  $\Gamma_1$  phase ( $\text{Fe}_5\text{Zn}_{21}$ ) with an iron composition range of 17.0 -19.5 wt%, followed by the delta phase. The  $\delta$  ( $\text{FeZn}_{10}$ ) phase has a lower iron composition range than the  $\Gamma$  phase with 7.0 -11.5 wt%. Finally the zeta phase being the largest phase in the sample has an iron range composition of 5 -6 wt%, the outer phase ( $\eta$ ) being a zinc rich solid solution is about 25  $\mu\text{m}$  (Marder, 2000).

An SEM image of the zinc coating of a galvanized steel electrode after being corroded on wet cycle for the full process of experimentation is showed in *Fig. 36*. The microstructure shows that the galvanized coating underwent a general corrosion reducing the thickness of the coating uniformly in the surface about 10  $\mu\text{m}$ . After running a mapping analysis using an energy dispersive x-ray on SEM is possible to identify positioning and concentrations of chloride and underlying the zinc coating as shown in *Fig. 37*.

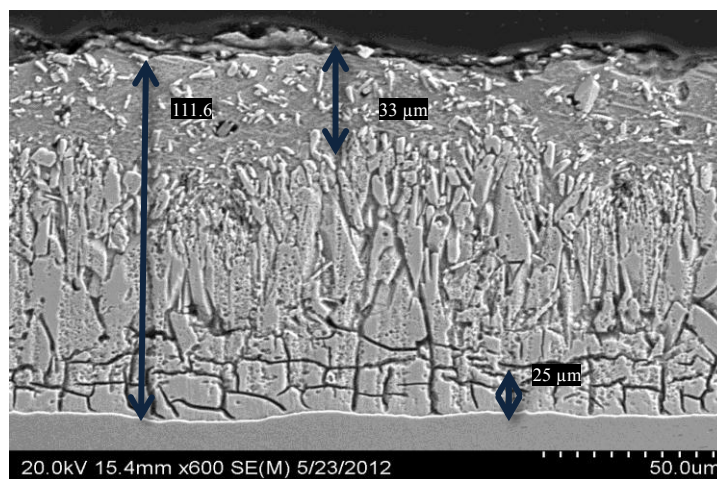


**Figure 35 SEM image of the galvanized steel microstructure.**

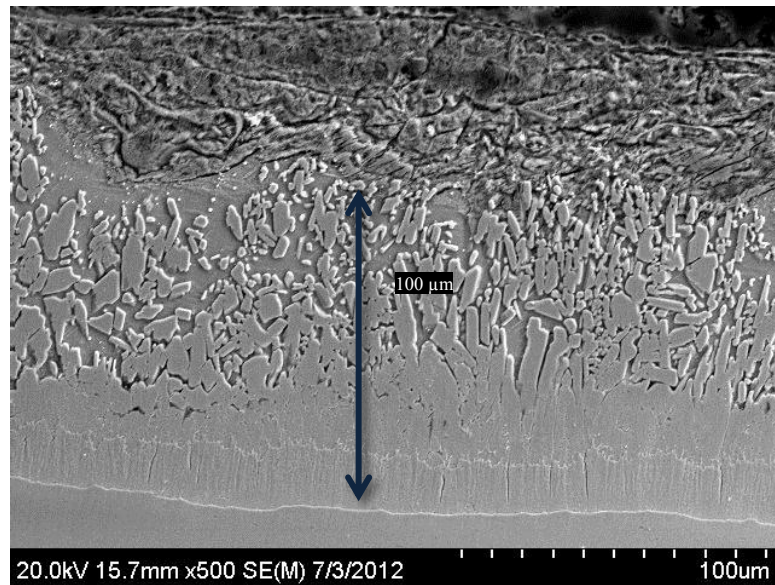


Figure 36 SEM image Bridgeport galvanized steel electrode in wet cycle after full process.

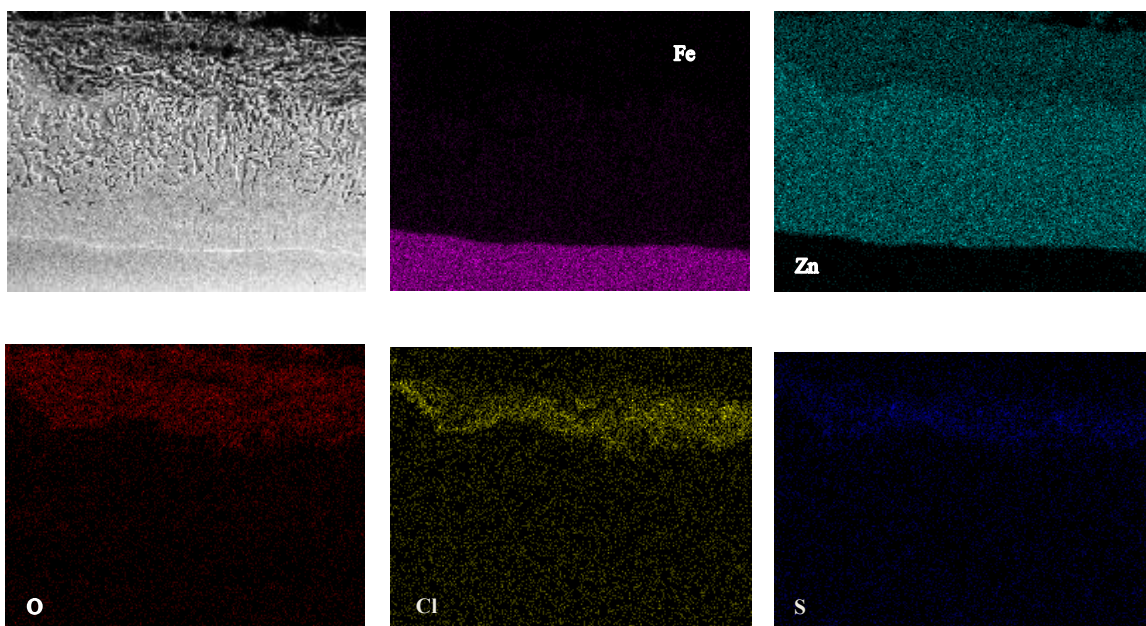


Figure 37 Bridgeport mapping of galvanized steel electrode

Fig. 38 shows a line scan analysis demonstrating the change of elements between zinc and iron across the metallic interface. At a distance range from 0  $\mu\text{m}$  to about 50  $\mu\text{m}$  the oxygen content increased significantly and iron content was almost zero. The chlorine and sulfur contents, representing



chloride and sulfate ion penetration increased about 25  $\mu\text{m}$  and decreased similarly with oxygen indicating that the zinc corrosion product of ZnO was porous on the surface. The change of intensity created at a distance of about 150  $\mu\text{m}$  represents when the zinc weight % decrease and the iron weight % increase. *Fig. 39* illustrates the scan line transpose in the picture where the elements were found.

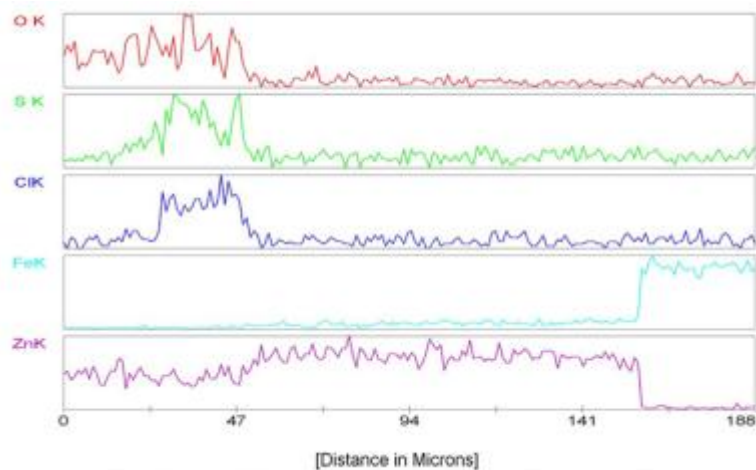


Figure 38 Bridgeport line scan of galvanized steel

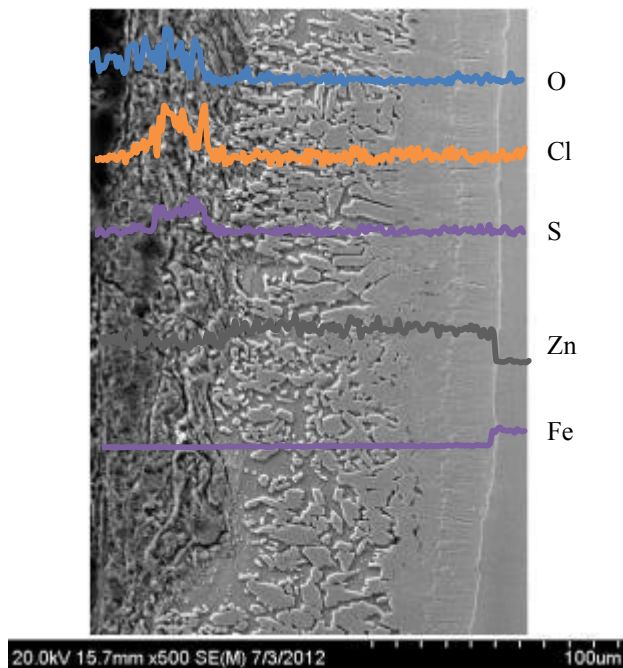


Figure 39 Bridgeport Galvanized steel scan line

SEM analyses along with mapping scan were performed on the extracted electrode from the electrochemical noise experiment performed with soil from Quarry F and Bridgeport. The electrode under-went wet/dry cycles for one year and two years. The microstructure of the zinc coating shows that corrosion products had started to produce in the surface. These corrosion products indicate that the galvanized steel is undergoing a passive corroding state. The mapping scan analyses show oxygen and chloride ions in the zeta phase, meaning that the underlying steel was not yet reached by the corrosion front. The SEM image illustrates that the thickness of the coating is significantly thicker than the average  $\sim 106\text{ }\mu\text{m}$  as shown in *Fig. 37*. Also shows the area that was analyzed in *Fig. 36* that the element analyzed is mainly composed of zinc and oxygen; these elements suggest that the principal component is ZnO. According to Yadav et al. the galvanized steel is in the first stage of corrosion mechanism in a chloride environment (Yadav, et al., 2004).

## Chapter 5: Conclusion

The corrosion of galvanized steel embedded to soil was the focus of the study primarily to determine the long-term behavior based on laboratory tests, as well as developing a sampling technique for monitoring corrosion in field-testing. The monitoring tests consisted of acquiring potential and current transients or electrochemical noise to determine the dissolution of the zinc coating, the intermetallic Fe-Zn layer and the underlying carbon steel. The electrochemical noise was then analyzed by examining the spectral densities and to the calculated corrosion rate.

In addition, electrochemical impedance spectroscopy (EIS) of the galvanized steel was analyzed to determine the effect of diluted chloride solutions. A double time constant of an equivalent circuit was used to simulate the corrosion behavior consisting of ZnO formation (i.e.,  $C_{ox}$  and  $R_{ox}$ ) and Zn dissolution ( $C_{dl}$  and  $R_p$ ). From the EIS, the corrosion rate was acquired when coupled with the potentiokinetic technique, or polarization scan. The corrosion rate for the galvanized steel reached 81 mils/yr at the high chloride content (i.e., 0.1 M NaCl) and 0.0034 mils/year for the low chloride content (i.e., 0.0001 M NaCl). In comparing the corrosion rates available from field bilogarithmic trends and the acquired laboratory studies, the laboratory corrosion rates of 0.0034 and 81  $\mu\text{m}/\text{yr}$  at 0.0001 and 0.1 M NaCl, respectively, corresponded to the field corrosion rate of 20  $\mu\text{m}/\text{yr}$  at 200 ppm Cl (approximating 0.0002 M Cl).

For the electrochemical noise analysis, the power spectrums were acquired for corrosion coupons embedded in soil. By using an fast Fourier transform and the maximum entropy method. The PSD-FFT followed the same decreasing trend depicted with the corrosion rate with increasing time.



## Bibliography

- Aal E. E. Abd Effect of Cl<sup>-</sup> anions on zinc passivity in borate solution [Journal] // Corrosion Science. - Zagazig : Elsevier Science Ltd., January 20, 2000. - pp. 1-16.
- Al-Mazeedi H. A. A. and Cottis R. A. A practical evaluation of electrochemical noise parameters as indicators of corrosion type [Journal] // Electrochemical Acta. - May 3, 2004. - Vol. 49. - pp. 2787-2793.
- Aramaki K. The inhibition effects of cation inhibitors on corrosion of zinc in aerated 0.5 M NaCl [Journal] // Corrosion Science. - 2001. - 43. - pp. 1573-1588.
- Aramaki Kunitsugu The inhibition effects of chromate-free, anion inhibitors on corrosion of zinc 0.5 M NaCl [Journal] // Corrosion Science. - 2001. - pp. 591-604.
- Bertocci U. [et al.] Analysis of Electrochemical Noise by Power Spectral Density Applied to Corrosion Studies [Journal] // Journal of Electrochemical Society . - 1998. - pp. 2780-2786.
- Castillo Carlos The electrochemical behavior of zinc [Report] : Thesis. - El Paso : The University of Texas at El Paso, 2011.
- Chechirlian Serge, Keddman Michel and Takenouti Hisasi Specific aspects of impedance measurements in low conductivity media [Journal] // ASTM International. - 1993. - pp. 23-36.
- Cottis R. A. and Turgoose S. Electrochemical noise measurements - a theoretical basis [Journal] // Materials Science Forum. - 1995. - pp. 663-672.
- Cottis R. A. Interpretation of Electrochemical Noise Data [Journal] // Corrosion. - 2001. - pp. 265-285.
- Dafydd H., Worsley D. A. and McMurray H. N. The kinetics and mechanism of cathodic oxygen reduction on zinc and zinc-aluminium alloy galvanized coatings [Journal] // Corrosion Science. - 2005. - pp. 3006-3018.
- El-Mahdy Gamal Ahmed, Nishikata Atsushi and Tsuru Tooru Electrochemical corrosion monitoring of galvanized steel under cyclic wet-dry conditions [Journal] // Corrosion Science. - 2000. - pp. 183-194.
- Fontana M. G. and Greene N. D. Corrosion Engineering [Book]. - NY : McGraw-Hill, 1967.

Gouda V. K., Khedr M. G. A. and Shams El Din A. M. Role of anions in the corrosion and corrosion-inhibition of zinc in aqueous solution [Journal] // Corrosion Science. - 1967. - pp. 221-230.

Hamlaoui Y, Pedraza F. and Tifouti L. Corrosion monitoring of galvanised coatings through electrochemical impedance spectroscopy [Journal] // Corrosion Science. - 2008. - pp. 1558-1566.

Horstmann D. Reaction between zinc and iron [Journal] // Zinc development association. - 1978.

Ishikawa T. [et al.] Formation of magnetite in the presence of ferric oxhydroxides [Journal] // Corrosion Science. - 1998. - pp. 1239-1251.

Ishikawa T. [et al.] Influence of anions on the formation of  $\beta$ -FeOOH rusts [Journal] // Corrosion Science. - 2005. - pp. 2510-2520.

Jones Denny A. Principles and Prevention of Corrosion [Book]. - NY : Macmillan Publishing Company, 1992.

Kelly R. G. [et al.] Electrochemical techniques in corrosion science and engineering [Book]. - Broken Sound Parkway : CRC Press, 2003.

Kubachewski O. and Massalski T. Binary alloy phase diagrams [Journal] // ASM. - 1986. - p. 1128.

Langill and Thomas J. American Galvanizers Association [Online]. - August 17, 2005. - February 8, 2012. - <http://www.galvanizeit.org/>.

Li C. [et al.] EIS monitoring study of atmospheric corrosion under variable relative humidity [Journal]. - Sheyang : Corrosion Science, 2010. - 52. - pp. 3677-3688.

Ma Y. and Wang F. Corrosion of low carbon steel in atmospheric environments of different chloride content [Journal] // Corrosion Science . - 2009. - pp. 997-1006.

Mansfeld F and Xiao H Electrochemical noise analysis of iron exposed to NaCl solution of different corrosivity [Journal] // J Electrochemical Soc. - 1993. - pp. 2205-2209.

Mansfeld F Electrochemical Impedance Spectroscopy as a new tool for investigating methods of corrosion protection [Journal] // Electrochimica Acta. - 1990. - pp. 1533-1544.

Mansfeld F. [et al.] Minimization of high-frequency phase shift in impedance measurements [Journal] // Journal of Electrochemical Society. - 1988. - pp. 906-908.

Mansfeld F. and Lee C. C. The frequency dependence of the noise resistance for polymer-coated metals [Journal] // Journal of Electrochemical Society. - 1997. - pp. 2068-2071.

Mansfeld Florian Corrosion Mechanisms [Book]. - NY : Marcel Dekker, Inc., 1987.

Marcus P. and Mansfeld F. Corrosion Science and Engineering [Book]. - NY : Taylor & Francis, 2006.

Marder A. R. The metallurgy of zinc coated steel [Journal] // Progress in materials science. - 2000. - pp. 191-271.

Morcillo M. [et al.] Atmospheric corrosion of mild steel [Journal] // Revista de metalurgia. - 2011. - pp. 426-444.

Nishikata A., Ichihara Y. and Tsuru T. An application of electrochemical impedance spectroscopy to atmospheric corrosion study [Journal] // Corrosion Science. - 1995. - 6 : Vol. 37. - pp. 897-911.

Orazem Mark E and Tribollet Bernard Electrochemical Impidance Spectroscopy [Book] / ed. Wiley A John. - Pennington : The Electrochemical Society Series, 2008.

Perez Nestor Electrochemistry and corrosion science [Book]. - Norwell : Kluwer Academic Publishers, 2004.

Porter Frank C. Corrosion Resistance of zinc and zinc alloy [Book]. - NY : Marcel Dekker, 1994.

Refait P. and Genin J.-M.R. The mechanisms of oxidation of ferrous hydroxychloride  $\beta\text{-Fe}_2(\text{OH})_3\text{Cl}$  in aqueous solution: the formation of akaganeite Vs goethite [Journal] // Corrosion Science. - 1997. - pp. 539-553.

Remazellines C. and Refait Ph. On the fromation of B-FeOOH (akaganeite) in chloride-containing environments [Journal] // Corrosion Science. - 2007. - pp. 844-857.

Schweitzer P. A. Fundamentals of metallic corrosion [Book]. - NY : CCR Press, 2007.

Schweitzer Philip A. Fundamentals of corrosion Mechanisms, causes, and preventative methods

[Book]. - NY : Taylor and Francis Group, 2010.

Shreir L. L., PhD, Jarman R. A., PhD and Burstein G. T.. PhD Corrosion [Book]. - Oxford : Hartnolls, Bodmin, 1994.

Tanaka Hidekazu [et al.] Role of zinc on the formation, morphology, and adsorption characteristics of  $\beta$ -FeOOH rusts [Journal] // Corrosion Science. - 2010. - pp. 2973-2978.

Walter G. W. Corrosion rates of zinc, zinc coatings and steel in aerated slightly acidic chloride solutions calculated from low polarization data [Journal] // Corrosion Science. - 1976. - pp. 573-586.

Walter G. W. Critical Analysis of Some Electrochemical Techniques Including Polarization Resistance, for the Study of Zinc Coating Performance in Near Neutral Chloride Solutions. [Journal] // Corrosion Science. - 1975. - pp. 47-56.

Yadav A P, Nishikata A and Tsuru T Electrochemical impedance study on galvanized steel corrosion under cyclic wet-dry condition-influence of time of wetness [Journal] // Corrosion Science. - 2004. - pp. 169-181.

Yadav A. P. [et al.] Effect of Fe-Zn alloy layer on the corrosion resistance of galvanized steel in chloride containing environment [Journal] // Corrosion Science. - 2007. - pp. 3716-3731.

Yadav Amar Prasad, Nishikata Atsushi and Tsuru Tooru Degradation mechanism of galvanized steel in wet-dry cyclic environment containing chloride ions [Journal] // Corrosion Science . - 2004. - pp. 361-376.

Yavad A. P. [et al.] Surface potential distribution over a zinc/steel galvanic couple corroding under thin layer of electrolyte [Journal] // Electrochemical Acta. - 2007. - pp. 3121-3129.

Zhang X. G. and Valeriote E. M. Galvanic protection of steel and galvanic corrosion on zinc under thin layer electrolytes [Journal] // Corrosion Science. - 1993. - pp. 1957-1972.

## Appendix

### Electrochemical impedance spectroscopy graphs

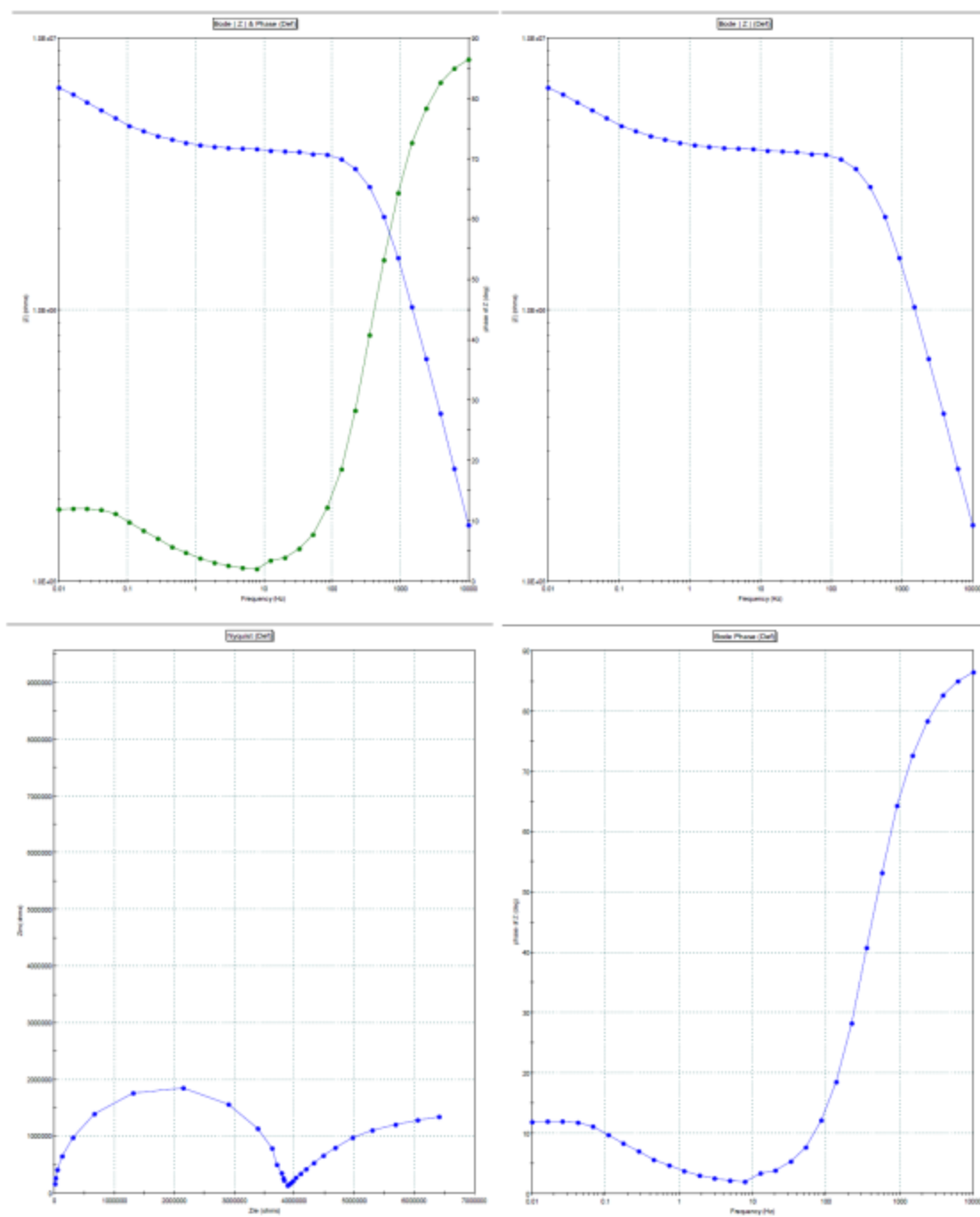


Figure 40. Bode and Nyquist plots for galvanized steel at 0.0001 M NaCl solution.

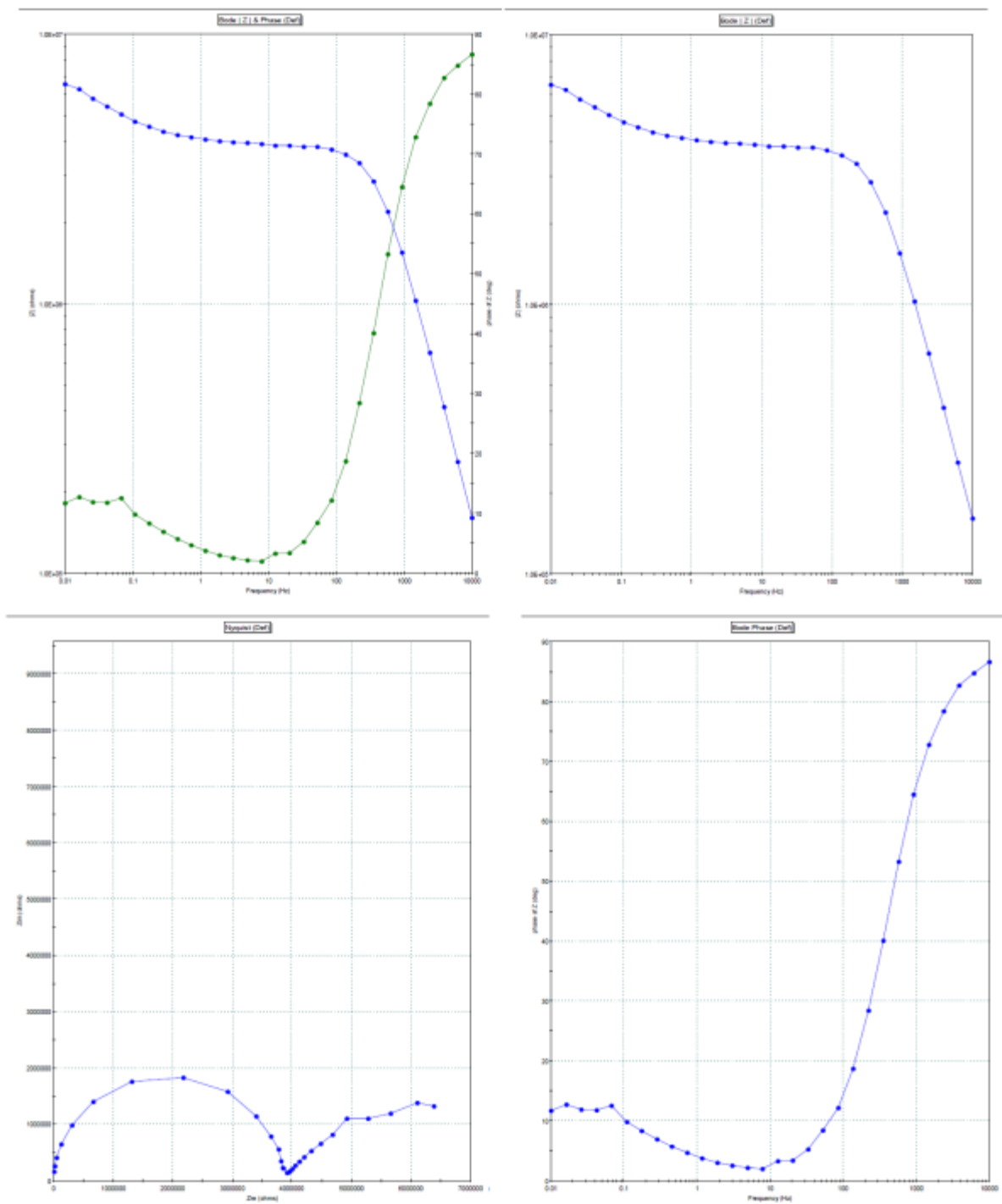


Figure 41. Bode and Nyquist plots for galvanized steel at 0.0001 M NaCl solution.

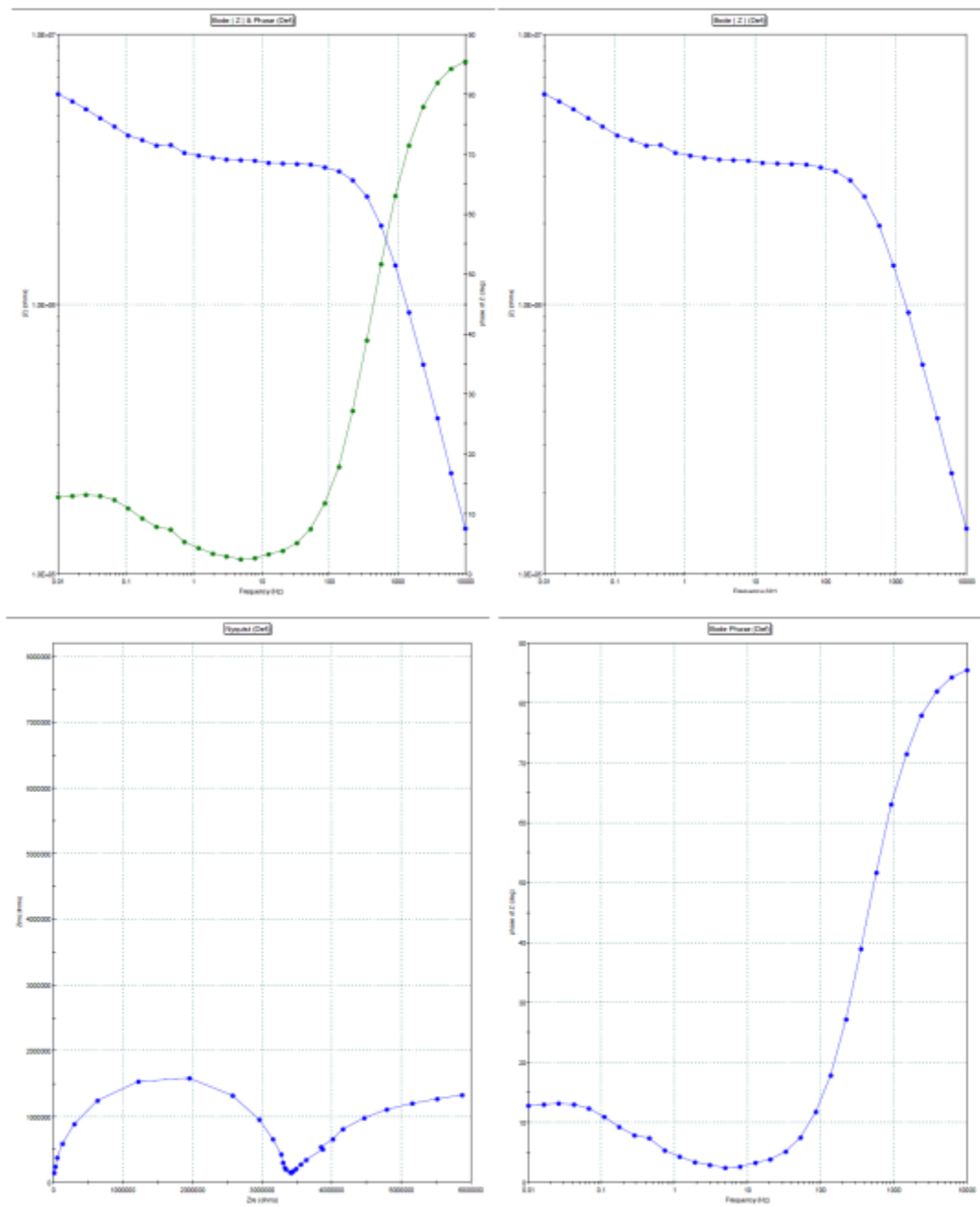


Figure 42 Bode and Nyquist plots for galvanized steel at 0.0001 M NaCl solution.

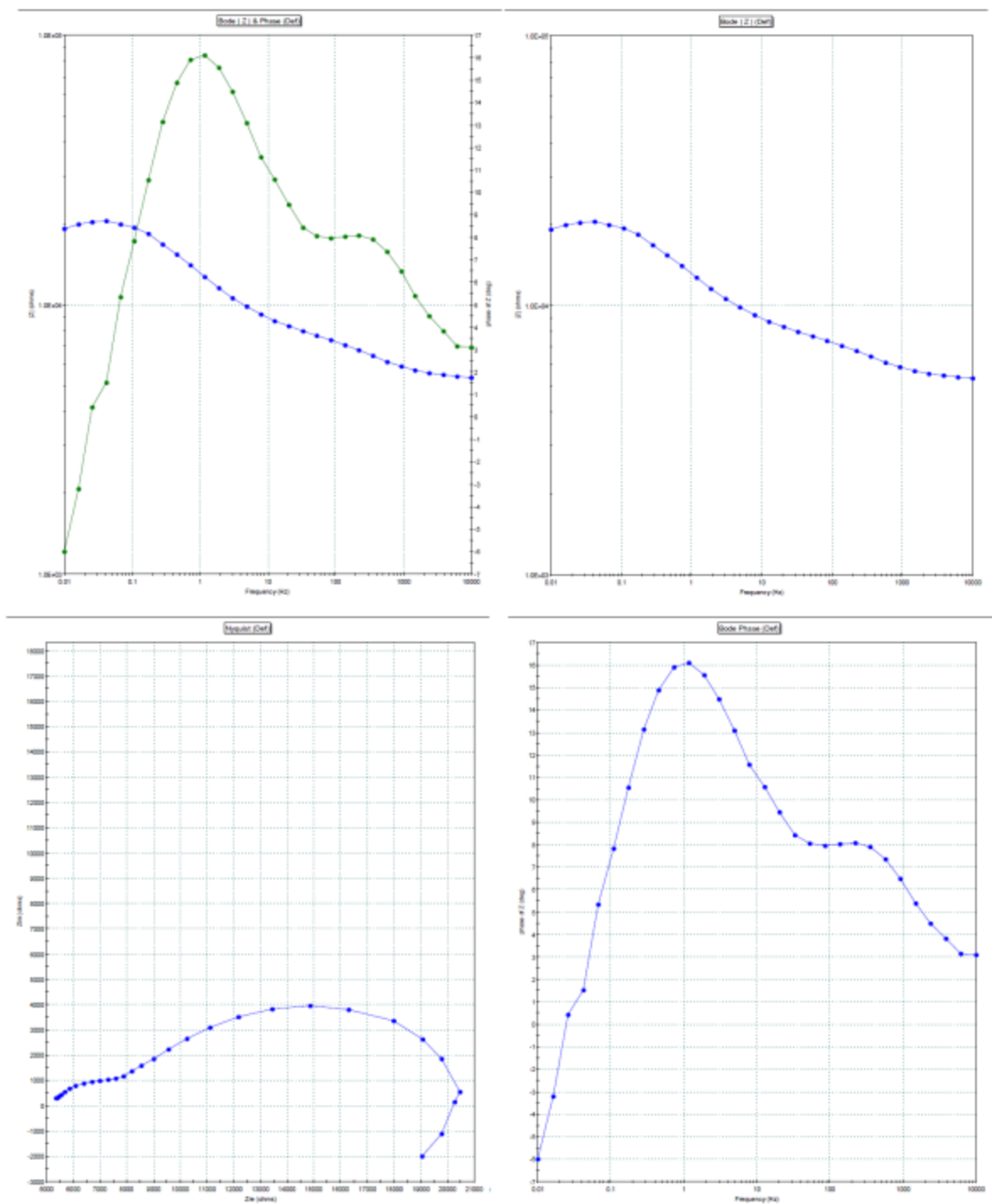


Figure 43 Bode and Nyquist plots for galvanized steel at 0.001 M NaCl solution.



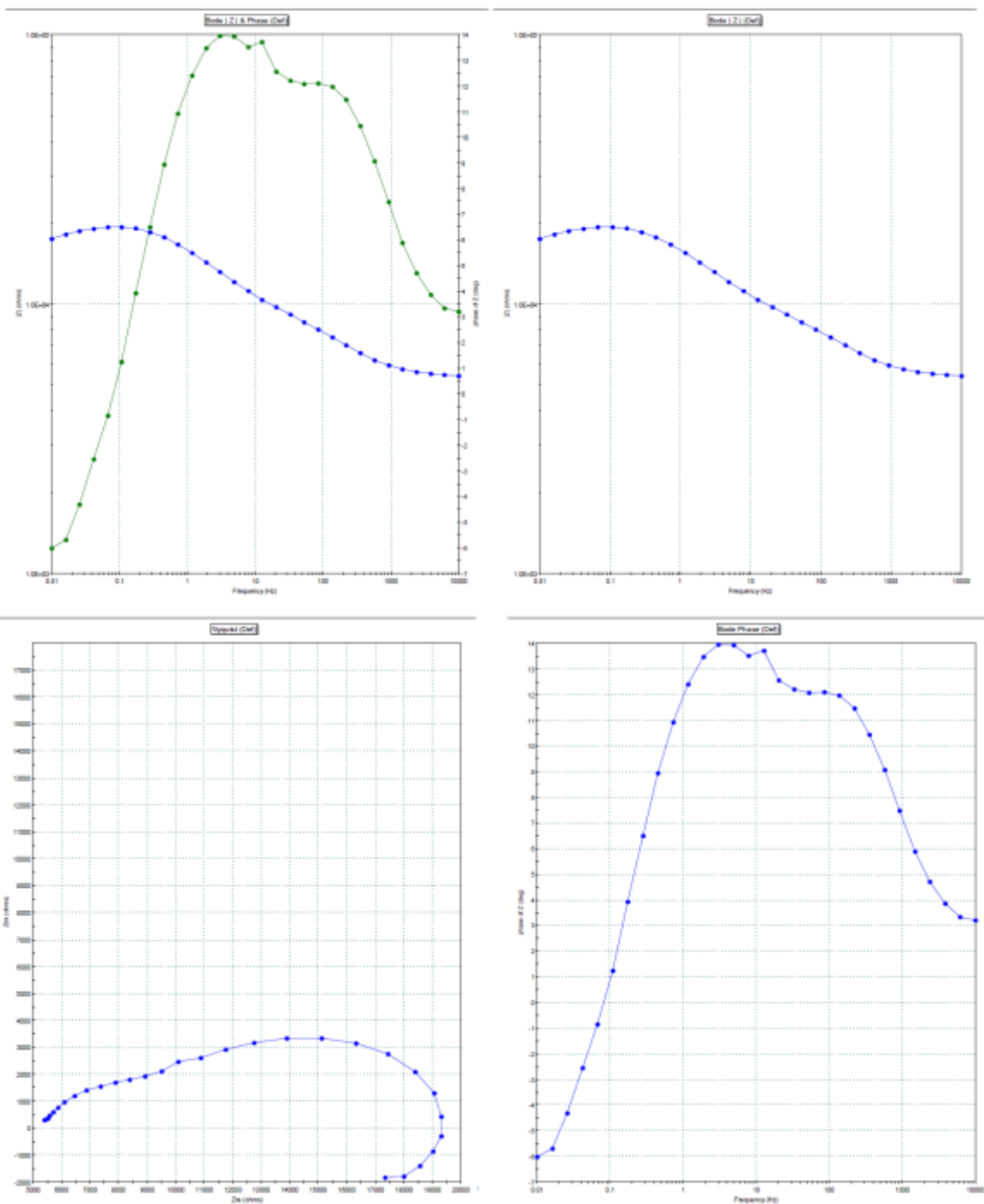


Figure 44. Bode and Nyquist plots for galvanized steel at 0.001 M NaCl solution.

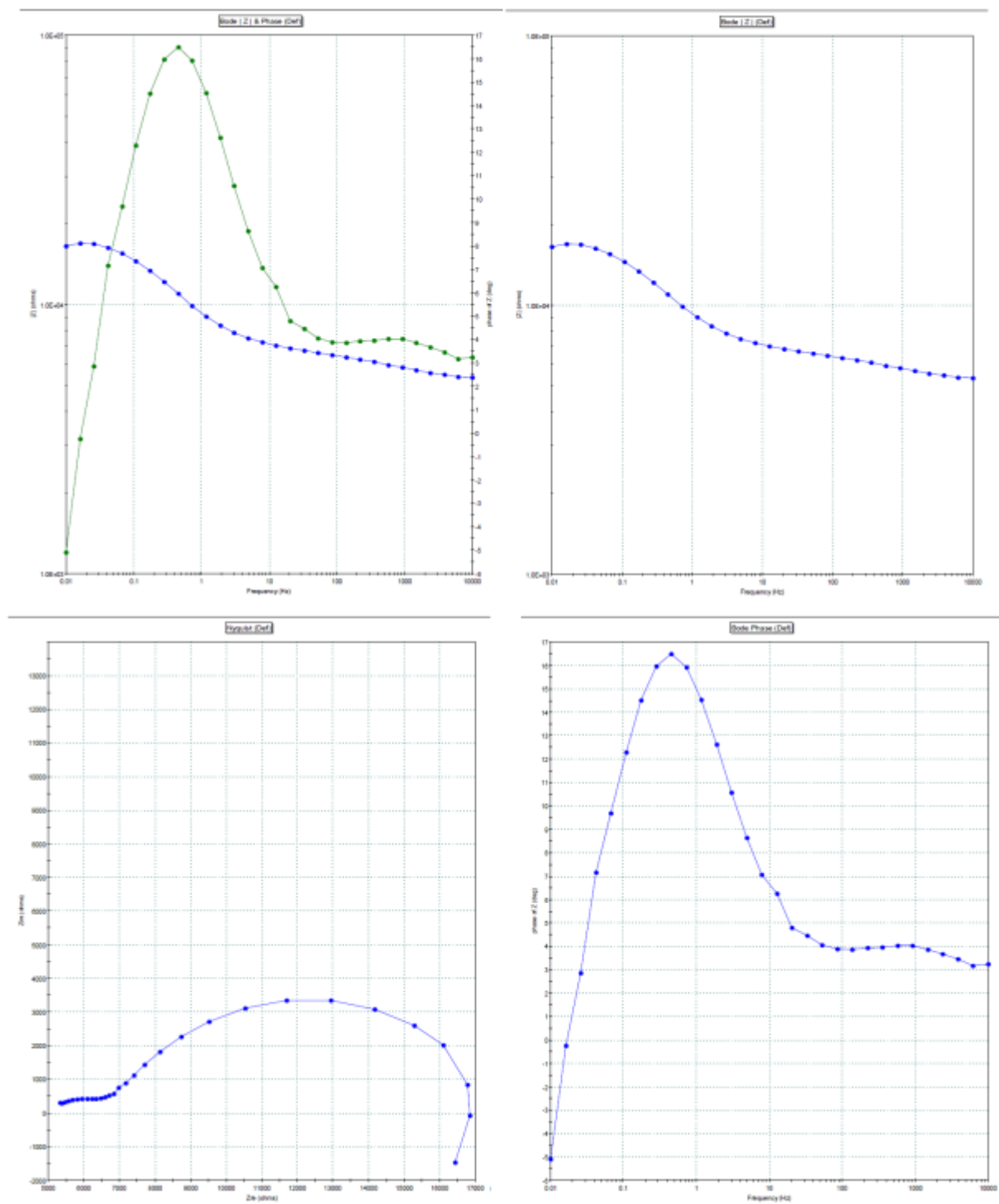


Figure 45. Bode and Nyquist plots for galvanized steel at 0.001 M NaCl solution.

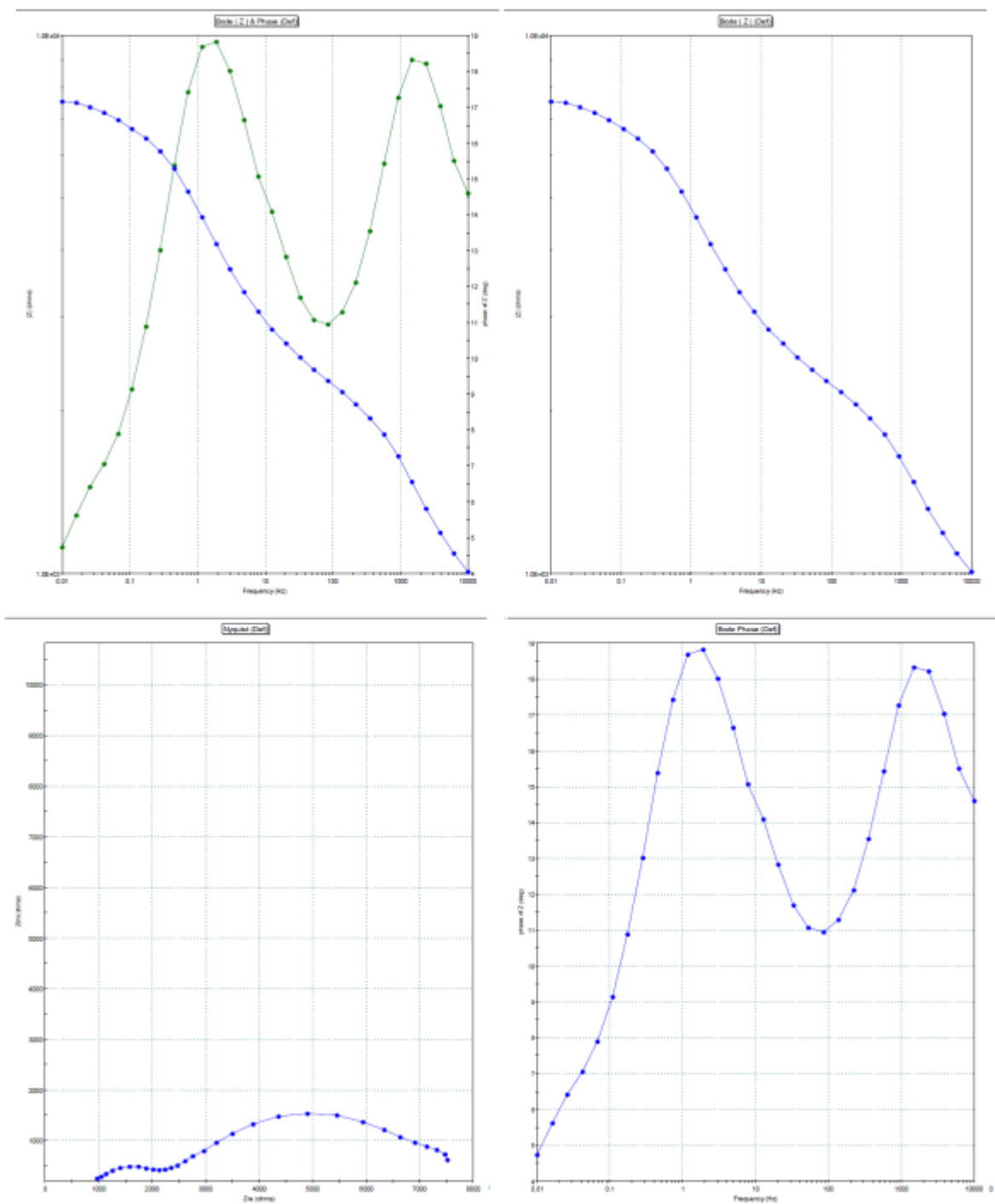


Figure 46. Bode and Nyquist plots for galvanized steel at 0.01 M NaCl solution.

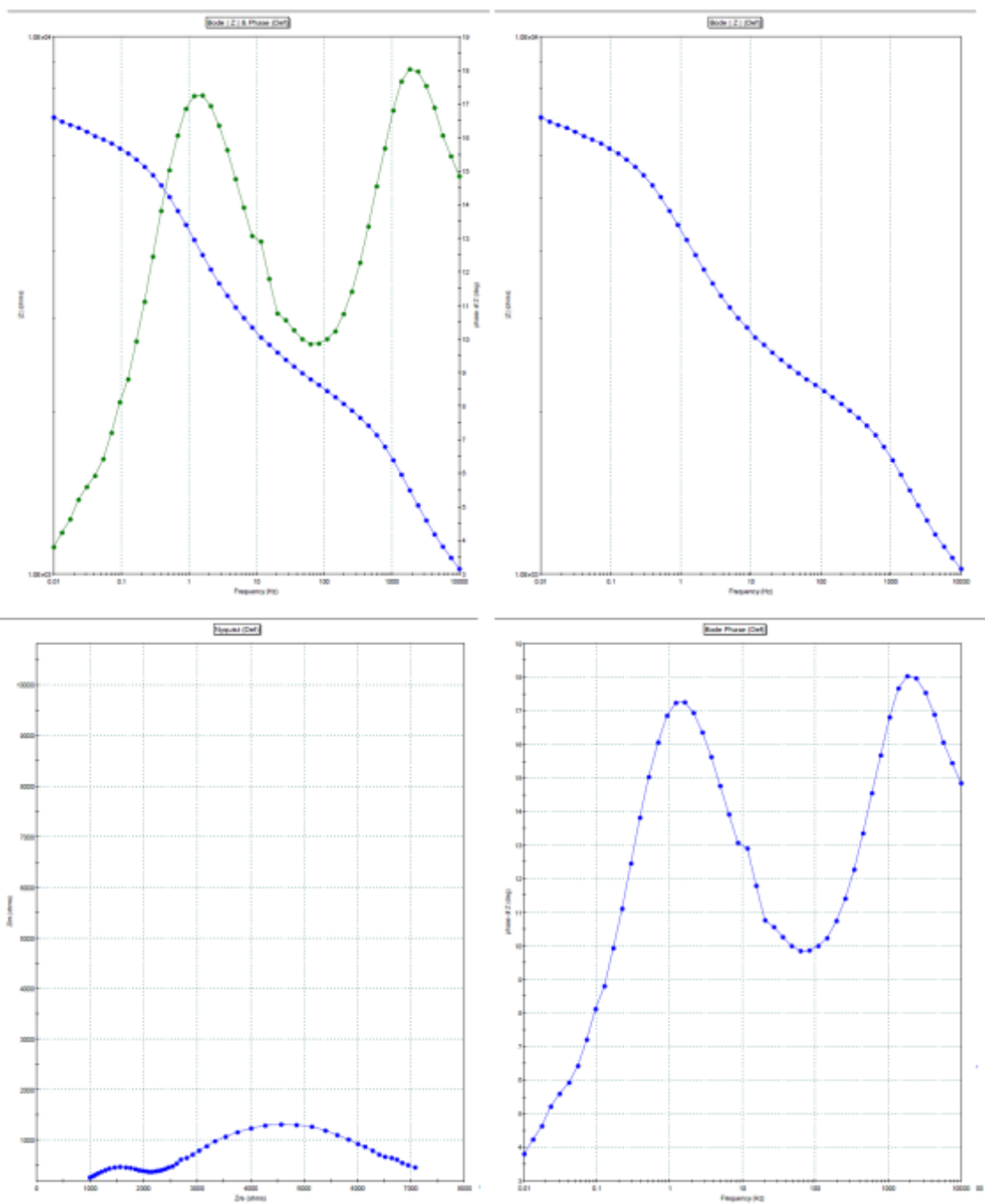


Figure 47. Bode and Nyquist plots for galvanized steel at 0.01 M NaCl solution.

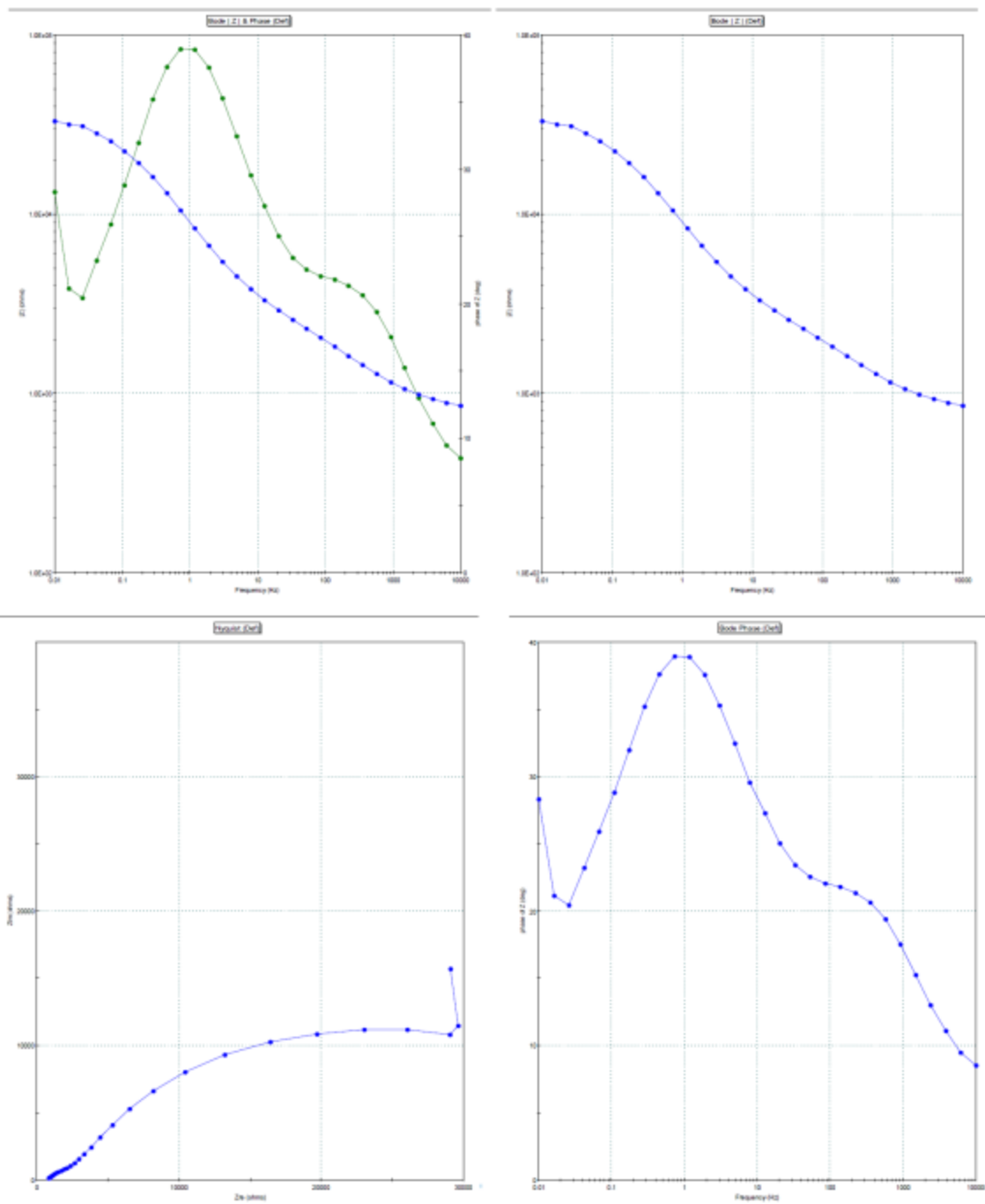


Figure 48. Bode and Nyquist plots for galvanized steel at 0.01 M NaCl solution.

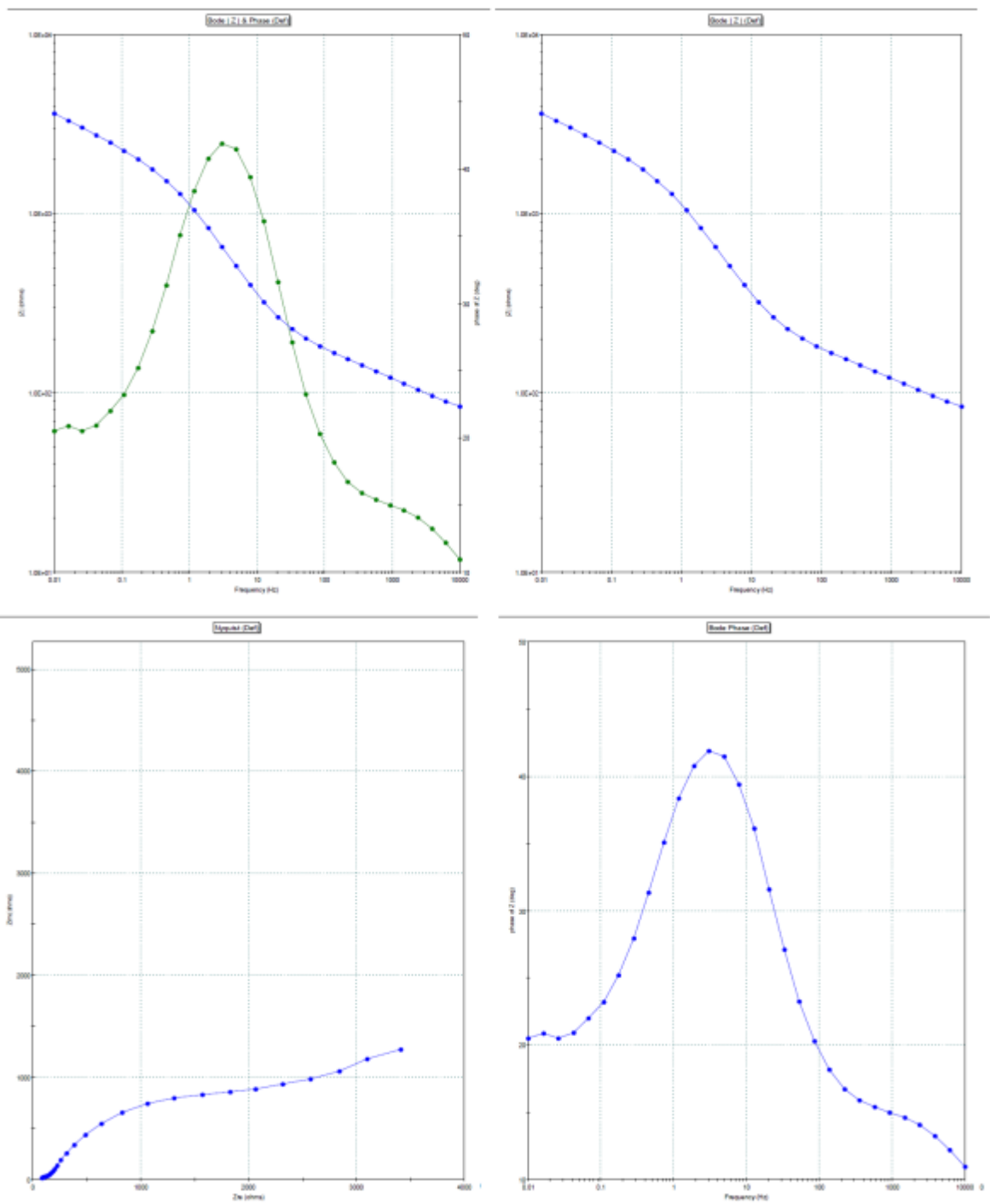


Figure 49. Bode and Nyquist plots for galvanized steel at 0.1 M NaCl solution.

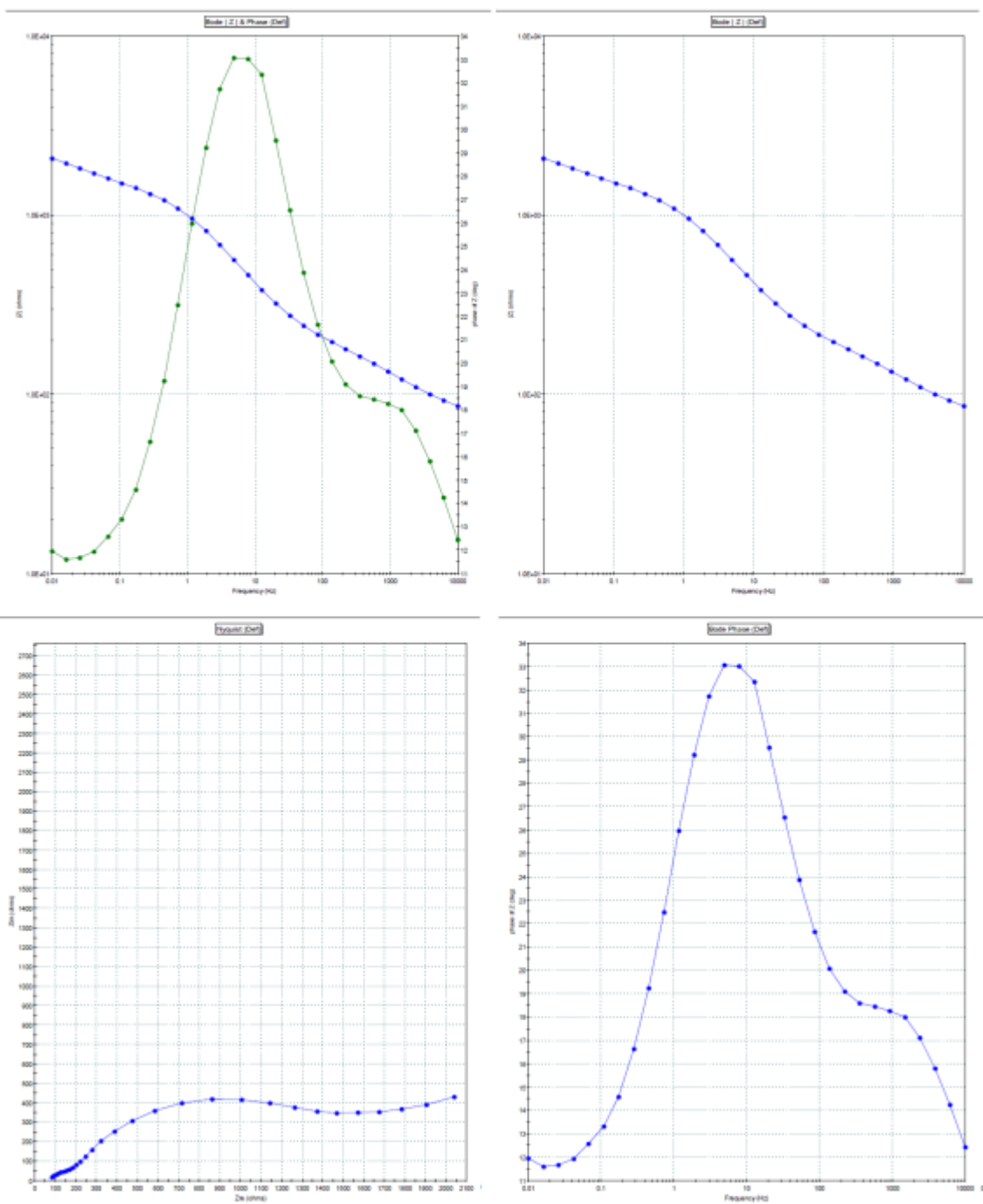


Figure 50. Bode and Nyquist plots for galvanized steel at 0.1 M NaCl solution.

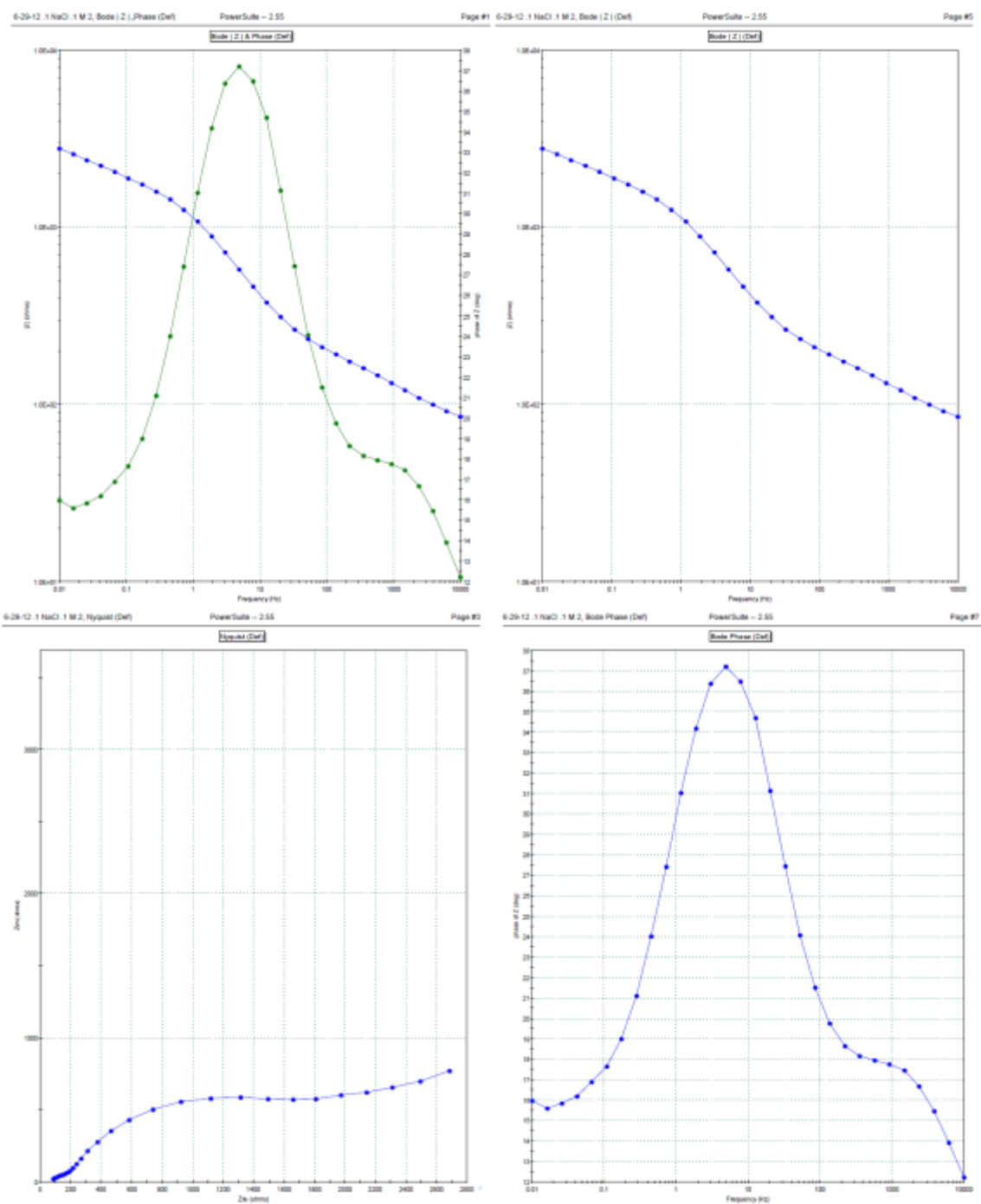


Figure 51. Bode and Nyquist plots for galvanized steel at 0.1 M NaCl solution.



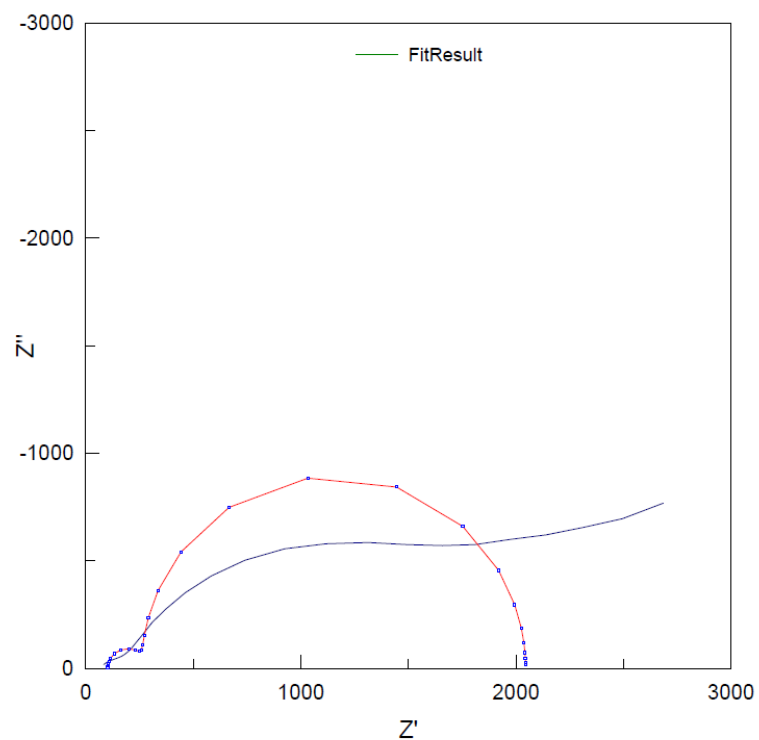


Figure 52 Nyquist plot of galvanised steel at 0.1 M NaCl. Acquired with Zview

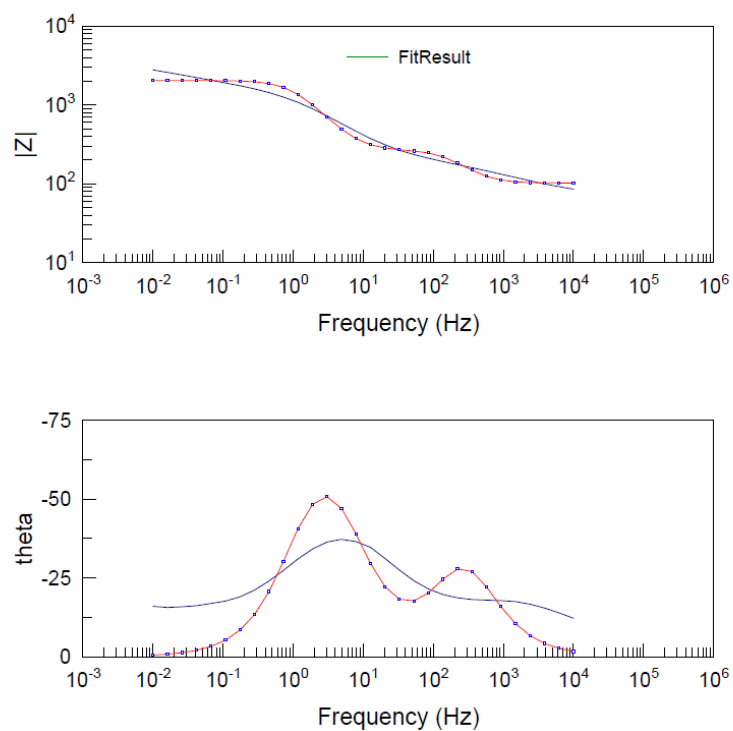


Figure 53 Bode and Phase angle plots of galvanised steel at 0.1 M NaCl. Acquired with Zview

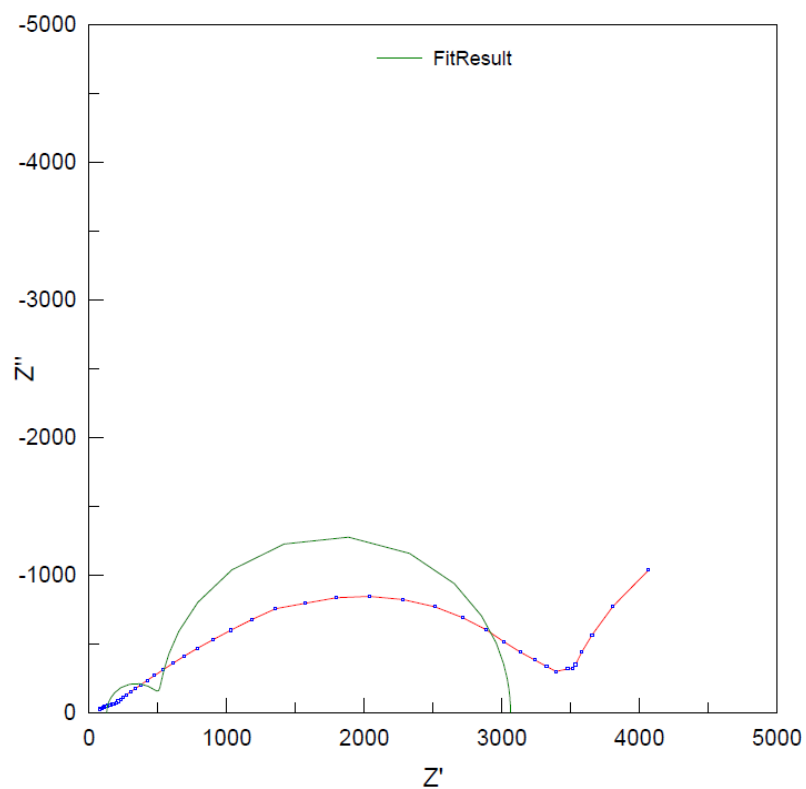


Figure 54 Nyquist plot of galvanized steel at 0.01 M NaCl. Acquired with Zview

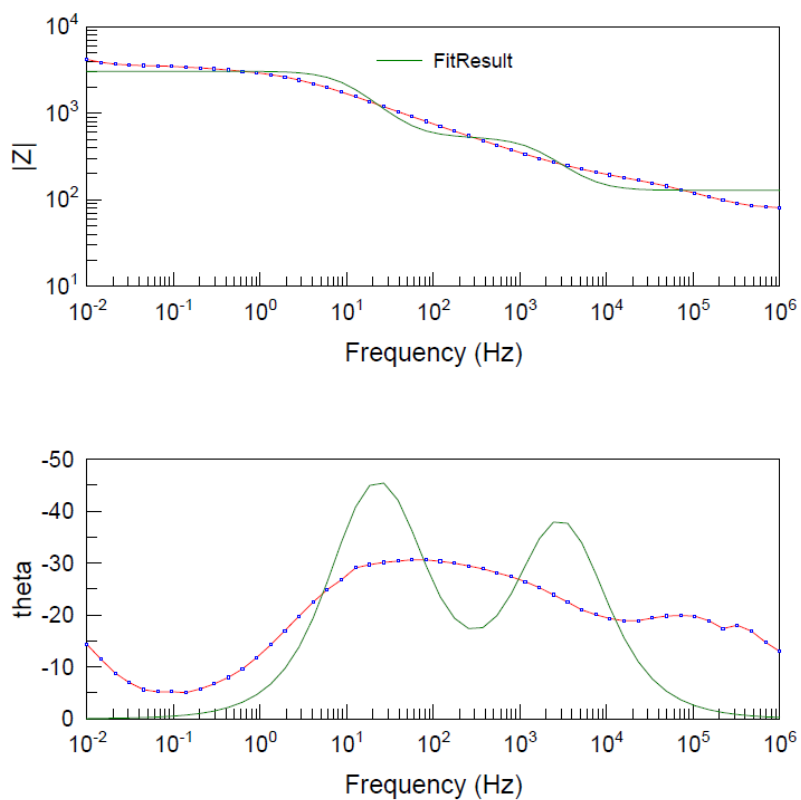


Figure 55 Bode and Phase angle plots of galvanized steel at 0.01 M NaCl. Acquired with Zview

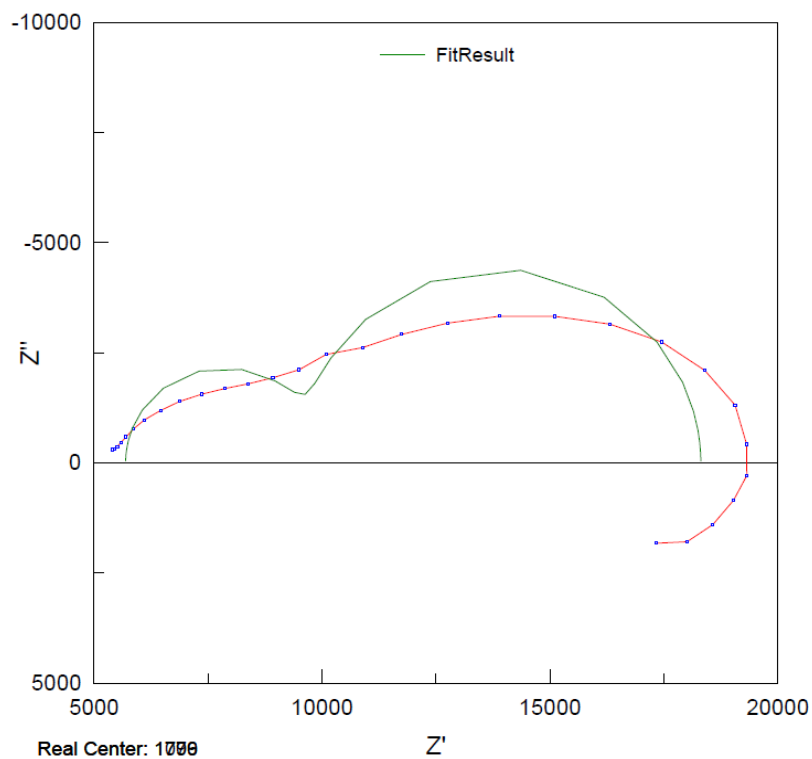


Figure 56 Nyquist plot of galvanised steel at 0.001 M NaCl. Acquired with Zview

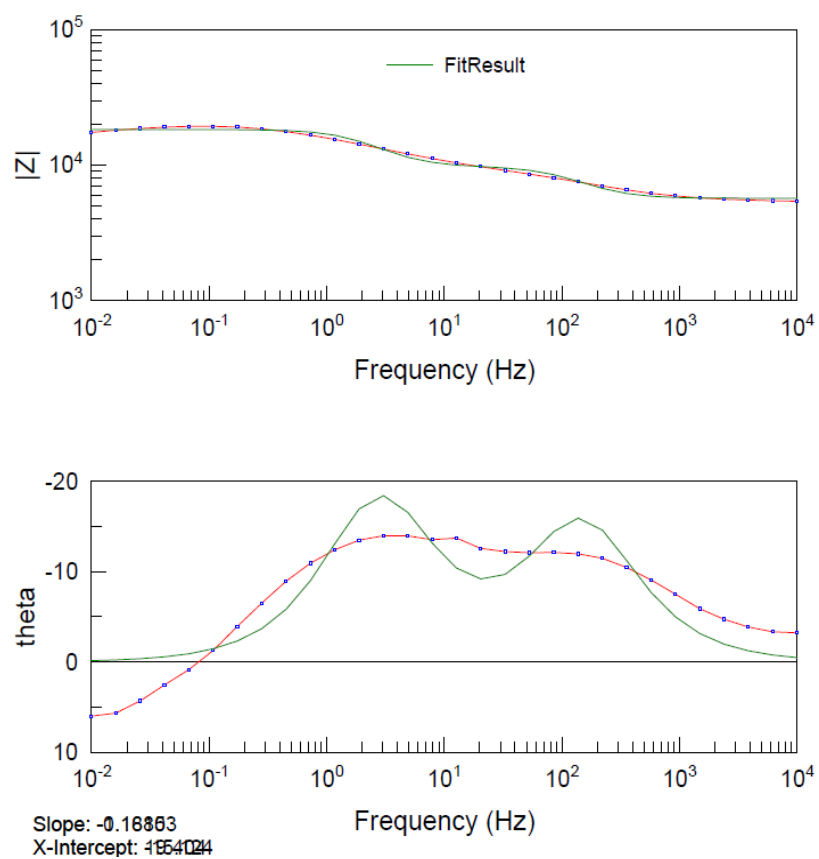


Figure 57 Bode and Phase angle plots of galvanised steel at 0.001 M NaCl. Acquired with Zview

Electrochemical Noise graph

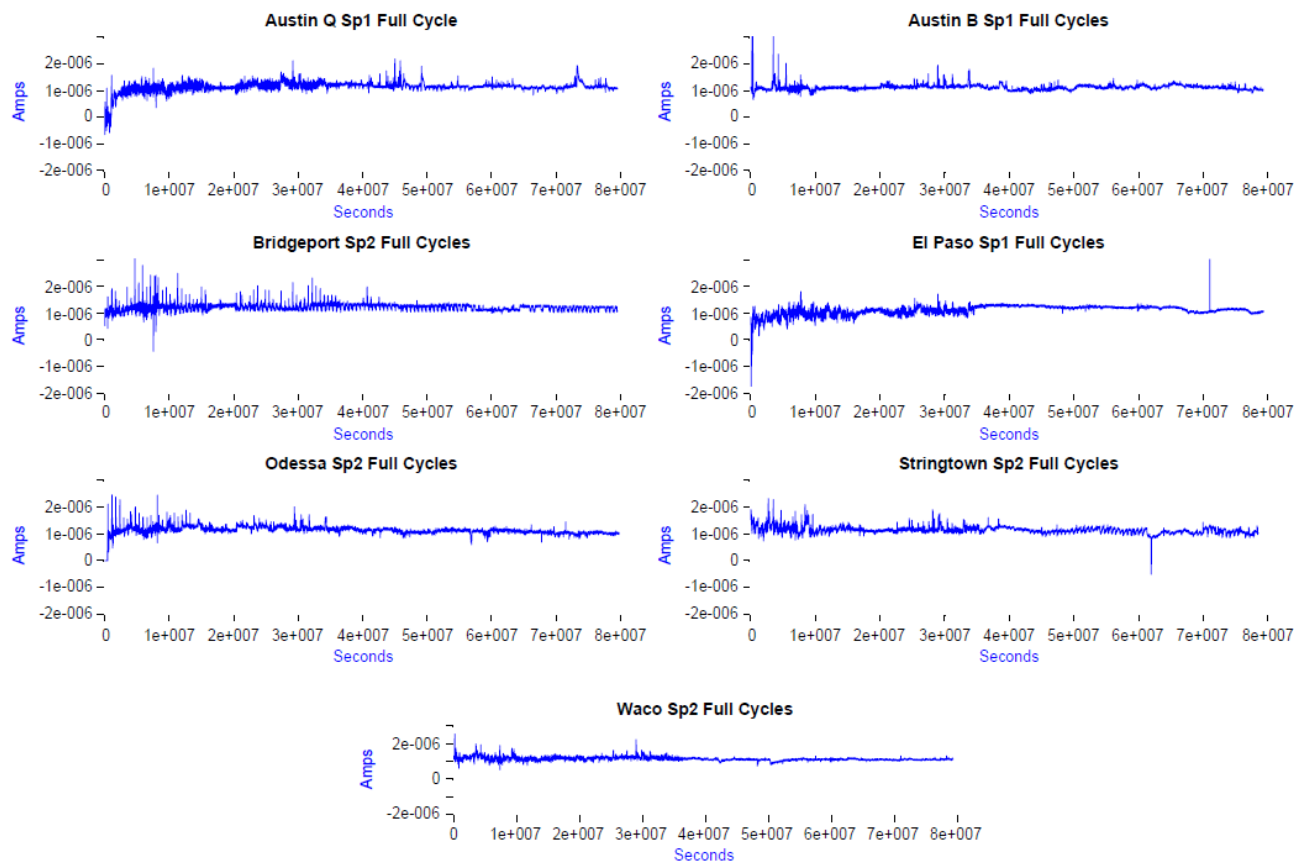


Figure 58 Electrochemical noise current vs. time

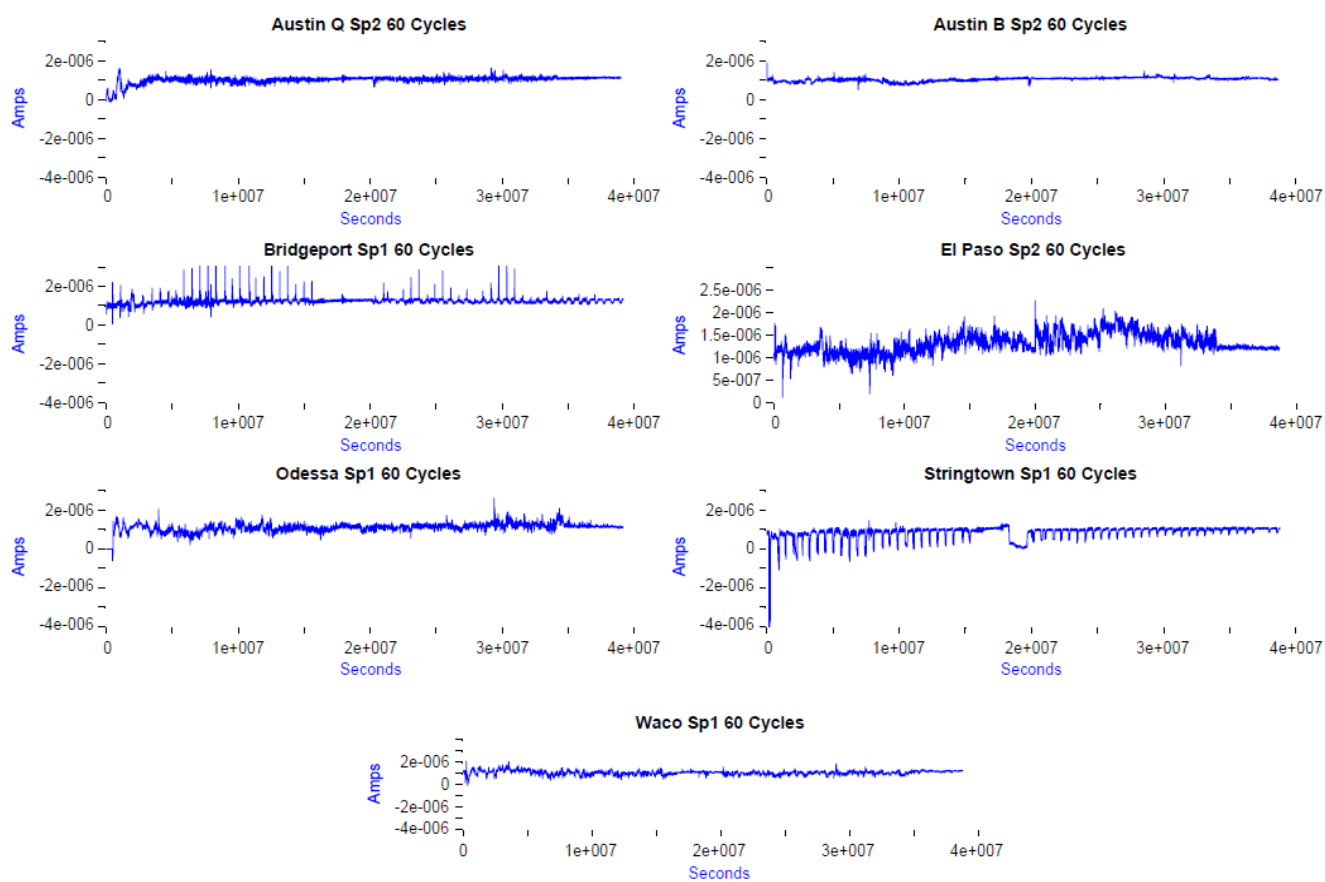


Figure 59 Electrochemical noise current vs. time

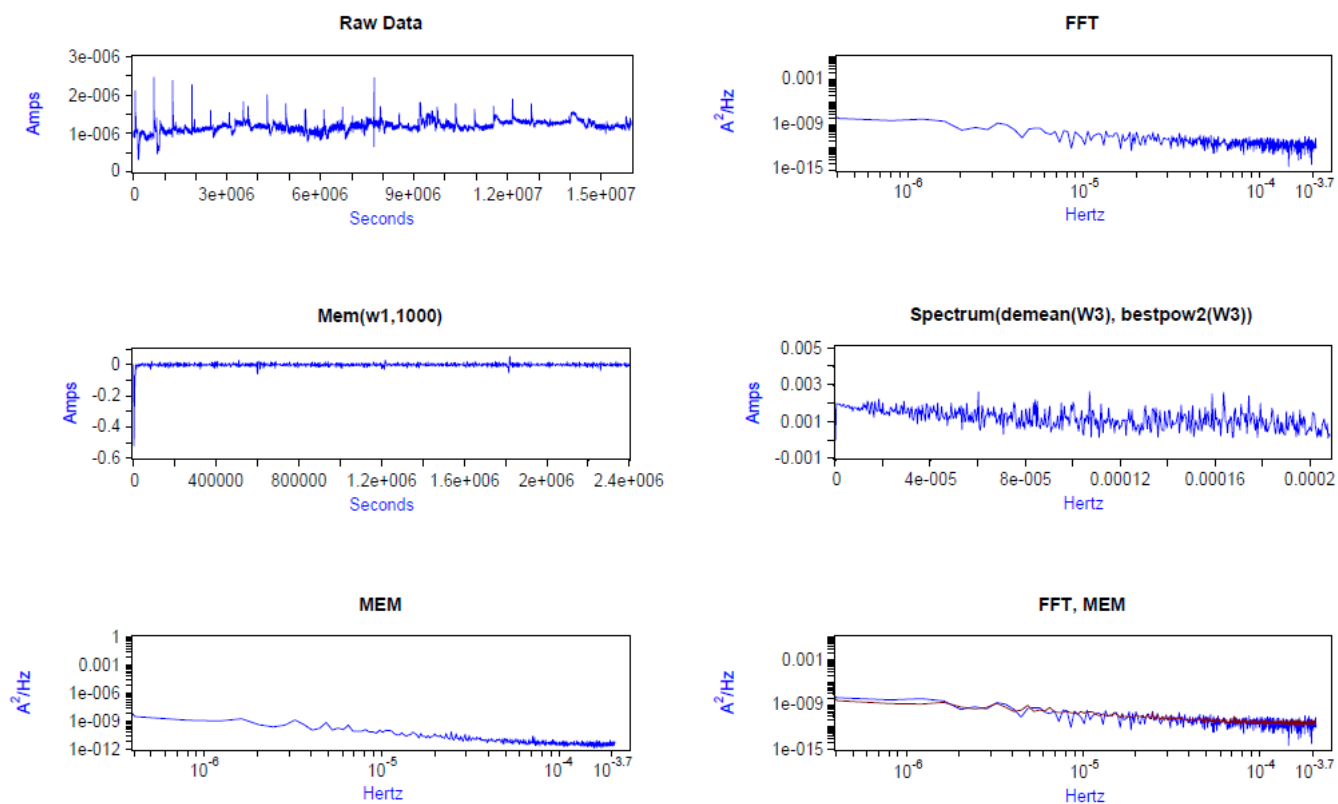


Figure 60 Electrochemical noise analysis for Quarry F wet/dry cycles Sp2 acquired with DADISP

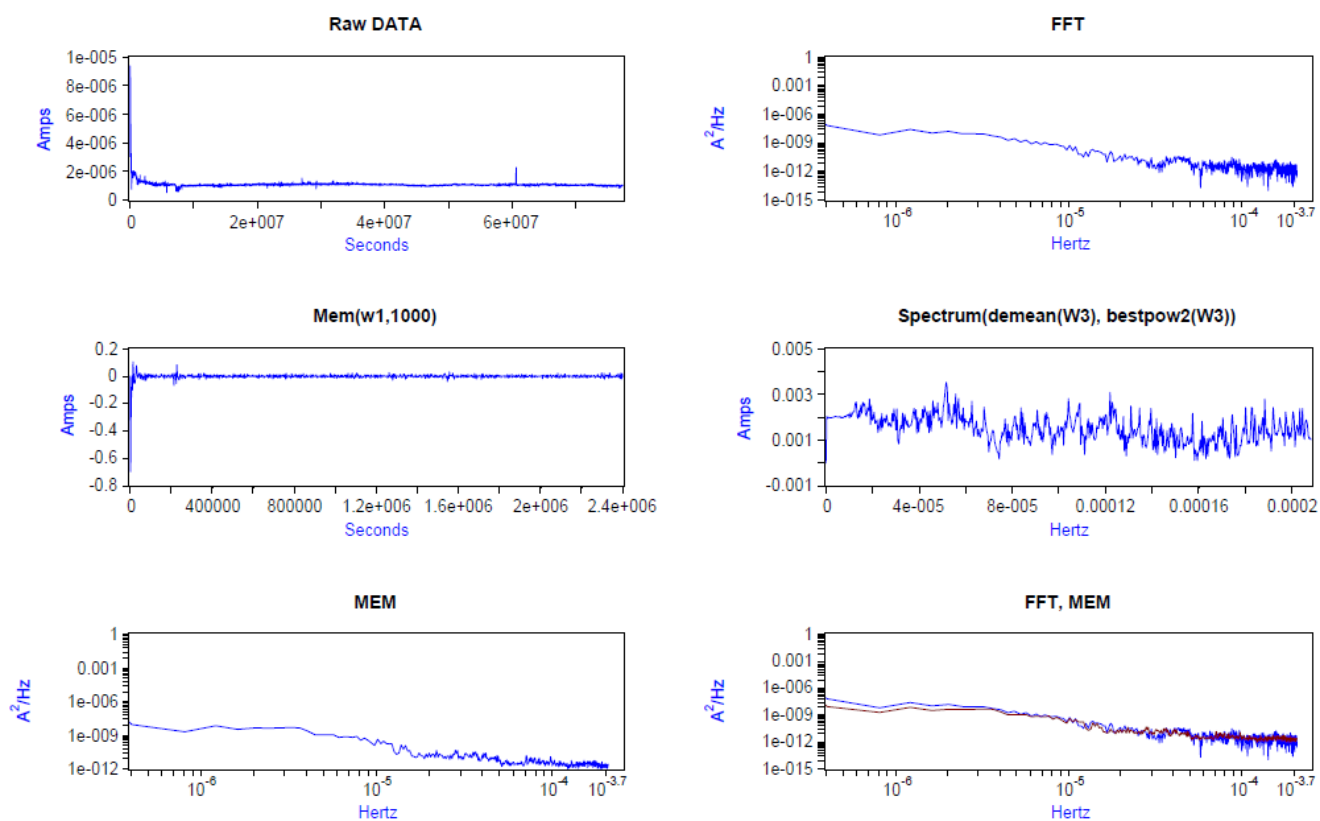


Figure 61 Electrochemical noise analysis for Quarry F wet cycles Sp4 acquired with DADISP

## Microstructures



Figure 62 Mesh 3 at 100x (2% Nital etch) acquired from optical microscope



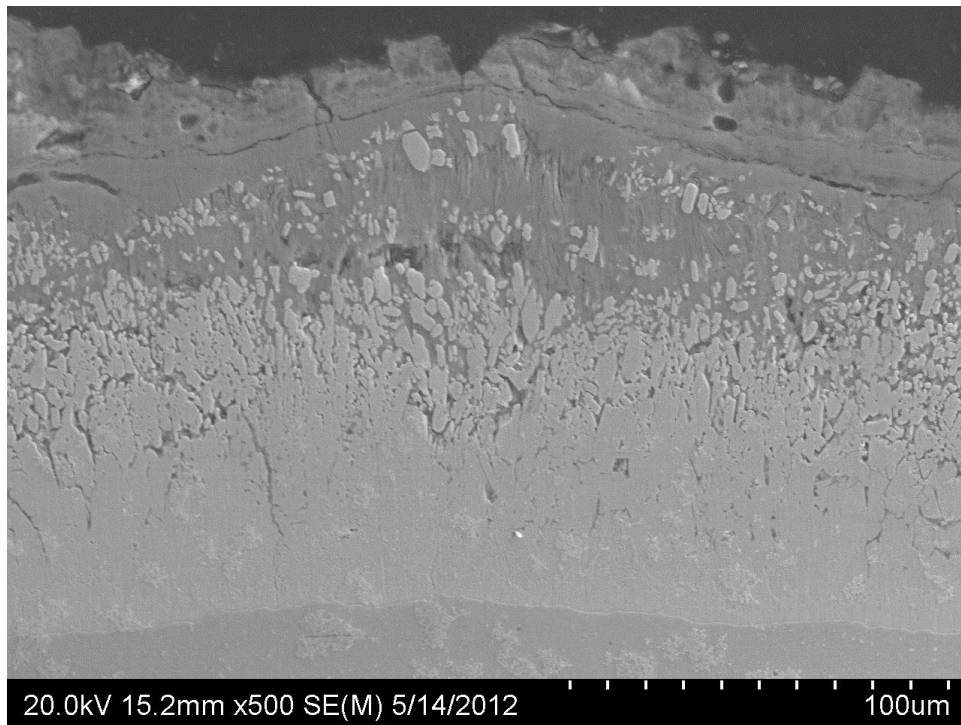


Figure 63 SEM picture of Bridgeport full cycles wet (2% Nital etch)

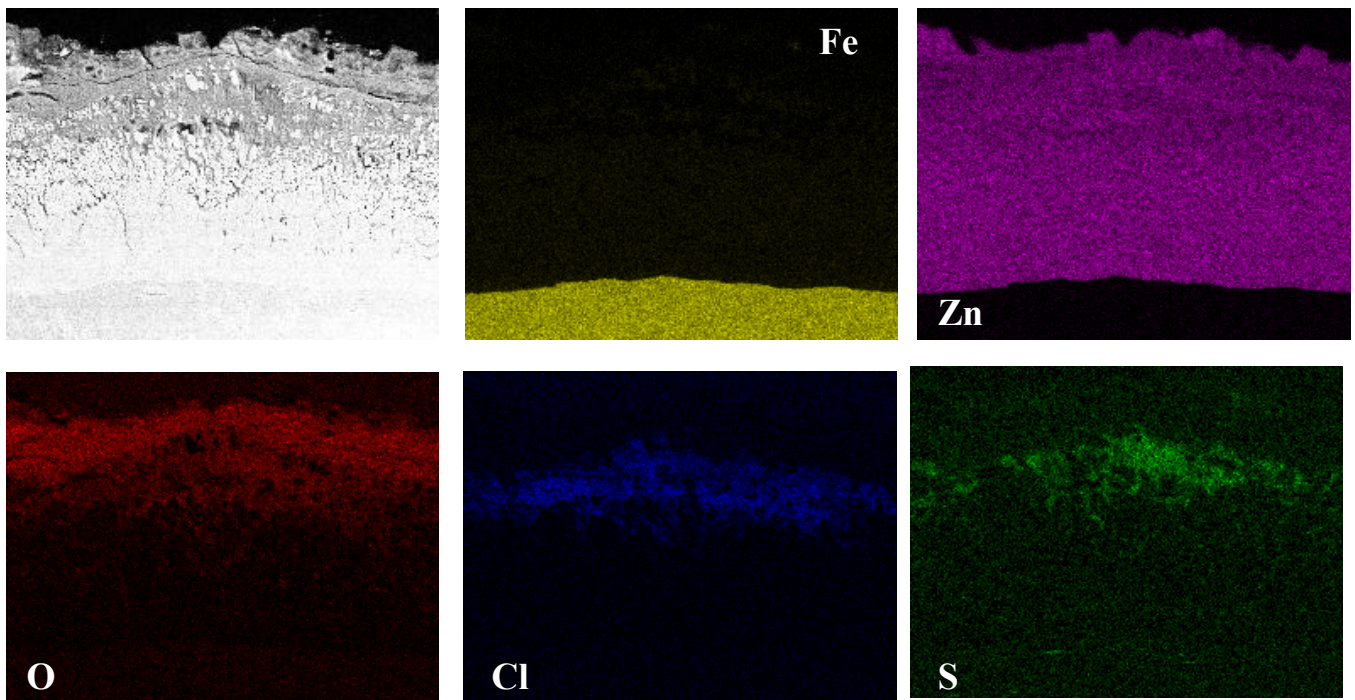


Figure 64 SEM mapping picture of Bridgeport full cycles wet (2% Nital etch)

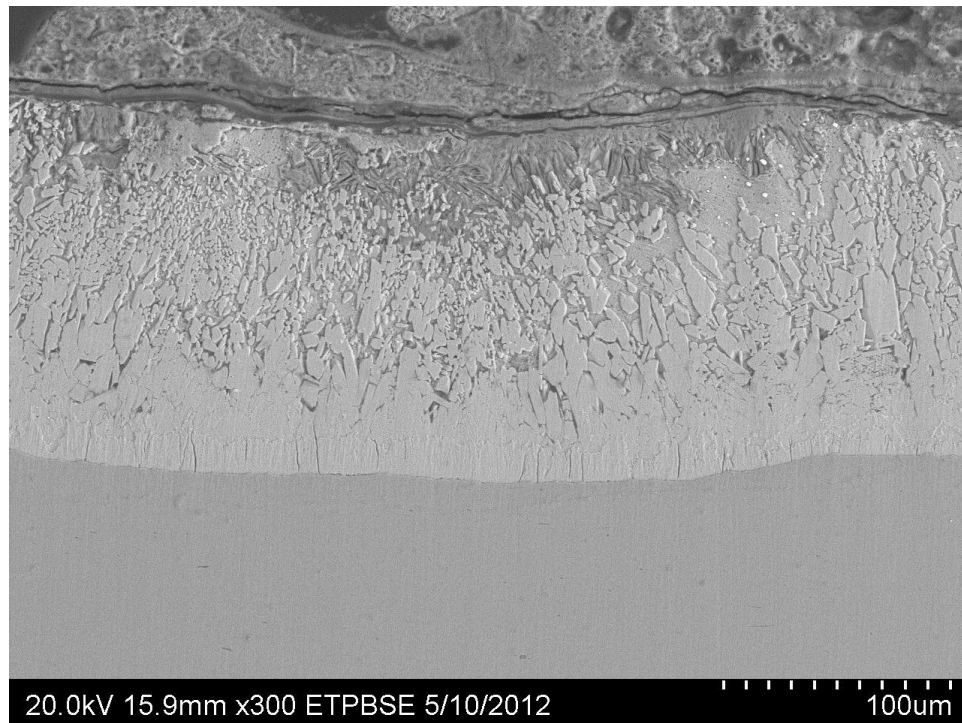


Figure 65 SEM picture of Quarry F Sp 2 full cycles wet dry (2% Nital etch)

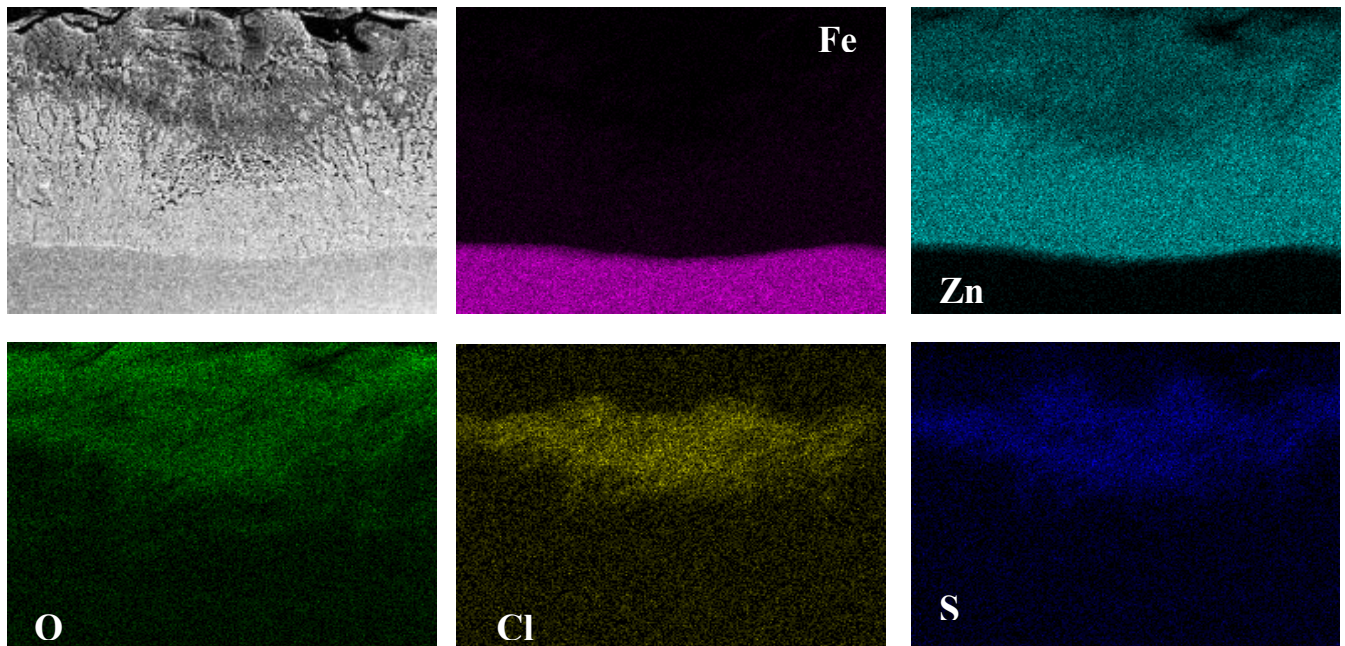


Figure 66 SEM mapping picture of Quarry F Sp 2 full cycles wet dry (2% Nital etch)

## **Curriculum Vitae**

Jesus F Hinojos was born on August 30, 1984 in Ciudad Juarez, Chihuahua, Mex. He is the first son of Jesus F Hinojos and Virginia de Hinojos. He obtained his Bachelor of Science in Mechanical Engineering degree at the University of Texas at El Paso (UTEP) in spring 2010. Shortly after, he pursued his graduate studies at UTEP for his Master of Science in Mechanical Engineering and graduated in the fall 2010.

Permanent Address: 125 Vaquero Ln Apt.46.  
El Paso, TX, 79912

This thesis was typed by Jesus F Hinojos.